Zinc Oxide / Nanocrystalline Silicon Contacts for Silicon Heterojunction Solar Cells

Huimin Li

JÜLICH
Forschungszentrum

Zinc Oxide / Nanocrystalline Silicon Contacts for Silicon Heterojunction Solar Cells

Huimin Li

Contents

Contents

Abstract

The silicon heterojunction (SHJ) solar cell is one of the most promising technologies and draws intensive attention due to its high conversion efficiency with low temperature coefficient and low energy consumption in production. Reducing the cost of cell fabrication is one of the key challenges to overcome for mass production. Usage of abundant materials and low-cost scalable production processes is a way to reduce cost. This work is focused on the replacement of conventional indium tin oxide (ITO) with aluminum-doped zinc oxide (AZO), which is a more environmentally friendly, abundant, and less costly transparent conductive oxide material. Layers of AZO were prepared with industrially relevant magnetron sputtering process at low temperature to address both scalability and cost reduction for future production lines. Optical and electronic properties of AZO implemented in rear-emitter SHJ solar cells is addressed in this study.

To reduce parasitic absorption of the window layer and form proper contact between doped silicon (Si) layer and AZO, doped hydrogenated nanocrystalline Si (n-type or p-type nc-Si:H) layers were used in the SHJ solar cells instead of the conventional doped hydrogenated amorphous Si (n-type or p-type a-Si:H) layers. The optical and electrical properties of doped nc-Si:H layers and AZO films were optimized for the application in SHJ solar cells. Moreover, the influence of AZO sputtering on the passivation quality of Si layer stacks was investigated and the contacts at the interfaces between AZO and p-type Si layers were studied. Furthermore, loss analysis of photovoltaic parameters, such as open circuit voltage (V_{oc}), fill factor (FF), series resistance (R_s), and short circuit current density (J_{sc}) of SHJ solar cells with AZO was carried out after the experimental analysis.

Various contact combinations between AZO and doped Si layers were tested in SHJ solar cells. It was observed that the solar cells with the combination of AZO and doped amorphous Si layers or n-type nc-Si:H layer operated properly. However, severe s-shaped illuminated current density-voltage (J-V) curves were observed in SHJ solar cells when AZO was in contact with p-type nc-Si:H layers. The s-shaped J-V characteristic is a result of a carrier collection barrier at the rear side of the device located at the interface between p-type nc-Si:H and AZO. Increasing the doping in p-type nc-Si:H layer or inserting a seed layer prior to the p-type nc-Si:H layer resulted in suppression of the contact barrier. However, increase of either the doping concentration or the sputtering temperature of AZO films did not contribute to the reduction of contact barrier.

It was observed that the AZO sputtering process during cell fabrication affected the passivation quality of the cell stack. Thus, effects of AZO sputtering temperature and pressure on effective carrier lifetime were studied for various combinations of AZO and doped Si layers. Generally, high initial effective carrier lifetimes were observed after Si layer deposition, but the lifetimes were significantly reduced upon AZO sputtering. However, the detrimental effect of AZO sputtering on the lifetime of Si layer stacks were eliminated completely by annealing especially

Abstract

for room temperature AZO sputtering process. It shows the application potential of room temperature sputtered AZO in SHJ solar cells. Increasing the AZO sputtering temperature contributed to the reduction or removal of effective carrier lifetime degradation due to in-situ annealing. Variation of AZO sputtering pressure had no influence on the lifetime variation. Compared to nc-Si:H layers, amorphous Si layers were less sensitive to the influence of AZO sputtering.

With the application of AZO and Si layers of n-type nc-Si:H and p-type a-Si:H, a cell efficiency of 21.2 % for a 19 mm × 19 mm cell was achieved with V_{oc} = 720 mV, J_{sc} = 39.1 mA/cm^2 and FF = 75.4 %. A cell efficiency of 19.3 % for a large-area 156.75 mm × 156.75 mm cell was achieved with V_{oc} = 732 mV, J_{sc} = 36.2 mA/cm^2 and FF = 72.8 %. The best cell results were analyzed for losses with respect to the state-of-the-art theoretical limits. The loss in V_{oc} is mainly due to the recombination at the surface and in the bulk (Shockley-Read-Hall), and due to the the non-optimal carrier selectivity at the contact interfaces with silicon layer stacks. The loss in FF is mainly due to the series resistance and the recombination in the non-optimal junction region. The series resistance is mainly due to the finger resistance and the contact resistance at the interface between p-type Si layer and AZO film. The loss in J_{sc} is primarily due to the parasitic absorption in the short and long wavelength regions, the escape of long-wavelength light from the front side of solar cell, and the front metal shadowing.

The present work demonstrates the feasibility to replace conventional ITO with aluminum doped zinc oxide (AZO), which is prepared at room temperature with standard industrial magnetron sputtering technique, in the process chain of silicon heterojunction solar cells.

Zusammenfassung

Die Silizium-Heteroübergangssolarzelle (SHJ) ist eine der vielversprechendsten Solarzellentechnologien und zieht aufgrund ihres hohen Wirkungsgrades, ihres niedrigen Energieverbrauchs während der Produktion und ihres niedrigen Temperaturkoeffizienten große Aufmerksamkeit auf sich. Die Reduzierung der Produktionskosten ist eine Hauptherausforderung, um die Schwierigkeiten für die Massenproduktion zu überwinden. Die Nutzung reichlich vorhandener Materialien und kostengünstige, skalierbare Produktionsprozesse ist ein Weg Kosten zu reduzieren. Diese Arbeit untersucht die Möglichkeit standardmäßig genutztes Indiumzinnoxid (ITO) durch Al-dotiertes Zinkoxid (AZO) zu ersetzen, welches ein umweltfreundlicheres, reichlich vorhandenes und kostengünstigeres transparentes leitfähiges Oxid ist. AZO-Schichten werden mittels industrierelevanten Magnetron-Sputter-Prozessen bei niedrigen Temperaturen abgeschieden, welches gleichzeitig Skalierbarkeit und Kostenreduktion zukünftiger Prozesslinien ermöglicht. In dieser Arbeit werden die optischen und elektronischen Eigenschaften von AZO-Schichten untersucht, die in SHJ Solarzellen in Rückenseitenemitter-Konfiguration eingebaut werden.

Um die parasitäre Absorption der Fensterschicht zu verringern und einen guten Kontakt zwischen der dotierten Si-Schicht und AZO zu bilden, wurden anstelle der herkömmlichen dotierten hydrierten amorphen Si-Schichten (n-Typ oder p-Typ a-Si:H) dotierte hydrierte nanokristalline Si-Schichten (n-Typ oder p-Typ nc-Si:H) in die SHJ-Solarzellen implementiert. Die optischen und elektrischen Eigenschaften von dotierten nc-Si:H-Schichten und AZO-Filmen wurden für die Anwendung in SHJ Solarzellen optimiert. Darüber hinaus wurde der Einfluss von gesputtertem AZO auf die Passivierungsqualität in Si-Schichtstapeln und die Kontakte an den Grenzflächen zwischen der AZO- und der p-Si-Schicht intensiv untersucht. Zudem wurde nach der Analyse der experimentellen Ergebnisse eine Verlustanalyse für die photovoltaischen Parameter Leerlaufspannung (V_{oc}), Füllfaktor (FF), Serienwiderstand (R_s) und Stromdichte (J) von SHJ-Solarzellen durchgeführt.

Verschiedene Kombinationen zwischen AZO und dotierten Si-Schichten wurden in SHJ-Solarzellen getestet. Solarzellen mit einer Kombination aus AZO und dotierten amorphen Si-Schichten oder AZO und nc-Si:H-Schichten (n-Typ) arbeiteten einwandfrei. Jedoch wurden unter Beleuchtung stark s-förmige Photostromdichte-Spannungs-Kurven (J-V) für SHJ-Solarzellen mit einem AZO - nc-Si:H (p-Typ) Kontakt beobachtet. Die s-förmige J-V-Kennlinie ergab sich aufgrund einer Barriere an der Rückseite des Bauelements zwischen p-Typ nc-Si:H und AZO, die die Ladungsträgersammlung hemmte. Das Erhöhen der Dotierung in der nc-Si:H-Schicht (p-Typ) oder das Einfügen einer Keimschicht vor der nc-Si:H-Schicht (p-Typ) trugen zur Reduzierung der Kontaktbarriere bei. Eine Erhöhung der Dotierungskonzentration der AZO-Filme oder höhere Sputtertemperaturen bei der AZO-Abscheidung führten hingegen nicht zur Verringerung der Kontaktbarriere.

Zusammenfassung

Es wurde beobachtet, dass der AZO-Sputterprozess die Passivierungsqualität in den Zellstapeln während des Zellherstellungsprozesses beeinflusste. Daher wurden die Auswirkungen der Temperatur und des Drucks während der Sputterdeposition der AZO-Schicht auf die effektive Ladungsträgerlebensdauer für verschiedene Kombinationen von AZO- und dotierten Si-Schichten im Detail untersucht. Im Allgemeinen wurden nach der Abscheidung der Si-Schicht hohe effektive Ladungsträgerlebensdauern beobachtet, welche jedoch nach dem AZO-Sputterprozess signifikant kleiner wurden. Dieser schädliche Effekt des AZO-Sputterprozesses auf die effektive Ladungsträgerlebensdauer konnte durch einen nachträglichen Temperprozess vollständig beseitigt werden. Dies galt auch für bei Raumtemperatur gesputtertem AZO, welches das Potenzial dieser AZO-Schichten für die Anwendung in SHJ-Solarzellen verdeutlichte. Höhere Temperaturen bei der AZO-Deposition führten zu einer Reduzierung oder Beseitigung der Lebensdauerdegradierung aufgrund von in-situ-Tempern. Die Variation des Drucks während der AZO-Deposition hat keinen Einfluss auf die Variation der Lebensdauer. Im Vergleich zu nc-Si:H-Schichten waren amorphe Si-Schichten weniger empfindlich gegenüber dem Einfluss des AZO Sputterns.

Die Anwendung von AZO- und Si-Schichten aus nc-Si:H (n-Typ) und a-Si:H (p-Typ) führte zu einem Zellwirkungsgrad von 21,2% für eine 19 mm × 19 mm-Zelle mit V_{oc} = 720 mV, J_{sc} = 39,1 mA/cm² und FF = 75,4 %. Zudem wurde eine Zelleneffizienz von 19,3 % für eine großflächige 56,75 mm × 156,75 mm-Zelle mit V_{oc} = 732 mV, J_{sc} = 36,2 mA/cm² und FF = 72,8 % erreicht. Eine detaillierte Verlustanalyse der photovoltaischen Parameter der besten Solarzelle wurde unter Berücksichtigung der theoretischen Grenzen durchgeführt. Der V_{oc}-Verlust wurde hauptsächlich auf die Ladungsträgerrekombinationen an der Oberfläche und im Absorbermaterial (Shockley-Read-Hall) sowie auf die nicht optimale Ladungsträgerselektivität an den Kontaktgrenzschichten mit Siliziumschichtstapeln zurückgeführt. Die hauptsächlichen FF-Verluste konnten einem hohen Serienwiderstand und der Rekombination in der Raumladungszone zugeordnet werden. Der Serienwiderstand bestand hauptsächlich aus dem Serienwiderstand der Metallfinger und dem Kontaktwiderstand an der Grenzfläche zwischen der Si-Schicht (p-Typ) und der AZO-Schicht. Die Hauptursachen für die Verringerung der Kurzschlussstromdichte waren parasitäre Absorption im langwelligen und kurzwelligen Wellenlängenbereich, der Lichtaustritt an der Frontseite der Solarzelle und die Abschattung durch das Frontmetall.

Die vorliegende Arbeit demonstriert das vielversprechende Potenzial in der Prozesskette der SHJ-Solarzellen-Herstellung standardmäßig genutztes ITO durch Al-dotiertes Zinkoxid (AZO) zu ersetzen, welches mittels industrierelevanten Magnetron-Sputter-Prozessen bei Raumtemperatur abgeschieden werden kann.

Chapter 1 Introduction

The enormous demand of electricity worldwide is mostly met by energy derived from burning of fossil fuels. The environmental impact of such practices is well known and use of renewable energy sources can help us mitigate the damage. Solar energy is being promoted worldwide as a primary source of renewable energy because of its easy accessibility all around the world [1, 2]. Photovoltaics (PV) provide a way to directly convert the solar radiation to electricity with the use of photovoltaic devices developed by implementation of a large variety of physical concepts, novel structures, and custom designed materials [3]. Last four decades have seen humongous development in different PV technologies and as shown in Fig. 1.1. The best research-cell efficiency chart maintained by National Renewable Energy Laboratory (NREL) [4] corroborates this claim. Among different materials in use for PV, silicon shows significant advantages over others because of its non-toxic properties and abundance in earth. Due to these advantages it has been extensively used for development of high efficiency solar cells and is the dominant technology in the PV market at present [5, 6].

After the first semiconductor p-n junction solar cells prepared by Russel Ohl of Bell Laboratories in 1941 [7, 8], the first-generation Silicon (Si) solar cell was developed based on monocrystalline, polycrystalline, and hybrid Si cell technologies. To reduce the material cost, the second-generation solar cells were based on thin-film technology [9] and Si thin-film became the key candidate for the second-generation technology. However, for the mature second-generation technology, due to the efficiency limitation cost again became the dominant factor by those of constituent materials in solar cell. Therefore, the solar cell technology development entered into the third generation characterized with "high-efficiency" based on thin-film deposition methods [10].

The "high efficiency" technology has been vigorously promoted by the Chinese government's policy to restructure its power support system with high efficiency cells, by the development of better solar cell technologies, and by the market pull effect from chasing best levelized cost of energy (LCOE) which addresses the average minimum price at which electricity must be sold in order to break-even over the lifetime of power generation asset [11]. Among the high efficiency solar cells, the passivated emitter and rear cells (PERC) family dominate the PV market [12, 13]. The technologies of heterojunction (HJ) and interdigitated back contact (IBC) have shown their
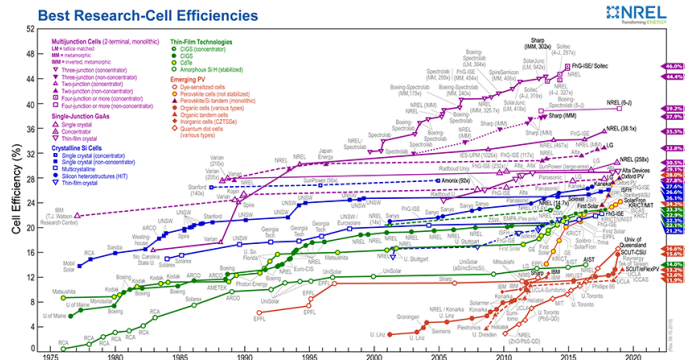
Fig. 1.1. Best research-cell efficiency chart from the National Renewable Energy Laboratories (NREL) in 2019. This plot is courtesy of the National Renewable Energy Laboratory, Golden, CO.

potentials as well to further increase the energy conversion efficiency. Besides, tandem structures in solar cells also allow for more efficiently conversion from sunlight to electricity and makes high efficiency solar cells. In this work, the HJ technology (HJT) is focused for the cell development due to its potential to reduce the capex and cost of the ownership with the advantages of high efficiency, low temperature coefficient, good low-light performance of the cells, fewer process steps, and bificiality [14-17]. Within HJT, the silicon heterojunction (SHJ) solar cell with intrinsic amorphous Si layer is one of the most promising technologies for the requirements of high efficiency and low cost. Superior heterojunction solar cells with conversion efficiency above 24 % have been achieved by Meyer Burger Company which is approaching the practical limits of 25 % in mass manufacturing [11]. A photoconversion efficiency over 26 % was achieved for the SHJ solar cell with interdigitated back contact structure [17]. Based on the excellent performance of HJT, its combination with perovskite for tandem structures could be one option for the future development [18, 19].

This work is focused on the contacts between aluminum (Al)-doped zinc oxide (AZO), one kind of transparent conductive oxide (TCO), and doped hydrogenated nanocrystalline Si layers (n-type or p-type nc-Si:H) in SHJ solar cells. The traditional notation :H for hydrogenated in all Si layers was skipped in this work for the consideration of readability. The work is divided into four parts. The first part deals with the properties of doped nc-Si and AZO layers. The second part deals with the SHJ solar cell performance with the implementation of doped nc-Si and AZO layers. The third part deals with the influence of AZO sputtering on the passivation quality and the contact at the interface between AZO and p-type nc-Si. The fourth part deals with the loss analysis on the solar cell parameters.

Chapter 2 reviews the basic knowledge and literature on the development of crystalline silicon (c-Si) solar cells, especially the silicon heterojunction solar cells, in three sections. Section 2.1 describes the development of c-Si solar cells and the current situation in PV market. Section 2.2 is

divided into two parts. Section 2.2.1 describes the concept of conventional SHJ solar cells and its structure, followed by a discussion on the state-of-the-art approaches towards the limit efficiency of SHJ solar cells. Section 2.2.2 describes the development of SHJ solar cells with alternative Si thin-film and TCO layers. Section 2.3 describes the current work of SHJ solar cells fabricated with the different layer combinations of AZO and doped nc-Si.

Chapter 3 describes the SHJ solar cell fabrication process and the analytical methods used to characterize the properties of the materials and SHJ solar cells in this work. The detailed analyses of experimental results are presented in the following experimental chapters. Section 3.1 describes the fabrication process for SHJ solar cells from wafer cleaning, Si layer deposition, AZO sputtering, until metallization. Section 3.2 is divided into two parts. Section 3.2.1 focuses on the material characterization methods and section 3.2.2 focuses on SHJ solar cells characterization methods.

Chapters 4-7 gives details of the experimental works conducted. Chapter 4 focuses on the material development for the SHJ solar cells and is divided into two sections, the deposition and characterization for the n-type and p-type nc-Si layers in section 4.1 and for the AZO in section 4.2. Chapter 5 describes the results of SHJ solar cell with the contacts between various AZO and doped Si layers. The SHJ solar cells are fabricated with the Si layer combinations of (1) n-type amorphous silicon (a-Si) / p-type a-Si, (2) n-type nc-Si / p-type a-Si, (3) n-type a-Si / p-type nc-Si, and (4) n-type nc-Si / p-type nc-Si on n-type Czochralski (Cz) textured wafers with rear emitter configuration, respectively. Section 5.1 describes the optical and electrical properties of the four kinds of doped Si layers applied in SHJ solar cells. Section 5.2 describes the implementation of AZO films sputtered by varying different parameters, sputtering temperature, target doping concentration, and precursor, in SHJ solar cells. In this section, the contact resistance between AZO and doped Si layers have been measured. Chapter 6 describes the influence of AZO sputtering on the passivation quality of the surface defects in SHJ solar cells. Section 6.1 describes the influence of AZO sputtering on the symmetrical structures with either i/n (intrinsic a-Si /n-type nc-Si) stack or i/p (intrinsic a-Si/ p-type a-Si) stack on both sides of the wafer. Section 6.1 is divided into two sub-sections. Section 6.1.1 describes the influence of AZO sputtering pressures and substrate temperature on the i/n and i/p symmetrical structures. Section 6.1.2 describes influence of AZO sputtering on i/n symmetrical structures deposited with varying gas flow rate ratios between silane and hydrogen and different i/n stack thickness. Section 6.2 describes the influence of room temperature (RT) AZO sputtering on the SHJ solar cell precursors. Chapter 7 describes the contact properties of the interface between p-doped Si layer and AZO in SHJ solar cells. Section 7.1 describes the s-shaped current density-voltage (J-V) curve of the SHJ solar cell with p-type nc-Si layer. Section 7.2 describes the current-voltage (I-V) characteristics of the contact at the interface between p-type nc-Si and AZO. Section 7.3 describes the optimizations on the contact barriers by varying p-type nc-Si and AZO layers. Section 7.3.1 describes the varying in p-type nc-Si layer with increased doping level or thickness, or with inserting a seed layer prior to the p-type nc-Si. Section 7.3.2 describes the varying in AZO sputtered with increased substrate temperatures or target doping concentrations. In addition, influence of the deposition order of AZO and p-type Si on cell performance was presented.

Chapter 8 is focused on the loss analysis on the photovoltaic parameters of SHJ solar cells. Section 8.1 introduces the theoretical limitation for the solar cell fabricated in this work. Section 8.2 to 8.5 describes the loss analyses of open circuit voltage, fill factor, series resistance, and short circuit current density, respectively.

Chapter 9 summarizes this work and presents the outlook for the continuation of the work in future.

Chapter 2 Fundamentals and literature review

2.1 Crystalline silicon solar cells

The maximum theoretical efficiency of c-Si solar cells is limited by the intrinsic properties of Si which is of interest for the continuous improvement in technology for the PV research. The calculations for the maximum theoretical efficiency of c-Si solar cells have been carried out with the state-of-the-art parameters in [20, 21]. The efficiency of 29.43% has been calculated for a 110-μm-thick solar cell made of undoped Si considering the intrinsic limitation. However, in a real solar cell, the recombination at surface defects and defects in Si, the non-ideal optical properties, and the series resistance are also needed to be taken into consideration for efficiency limitation evaluation. The current efficiency record for single junction silicon solar cells is 25.6% achieved by Panasonic [22]. Approaching the efficiency limitation drives the continuous improvement in the technology development for c-Si solar cells.

Recombination loss at the rear of the conventional cell with Al-back surface field (Al BSF) limits the efficiency to 19%. This limitation has motivated a technological turning point towards high efficiency exceeding 20% in c-Si solar cell PV market [23]. There are four high-efficiency cell technology candidates for the c-Si solar cell development: (1) the passivated emitter and rear cell (PERC), (2) the passivating contacts technology, (3) the heterojunction technology, and (4) the interdigitated back contact (IBC) technology. The feasible combinations within these four technologies shows the potential to achieve high efficiency solar cell as well.

In mass production, the quantity of Al BSF cells will be gradually reduced and the well-developed passivated emitter and rear cell (PERC) family [24] with efficiency above 20% will become the mainstream by 2029 [25] as shown in Fig. 2.1. The PERC family includes the passivated emitter and rear directly-contacted (PERD) and its extensions, e.g. passivated emitter with rear locally diffused (PERL), passivated emitter, rear totally-diffused (PERT), and the passivated emitter, rear floating-junction (PERF).
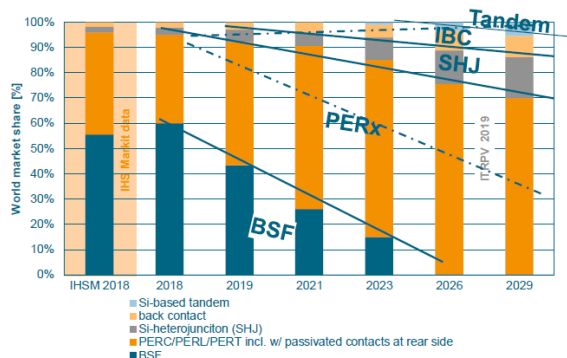
Fig. 2.1. Trends of the market share for cell technologies until 2029 [25].

The PERC configuration can effectively reduce the recombination loss at the interface between metal and crystalline Si wafer [26]. Meanwhile, the PERC cell shows the advantage of a great tolerance towards both mono- and multi-crystalline wafers. Jinko Solar has reported the record efficiency of 23.95% for PERC cells on p-type mono-crystalline substrate with passivated contact technology in 2018 and the efficiency of 22.04% for PERC cells on multi-crystalline substrate in 2017 [27]. The PERC platform has been adapted with the on-going incremental improvements to achieve cell efficiencies approaching 24%, and even 25% of the best laboratory cells [6]. As shown by Zhao et al. [28], a cell efficiency of 24.7% has been achieved by PERL cells on float zone Si substrate and 24.5% for the modified PERT cells on a magnetically confined Czochralski substrate. These record efficiencies show the technological potential of the PERC family in both p-type mono- and multi-crystalline directions. However, it will take some time to be realized in production lines. Except for that, the p-type wafers can be negatively affected by the light induced degradation. More important is that the cost of the n-type wafers has been significantly reduced,
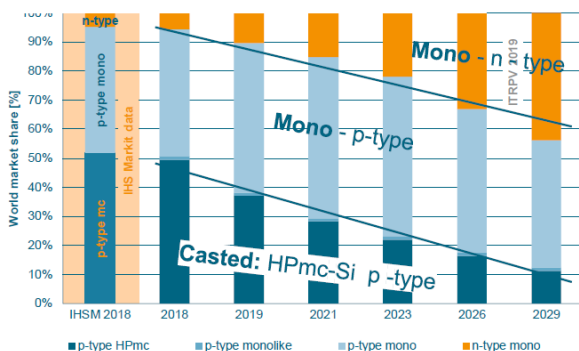
Fig. 2.2. Trends of the market share of the wafer types until 2029 [25].

and can be reduced further with the possibility of a thickness in the range of approximately 120 μm in next ten years [25]. Due to the reducing thickness and the potential for high efficiency, n-type monocrystalline will occupy increasing market share as shown in Fig. 2.2, accompanied by the increasing share of the n-PERT and n-PERL cells fabricated on the n-type wafer combined with passivated contacts.

The passivating contacts technology incorporates thin films with the contact structure to passivate the surface and to extract certain types of carriers simultaneously [29, 30]. Within passivating contacts technology, tunnel oxide passivated contact (TOPCon) is based on the growth of the ultra-thin interfacial oxide, the deposition of intrinsic polycrystalline Si layer and the following in- and ex-situ doping processes. The ultra-thin interfacial oxide acts as the selective passivated contact and can be grown either thermally or wet chemically [31]. This technology combined with the front structure from the PERC and adapted rear side with the full area passivating contact allowing for high open circuit voltage (V_{oc}) as well as high fill factor (FF) [32]. Meanwhile, this technology is compatible with the high temperature process and can avoid the patterned metal contact in mass production. Richter et. al has announced the record efficiency of 25.7% for TOPCon cells on a 2 cm × 2 cm area using lab processing [31].

The technologies for c-Si solar cells of heterojunction and the interdigitated back contact will gain an increasing market share due to their high power conversion efficiency. The cells fabricated with the heterojunction technology and Si are named as SHJ solar cells. The SHJ solar cell is typically designed with two-side-contacted electrodes [16]. In the SHJ solar cells, the wafer surfaces are passivated with thin semiconducting film, in common cases intrinsic amorphous Si layers [33], to reduce the recombination loss at the interface contributing to a high V_{oc} then high efficiency. The Si layers are deposited by a common plasma enhanced chemical vapor deposition (PECVD) method, and the transparent conductive oxide layer can be fabricated by chemical vapor deposition (CVD) at low temperatures. Metallization is realized by either the Cu platting or screen printing. In 2015, Kaneka reported 25.1% and 24.5% efficiency for SHJ solar cells area of 152 cm^2 and 239 cm^2, respectively, with the Cu plated electrodes [34, 35]. Meyer Burger has reported their champion cell efficiency of 24% on an area of 244.32 cm^2 with bifacial and rear emitter configuration and screen-printing metallization [36]. The champion 60-M2-size-cell module power of 335 W has also been reported with the smart wire contact and white back sheet [36].

The interdigitated back contact technology is used in the silicon solar cells, named as IBC solar cells, to avoid the metal shadowing loss from the fornt surface and thus improving the short circuit current (J_{sc}) [17]. The IBC solar cells are investigated in the homo- and heterojunction configurations. The homojunction IBC solar cells have diffused n$^+$ and p$^+$ regions and the related interdigitated contact electrodes are integrated at the rear side. The heterojunction IBC (HJ-IBC) solar cells combined the advantages of the SHJ solar cell with high V_{oc} and the IBC cell with high J_{sc}. A cell efficiency of 26.6% has been demonstrated by Kaneka in 2017 for passivated contact HJ-IBC solar cell with the designated area of 180 cm^2 [17]. For the IBC solar cell, the high efficiency potential is accompanied by the complicated fabrication process which needs adaption for the mass production.

Based on the single junction solar cells, tandem solar cell is an option to improve the limitation efficiency with more efficient conversion from sunlight to electricity. The perovskite/silicon tandem solar cells have been widely investigated due to the wider absorption range from the solar spectrum compared to single junction solar cell [37, 38]. The fully texture monolithic perovskite/silicon tandem solar cells have achieved 25.2% power conversion efficiency. Besides the tandem stricture, the bifacial design can convert the sunlight incident from both side of the device [39, 40]. Jinko Solar has reported its bifacial cells with front efficiency of 22% and rear efficiency of 15.5%, resulting in a bifaciality of 70% for the p-type PERC cell with passivating contact technology [41].

According to published forecasts, in next ten years, the monocrystalline Si wafer will fast dominate the PV market. Especially, the widely used n-type monocrystalline Si wafer for high efficiency c-Si solar cells will gain increasing market share due to the cost reduction. To further reduce the cost, the wafer will be optimized to be 30-35 μm thinner and larger than the current M2 size (156.75 mm ×156.75 mm). Development of wafer has to be combined with the upgrades of the existing production tools. PERC cell family, including the cells with passivated contact on n-type monocrystalline wafer, will be the mainstream in the PV market with the market share above 50%. SHJ and IBC solar cells will show rapid development with a share of above 15 % and 10 %, respectively, by 2029. Meanwhile, the bifacial deign which can be applied to the c-Si solar cells of PERC, SHJ, IBC, even silicon tandem solar cells will gain approximately 60% share of the PV market by 2029 due to the more effective use of light [25].

2.2 Silicon heterojunction solar cells

As shown in section 2.1, PERC cells with passivated contact on n-type monocrystalline wafers, TOPCon solar cells with passivating contact, silicon heterojunction solar cells and cells with interdigitated back contact are all potential candidates to achieve high efficiency performance. Considering the thermal budget reduction and wafer cost reduction, low temperature process of SHJ solar cells have added advantage over the others. The solar cells with heterojunction technology have a good possibility of gaining market share and are widely and intensively studied by increasing research groups in recent years [42-47]. The SHJ technology have had the advantages of utilizing the experience achieved from the well-developed thin-film silicon solar cell technology [34]. The cells fabricated with IBC showed increased market share as well due to the high efficiency achieved with complicated fabrication process which, however, is not friendly to mass production. Considering the further reduction of the number of fabrication process steps and the increase of throughput, SHJ solar cells have high potential for mass production in future. The SHJ technology is compatible with the commercial standard n-type wafers. It is also appropriate for the thin wafers which is beneficial from the structure of SHJ solar cells and its low temperature process. Besides that, the SHJ technology has an excellent module bificiality and superior temperature coefficient [11, 41].

Compared to the homojunction solar cells, one-dimension cell design can be applied in SHJ solar cells due to the excellent surface passivation of the intrinsic layer without patterning steps. There is no trade-off between the sheet resistance and recombination due to the support from the TCO to the lateral conductivity, instead of the doped Si layer accompanied by the increased recombination loss in homojunction solar cells [48].

All advantages mentioned above contribute to the low production cost, or low LCOEs for SHJ-based PV system, which contribute to the competition in PV market [14]. In the following section, the SHJ solar cells will be described in detail.

2.2.1 Conventional SHJ solar cells

Sanyo (now Panasonic) first reported that intrinsic amorphous Si layer was used to passivate the wafer surface with the feathered structure HIT (heterojunction with intrinsic thin-layer), and presented the HIT cell results with efficiency exceeding 20 % with cell size of 101 cm^2 in 2000 [49], 23.7 % efficiency with V_{oc} = 745 mV in 2011, and 24.7 % efficiency with V_{oc} = 750 mV in 2013 [14] for the two-side-contacted design. These achievements clearly show the great potential for the SHJ solar cell development in mass production.

The conventional SHJ solar cell is schematically illustrated in Fig. 2.3 [16]. In the SHJ solar cells, n-type Cz c-Si substrate was used as substrate with the thickness approximately 170 μm after the texturing and cleaning process. The thin intrinsic a-Si layer was deposited as surface passivation layer with PECVD followed by the n- and p- type a-Si layers to form junction and surface field [16, 50]. Then the conventional TCO material, ITO (indium tin oxide) [51], is fabricated by PVD on the front and on the rear, respectively. The TCO at the front should have a high transparency and sufficient conductivity to support the carrier transport as well as serving as an antireflection coating. The rear TCO contacted with the rear metallization should have a low contact resistance with the Si layer and a relative high conductivity due to the lower conductivity of p-type a-Si layer, while as a trade-off it can have a relatively low transparency. After the TCO fabrication, the fingers and busbars are screen printed on the front and the rear side. After the curing step, the SHJ solar cells are ready for the characterization.
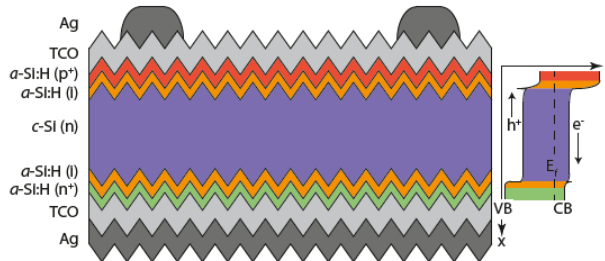

Fig. 2.3. Schematic cross-sections of the conventional silicon heterojunction solar cells [16].

The SHJ solar cell shown in Fig. 2.3 is designed as a mono-facial structure in which carriers are transported form the illuminated area to the grids on the front. The SHJ solar cells are fabricated either in front emitter configuration as shown in Fig. 2.3 where the junction is formed at the front side, or in the rear emitter structure where the p-n junction is formed at the rear side [52].

It is well known that on the front side of SHJ solar cell, there is always a trade-off between the parasitic absorption and conductivity of the layer stack. In front emitter SHJ solar cell, the photo-generated carriers can be simply departed by the junction and collected by the electrodes. While it requires high quality p-type a-Si layers with low absorption and high conductivity to reduce carrier recombination. To reduce the negative effect of the trade-off, fabricating the rear emitter solar cell is one of the approaches. The rear-emitter SHJ cell concept provides new options for more transparent front stacks, and also relaxes the requirements of the front TCO. It also allows for thick p-type layer on the rear side, which is interesting for industrial production.

2.2.2 Alternative Si thin-films and TCO materials in SHJ solar cells

In conventional SHJ solar cells, the application of amorphous Si layer with a band gap close to the c-Si wafer results in parasitic absorption. To improve the situation, more kinds of Si materials have been applied in SHJ solar cells to reduce the parasitic absorption and improve J_{sc} of the device. The n-type nc-Si and n-type nanocrystalline Si oxide (nc-SiO$_x$) have been applied in rear emitter SHJ solar cells as the front surface to improve the transparency and conductivity, thus reducing the current loss and the contact resistance between the Si layers and TCO. For the SHJ solar cells with n-type nc-Si as window layer, an efficiency of 22.6% has been achieved for cells with front AZO and back ITO contacts. Also, an efficiency of 22.5% has been achieved for cells with front/back AZO contacts, which also show the potential of AZO application in SHJ solar cells [53]. For SHJ solar cells with n-type nc-SiO$_x$ as the window layer, a conversion efficiency of 21.6% with the J_{sc} calculated from quantum efficiency (*QE*) measurement of 40.0 mA/cm^2 has been achieved on a cell area of 2 cm × 2 cm [54]. The p-type hydrogenated amorphous Si carbide (a-SiC) is used as the front emitter to reduce the parasitic absorption and reflection loss without degrading the electrical performance of devices [55].

Except the developed Si thin-films, different kinds of TCO materials have also been investigated. Since the mobility of the TCO layer is limited by the material itself, there is always a trade-off between the sheet resistance and the carrier concentration for the front TCO layer resulting in an offset between the *FF* and J_{sc}. Besides, further increasing the carrier concentration to reduce the sheet resistance can reduce the mobility as well [56]. Therefore, high mobility TCO material is expected to be the driving force for the high efficiency solar cells [57, 58]. Since TCO is a typically doped as a n-type material, the contact between TCO and p-type Si layer should also be taken into consideration [59]. TCO development and optimization have important influence on solar cell optimization. Besides the conventionally used ITO, the indium-oxide (In$_2$O$_3$) based materials with high mobility 60-120 cm^2/(V·s) such as Ti / Zr / Mo / W doped In$_2$O$_3$ films [60-64], amorphous indium zinc oxide (a-IZO) with mobility of 115 cm^2/(V·s) [65], and hydrogen-doped indium oxide

(IO:H) with the mobility > 100 cm^2/(V·s) [66, 67] have also been considered as the alternative TCO materials. However, the indium-oxide based TCO materials may be challenging for the mass production of SHJ solar cells due to indium related economic and environmental issues [68-71] and the elevated fabricating temperature above 200ºC. Due to the low deposition temperature (below 200ºC) of Si layers in SHJ solar cells, the TCO layers deposited below 200ºC are needed to avoid the potential damage to the Si layers which in turn restricts the mobility.

Taking these restrictions into account, Al-doped zinc oxide with low cost and low ecological impact is another candidate. However, the AZO has a mobility of approximately 20 cm^2/(V·s) and higher sheet resistance compared to ITO with similar absorption properties. Considering the advantages and shortcomings of the AZO film, Bivour et al. have done some simulations on solar cell performance with AZO. The simulations show that the TCO material with high sheet resistance of approximately 200 Ω/sq can still lead to an *FF* above 80 % [48, 72]. Meza et al. have reported the application of AZO in SHJ solar cell with the sheet resistance approximately 200 Ω /sq achieving the similar performance compared to the SHJ solar cells with ITO film [53]. These reports show the potential of applying AZO in SHJ solar cells.

2.3 SHJ solar cells with AZO and doped nc-Si

In this work, a two-side-contacted cell design was used to fabricate the SHJ solar cell in the rear emitter configuration which is shown in chapter 3. The 170 µm-thick n-type double side textured Cz Si wafers were used in those cells. In the SHJ solar cells, AZO was used to substitute ITO due to its low cost and low ecological impact. Especially the AZO, sputtered at room temperature, is a promising alternative with potential of low thermal budget and high throughput. For solar cell fabrication, doped amorphous Si layers are typically used to form the p-n junction and back surface field in conventional SHJ solar cells. Doped a-Si layers form a proper ohmic contact with commonly used ITO, however, a-Si layer may be less suitable material for contact formation with AZO [73]. The doped nanocrystalline Si layers are expected to improve the contact properties and reduce parasitic absorption simultaneously. In this work the n- and p-type nc-Si layers were studied and implemented in SHJ solar cells. Application of n-type nc-Si layer on the front side reduces the parasitic absorption compared to the cell with n-type a-Si layer and the application of p-type nc-Si layer on the rear side is expected to improve the contact between p-type Si layer and AZO. This work focuses on contacts between the AZO and doped nc-Si layers in SHJ solar cells.

Chapter 3 SHJ solar cell fabrication and characterization methods

This chapter describes the experimental methods for the silicon heterojunction solar cells fabrication process and the characterization methods to investigate the properties of materials and solar cells. This chapter is divided into two sections. The first section presents the experimental details of wafer cleaning, Si layer deposition, aluminum doped zinc oxide sputtering, and metallization in solar cell fabrication. The second section describes the characterization methods used to investigate the properties of Si layers and AZO layers as well as the SHJ solar cells.

3.1 SHJ solar cell fabrication

Silicon heterojunction solar cells fabrication process requires sequent process steps from wafer substrate preparation until metallization. The c-Si wafers are chemical cleaned and swiftly transferred to the Si film deposition system to minimize the oxidation of the wafer surface. The front layer stack of intrinsic a-Si and n-type front surface field (FSF) layers was deposited first without vacuum break. The rear layer stack of intrinsic a-Si and p-type emitter was deposited after flipping the wafer without vacuum break as well. After monitoring the passivation quality of the Si layer stack, AZO sputtering through a shadowing mask was carried out on the Si layers. Silver (Ag) electrodes were either evaporated through the shadow masks or screen-printed using a commercial setup. After curing the solar cells were ready for following characterization. The schematic process flow and the sketch of SHJ solar cell are depicted in Fig. 3.1.
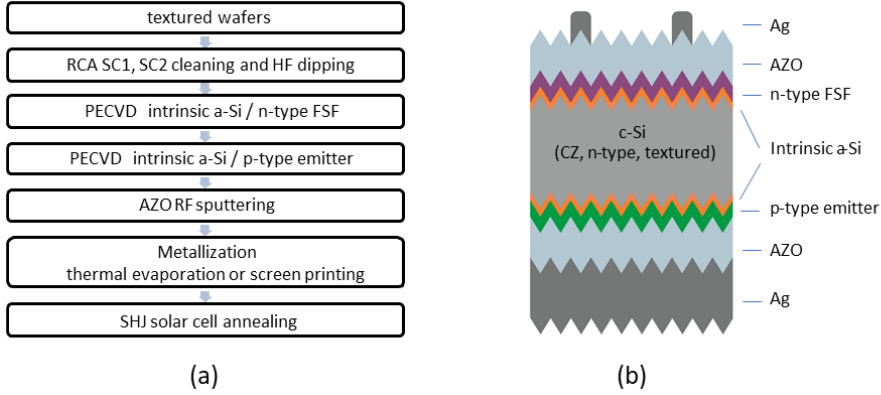
Fig. 3.1. Schematic illustration for (a) SHJ solar cells fabrication process flow; (b) rear emitter SHJ solar cells.

3.1.1 Wafer cleaning

SHJ solar cells are prepared on n-type double side textured Czochralski Si wafers with the thickness of 170 μm and resistivity of 0.5-7 Ω·cm. The SHJ solar cells were prepared in two sizes, one is the industrial M2 (156.75 mm × 156.75 mm) and another one is 19 mm × 19 mm on the approximately 78 mm × 78 mm size wafers which is one quarter from the M2 size wafer after laser cutting. The wafers are also labeled at the rear side prior to the chemical cleaning for the identification in the whole SHJ solar cell fabrication process. Since SHJ solar cell performance is dominated by the interface properties, it is crucial to prepare the growth surface prior to Si layer deposition [74]. In this work, wafers have been cleaned again after the shipment due to the possible contamination and oxidation. First, the wafers are chemically cleaned with RCA Standard Clean (SC) 1 (1 NH$_4$OH: 1 H$_2$O$_2$: 5 deionized water) to remove organic residues and particles, and then RCA Standard Clean 2 (1 HCl: 1 H$_2$O$_2$: 6 deionized water) to remove ionic contaminants for 10 minutes at 75-80°C in each solution [75]. Then the wafers are dipped into 1% HF solution for 5 mins to remove the surface oxide. After rinsing with deionized water and drying with hydrogen, the wafers are directly transferred to the PECVD system for the sequent Si layer deposition.

3.1.2 Silicon layer deposition

In the solar cell fabrication process, Si layers are deposited in the AK 1000 large area in line PECVD system produced by Meyer Burger shown in Fig. 3.2. The figure shows that there are three process modules (PM) for Si layer deposition and two loading modules (LM) for loading and unloading samples. In PM 1 intrinsic and boron-doped Si layers are deposited and in PM 2 and

13

PM 3 intrinsic and phosphorus-doped Si layers are deposited, respectively. With this arrangement Si layer stack of intrinsic amorphous layer and doped Si layer on each side of the wafer can be deposited in sequent without vacuum break. There is a cover layer deposition following the doped Si layer deposition to condition the process modules to avoid the influence of dopants on intrinsic layer. The PECVD system provides the capacity of $9 \times$ M2 (156.75×156.75 mm^2) size wafers in one deposition run.
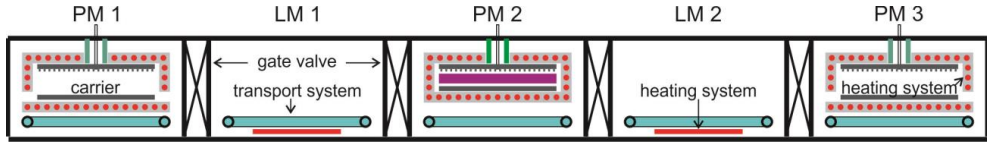
Fig. 3.2. Schematic illustration for the Si layer deposition system of AK 1000 large area in line PECVD system from Meyer Burger Company. The PM 2 is sketched with plasma-on status in the deposition.

In this work, PM 1 and PM 2 are used for the SHJ solar cell development. The p-type a-Si and nc-Si layers are developed in PM 1. The n-type a-Si and nc-Si layers are deposited in PM 2. For the depositions in PM 1 and PM 2, the base pressure is kept in the order of 10^{-9} mbar, the substrate temperature (T_{sub}) is kept at 200°C and the radio frequency (RF) generator for the power supply has a frequency of 13.56 MHz. In the process module, the electrode distance is 16 mm with the area 500 mm $\times$ 500 mm. A sketch of process chamber with plasma on is shown in PM 2 in Fig. 3.2. For the Si layer deposition hydrogen (H_2), silane (SiH_4), phosphine (PH_3), trimethyl borane ($B(CH_3)_3$ or TMB), and diborane (B_2H_6) are used as precursor gases for different doped Si layers with the flow rates and other deposition parameters listed in Table 3.1. The H_2 and SiH_4 are pure, and PH_3, TMB, and B_2H_6 are all supplied with 1% in H_2. The characterization methods are shown in section 3.2 and the Si layer experimental results are presented in chapter 4.

Table 3.1. Experimental parameters for the Si layers deposited in PM 1 and PM 2

	H_2 [sccm]	SiH_4 [sccm]	PH_3 [sccm]	TMB [sccm]	T_{sub} [°C]	Power [W]	Pressure [mbar]	time [s]	thickness [nm]
intrinsic a-Si (PM1)	650	145			200	300+50	2.7	2+20	5
p-type a-Si	500	50		100	200	90	3.5	37	10
p-type nc-Si	990	10		5	200	200	2.5	450	20
intrinsic a-Si (PM2)	650	145			200	300+50	2.7	2+23.5	5
n-type a-Si	500	50	50		200	120	2.5	58	12
n-type nc-Si	990	10	10		200	200	2.5	425	20

3.1.3 AZO sputtering

In this work Al-doped zinc oxide is applied as transparent conductive oxide in SHJ solar cells to support the lateral carrier transport. AZO is sputtered in a vertical in-line sputtering system by radio frequency sputtering of 1 wt.% or 2 wt.% Al_2O_3-doped ZnO ceramic target at different heater temperatures. The sketch of sputtering system is presented in Fig. 3.3. The sputtering is with Argon or Argon with 0.5% Oxygen, varied deposition pressures, power densities, target doping, and substrate temperatures. The sample carrier is dynamically moving in front of the target at certain speed. In order to study AZO properties 80-nm-thick AZO films are sputtered on Corning EAGLE XG glass substrate which has approximately the thickness applied in SHJ solar cells for the Hall effect measurement and transmittance/reflectance measurement.
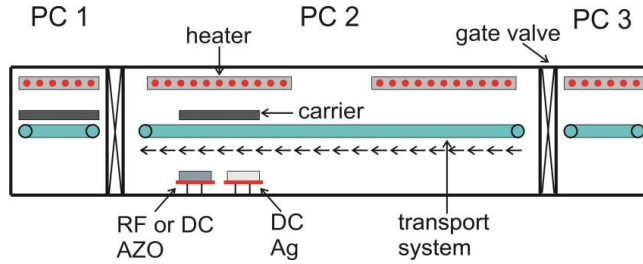
Fig. 3.3. Schematic illustration of aluminum doped zinc oxide (AZO) sputtering system.

3.1.4 Metallization

Two methods were applied for the cell metallization in this work. One is thermally vacuum evaporation of silver through a shadowing mask for cell aperture area of 19 mm × 19 mm. Another one is screen printing with the equipment MT-650TVC from Micro-tec for both cell areas of 19 mm × 19 mm and 156.75 mm × 156.75 mm. The front shadow masks for metallization are shown in Fig. 3.4. For the cells with the area of 19 mm × 19 mm, the whole area of the rear side is coved by the Ag electrode, while for the M2 size cells, intensive fingers were used to reduce the cost. The Ag paste used for screen printing is from Kyoto Elex DD-1760L-359 or NAMICS XH9455-27. After metallization, annealing is done to form ohmic contact between Ag and AZO.
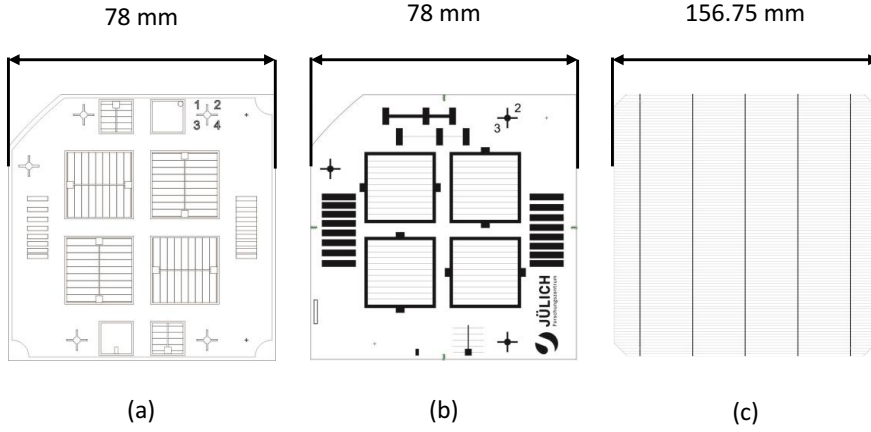
Fig. 3.4. Front shadow masks for Ag evaporation and screen printing: (a) inner busbar design for the 19 mm × 19 mm cells; (b) outer busbar mask design for 19 mm × 19 mm cells; (b) mask for screen printing of 156.75 mm× 156.75 mm (M2) cells.

3.1.5 Finished SHJ solar cells

In this work the SHJ solar cells are prepared in the so-called rear junction configuration, i.e. an n-type layer was used as window layer at the front of the device and the p-n junction was formed at the rear side. By combining different doped Si layers, four kinds of SHJ solar cells with (1) n-type a-Si / p-type a-Si, (2) n-type nc-Si / p-type a-Si, (3) n-type a-Si / p-type nc-Si, and (4) n-type
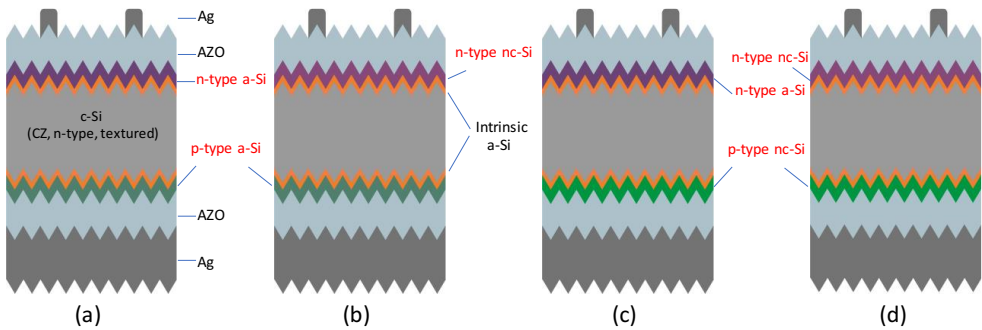
Fig. 3.5. SHJ solar cells with four doped Si layer combinations at the front and rear side: (a) n-type a-Si / p-type a-Si, (b) n-type nc-Si / p-type a-Si, (c) n-type a-Si / p-type nc-Si, and (d) n-type nc-Si / p-type nc-Si.

nc-Si / p-type nc-Si on the front and rear side, respectively, are fabricated as shown in Fig. 3.5. In this way, the AZO contacts to varied doped Si layers were tested in SHJ solar cells.

3.2 Characterization methods

3.2.1 Material characterization methods

3.2.1.1 Thickness

Layer thickness determination is very critical to calculate the parameters for the deposition rate r_d and electrical conductivity σ. There are two ways to measure the layer thickness. One way is with step profiling system of Vecco Dektak 6M Stylus Profiler. For this method, sharp steps between the glass substrate and Si layers have to be created by placing small Si wafer pieces on the glass substrate prior to deposition. In this way layer thickness can be obtained by the 12 μm probe scanning across the sharp step with the relative height difference. This Dektak measurement works validly for layer thickness above 50 nm, however, for the layer thickness below 20 nm used in SHJ solar cells, ellipsometry is more reliable for the thickness measurement [76] described as follows.

3.2.1.2 Spectroscopic ellipsometry

Spectroscopic ellipsometer is engineered to meet the diverse demands for thin-film characterization and important for the in-situ monitoring and process control during solar cell fabrication [77]. The ellipsometer measures the change of polarization after incident light with certain angles interacts with the thin Si films. After the measurement, the parameters of amplitude ratio and the phase difference are obtained. By fitting the parameters within certain models, the parameters for the thin layers can be obtained. In this work, the M-2000 XI spectroscopic ellipsometer with auto angel ESM-300 base from J. A. Woollam was used to characterize the thickness, refractive index and extinction coefficient for the Si layer and AZO.

3.2.1.3 Raman spectroscopy

Raman spectroscopy is a fast and non-destructive method to estimate the Si layer crystalline volume fraction I_c. This measurement is based on the interaction mechanism between the incident radiation and the materials. The incident photon can be scattered inelastically when interacting with the material by either emitting (Stokes scattering) or absorbing a phonon (anti-Stokes scattering). The energy shift indicates the vibration modes of the lattice, which correlates with the microstructure of the Si thin films [78]. In this work, the samples are deposited on Corning EAGLE glass and measured with a Renishaw in Via Raman Microscope with 532 nm Diode-pumped solid-state laser. The crystalline volume fraction I_c of the Si thin film is determined as the ratio between

the integrated area of crystalline and the total integrated area of crystalline and amorphous in the Raman shift range of 400-560 cm^{-1} [79].

3.2.1.4 Electrical conductivity

The lateral conductivity σ of Si layers was measured at room temperature in dark with two thermally evaporated coplanar silver contacts. For a given Si layer thickness and a 0.5 mm gap between the silver contacts, the conductivity can be acquired at a given voltage. This measurement could measure the lateral current flow which is by orders of magnitudes higher compared to the current flow vertically through the contact between silver and Si film, in this way its contact resistance can be negligible. However, for solar cells the vertical conductivity in Si layer is more relevant, and the conductivity in lateral and vertical directions with respect to the film growth could be significantly different. Therefore, the lateral conductivity measured currently can only be used as a monitor to the Si layer properties.

3.2.1.5 Photothermal Deflection Spectroscopy (PDS)

Photothermal deflection spectroscopy was used as a highly sensitive tool for the investigation of optical absorption. The absorption in band tails and in sub-band gap energy range can be achieved simultaneously [80]. The PDS setup consists of a cavity filled with carbon tetrachloride (CCl_4) surrounding the sample. The monochromatic chopped light beam in the wavelength range of 310-2600 nm illuminates the sample with the light source combination of halogen lamp and xenon lamp. The heat generated in the sample from the light absorption can be transferred to the surrounding CCl_4 fluid, which contributes to the change of refractive index in CCl_4. The variation of refractive index can be detected by the passing laser beam and the absorption profile of the sample can be obtained. To reduce the influence of the glass the measurement is followed by the phase correction procedure using chopped light and lock-in technique. This PDS measurement can be used for the accurate characterization of the absorption property in the low energy range.

3.2.1.6 Optical photometry

The transmittance $T(\lambda)$ and reflectance $R(\lambda)$ of layers on glass were measured using ultraviolet–visible-near infrared (UV-Vis-NIR) Perkin-Elmer LAMDA 950 photo spectrometer with a spectra range of 250-2500 nm. The integrating sphere with its interior covered by a diffused white reflective coating is installed to guarantee the uniform scattering. Baseline measurement was performed prior to the transmittance and reflectance measurements with no sample in front of the opening entrance of the sphere. For the transmittance measurement, the samples with layer side towards the direction of light incident are positioned in front of the opening entrance of the sphere, which collects the transmitted light to the detector. For the reflectance measurement, the samples are placed at the opposite side of the opening entrance of the sphere with the layer side towards the direction of light incident as well to collect the reflected light. In this case, both transmittance

and reflectance measurement are not taking the glass substrate into consideration. Therefore, the spectral absorptance can be calculated as $A(\lambda)=1-T(\lambda)-R(\lambda)$.

3.2.1.7 Hall effect measurement

Hall effect measurement is used to determine the carrier density n, resistivity ρ, and mobility μ. When a current perpendicular to the applied magnetic field cross the electrical conductor, the moving path of the charge carriers is curved and produces an electrical field perpendicular to the direction of current flow and the applied magnetic field. After an equilibrium is reached between the effects of electrical field and magnetic field, the charge carriers will cross the electrical conductor in a straight line. Therefore, with the known sample thickness the carrier density n, resistivity ρ, and mobility μ of the samples can be acquired. In this work Hall effect measurements are applied for the characterization of the electrical properties of AZO layers. The AZO samples are prepared on Corning EAGEL glass with the size of 10 mm × 10 mm. During Hall effect measurement the four contact pins are located at the four corner points of the sample. The contact between the pins and the AZO must be guaranteed as ohmic contact.

3.2.1.8 Quasi steady-state photo conductance (QSSPC)

Effective minority carrier lifetime τ_{eff} of photogenerated carriers is measured with the Sinton Consulting WCT-120 QSSPC setup. Effective carrier lifetime is limited by a combination of the lifetimes being contributed by several recombination processes related to bulk and surfaces of a Si wafer. The bulk recombination processes include Auger recombination with the lifetime of τ_{Auger}, radiative recombination with the lifetime of τ_{rad}, and defect assisted or Shockley-Read-Hall (SRH) recombination (recombination through the impurities and defects in bulk) with the lifetime of τ_{SRH}. The surface recombination is commonly through the impurities and defects at surfaces of the wafer, which is typically expressed via surface recombination velocity S. In this way the effective carrier lifetime can be expressed as follows [81]

$$\frac{1}{\tau_{eff}} = \frac{1}{\frac{1}{\tau_{Auger}}+\frac{1}{\tau_{rad}}+\frac{1}{\tau_{SRH}}} + \frac{S_{front}}{W} + \frac{S_{back}}{W}, \tag{3.1}$$

where W is the wafer thickness. Normally the effective carrier lifetime is extracted at the excess carrier density $\Delta n = 1\times10^{15}$ cm^{-3}. The surface recombination velocity S depends on the surface passivation and excess carrier density. With the development of wafer production crafts, the wafer bulk lifetime τ_{bulk} which is a combination of τ_{Auger}, τ_{rad}, and τ_{SRH} is much higher than the lifetime from the wafer surface recombination. Therefore, the effective carrier lifetime indicates the surface passivation, which is crucial to the good performance of SHJ solar cells.

For the lifetime measurement with QSSPC, there are two modes for the sample measurement. One is quasi-steady-state mode for the sample lifetime less than 200 μs. Another one is the transient mode for the sample lifetime more than 200 μs. In this work, transient mode is used for the characterization of passivation quality. With this mode, the short light pulse decays to darkness

rapidly, the sheet conductance versus time is measured after the light pulse by the RF coil, which is translated into excess carrier density Δn at each moment, finally by taking the derivative of the Δn over time the lifetime time can be determined as

$$\tau = -\frac{\Delta n}{d\Delta n/dt}.$$ (3.2)

For more information on lifetime, Ref. [82] is recommended.

3.2.2 SHJ solar cell characterization methods

3.2.2.1 Transfer length method (TLM)

Transfer length method was used to measure the contact resistance at the interface of the contact layers with the automatic measurement equipment [83]. The TLM structure (at the edge of the quarter wafer size cells, shown in section 3.1) consists of 8 parallel silver stripes with a diameter of 10 mm in length and 2 mm in width. The spacing L between the adjacent stripes are 523, 630, 728, 828, 930, 1037, and 1137 μm, respectively. By plotting the total resistance R_t between the adjacent silver stripes versus the adjacent spacing L, the contact resistance R_c is calculated by the intersection of the linear interpolation on the y-axis as shown in Fig. 3.6 (a). The specific contact resistance ρ_c can be calculated with R_c, wafer thickness W and transfer length L_T obtained from the intersection of the linear interpolation on the negative x-axis. The assumed current flow routes for the contact between Ag and AZO and the contact between AZO and Si layer are indicated in Fig. 3.6(b) and 3.6(c). Simultaneously the sheet resistance R_{sheet} of AZO can be obtained from the slope of the dependency and the wafer thickness W. The relationship between the parameters is determined by the following expression
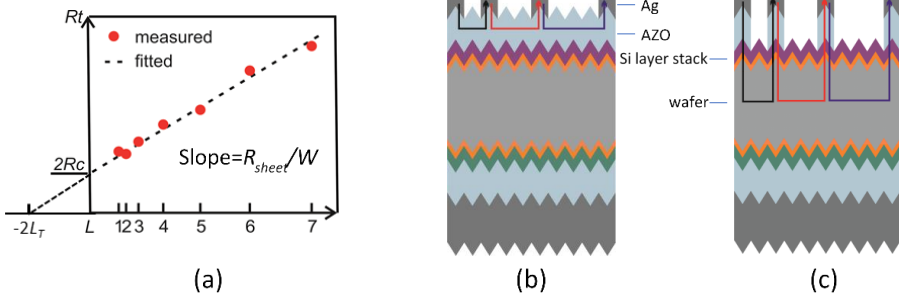

(a)   (b)   (c)

Fig. 3.6. Schematic illustration of (a) principle for the extracting of contact resistance from TLM measurement; (b) the assumed current flow route for the contact between AZO and silver; and (c) the assumed current flow route for the contact between AZO and silicon layers.

$$R_t = \frac{R_{sheet}}{W}L + 2R_c, \tag{3.3}$$

$$\rho_c = R_c L_T W. \tag{3.4}$$

3.2.2.2 Current density-voltage (J-V) characteristics

The current density-voltage characteristic for SHJ solar cell are measured by the "LOANA" characterization setup from pv-tools equipped with a SINUS 220 Wavelabs light source under standard test condition (25°C, AM 1.5G, 100 mW/cm²). The samples are positioned on a copper plate which is connected to a temperature controlling system within the temperature range of 25°C to 85°C. From the J-V measurement, dark J-V curve, light J-V curve, and J_{sc}-V_{oc} curves are obtained. By fitting the dark J-V data with diode mode, the saturation current density J_0 and the diode ideality factor n_{if} are determined. The parameters of solar cell conversion efficiency η, open circuit voltage V_{oc} (J=0), short circuit current density J_{sc} (V=0), and fill factor FF are obtained with light J-V curve. Simultaneously the shunt resistance R_{sh} and series resistance R_s are obtained from the J-V measurement. The relationships among the parameters are list as follows

$$FF = \frac{V_{mpp}J_{mpp}}{V_{oc}J_{sc}}, \tag{3.5}$$

where V_{mpp} and J_{mpp} are the voltage and current density, respectively, at the maximum power point (MPP). The efficiency is given by

$$\eta = \frac{P_{max}}{P_{in}} = \frac{V_{oc}J_{sc}FF}{P_{in}}, \tag{3.6}$$

where P_{max} is the power at maximum power point, and P_{in} is the input power of the solar cell.

3.2.2.3 Quantum efficiency (*QE*)

The spectra resolved quantum efficiency allows detailed monitoring of optical absorption and charge carrier extraction in SHJ solar cells. The external quantum efficiency (*EQE*) describes the probability of the generated charge carriers respect to the incident light at certain wavelength

$$EQE\ (\lambda) = \frac{J_{sc}(\lambda)}{q\phi_{inc}(\lambda)}, \tag{3.7}$$

where q is the electron charge and Φ_{inc} is the incident photon flux at certain wavelength.

The internal quantum efficiency (*IQE*) describes the probability of the generated charge carriers respect to the absorbed light at certain wavelength

$$IQE\ (\lambda) = \frac{J_{sc}(\lambda)}{q\phi_{abs}(\lambda)}, \tag{3.8}$$

where Φ_{abs} is the absorbed photon flux at certain wavelength.

The *IQE* excludes the optical loss from the reflectance and transmittance compared to *EQE*. The relationship between *EQE* and *IQE* is defined as

$$IQE = \frac{EQE}{1-R-T}, \tag{3.9}$$

where R and T is the reflectance and transmittance of SHJ solar cells, respectively. The T can be omitted due to the thick base absorption and metallization structure at the rear side of the solar cell. Therefore, the Eq. 3.8 can be described by

$$IQE = \frac{EQE}{1-R}. \tag{3.10}$$

The short circuit current density J_{sc} is obtained by integration of the product of electron charge, *EQE* and incident AM1.5G spectrum via

$$J_{sc} = \int q\ EQE(\lambda)\phi_{inc}d\lambda. \tag{3.11}$$

Chapter 4 Doped nc-Si and AZO for carrier selective contacts in SHJ solar cells

This chapter describes the fundamental study on the doped nc-Si and Al-doped zinc oxide layers for carrier selective contacts in SHJ solar cells. The first section describes development of n-type and p-type nc-Si layers by means of variations in deposition parameters as discharge power, gas pressure, gas flow rate ratio, and layer thickness. The second section presents optical and electrical properties of AZO films sputtered with different pressures, power densities, heater temperatures, target doping concentrations, and precursor gas mixtures.

4.1 Doped nc-Si for SHJ solar cells

As an alternative to the conventional a-Si layers used in SHJ solar cells, doped nc-Si layers with lower parasitic absorption and higher conductivity were developed and implemented into SHJ solar cells in this work. The n-type nc-Si layers were developed for window layer with low parasitic absorption for J_{sc} improvement. The p-type nc-Si layers, as well as n-type nc-Si layers, were developed to form proper contact to AZO film. For the depositions of doped nc-Si layers, H_2, SiH_4, PH_3, TMB, and B_2H_6 have been used as precursor gases. Generally, the ratios between the gas flow rates ϕ are used to describe the gas parameters during deposition. The gas flow rate ratio between ϕ_{SiH4} and ϕ_{H2} is described as r_{SiH4}

$$r_{SiH_4} = \emptyset_{SiH_4}/\emptyset_{H_2}. \tag{4.1}$$

The gas flow rate ratio between ϕ_{PH3} and ϕ_{SiH4} is described as r_{PH3}

$$r_{PH_3} = \emptyset_{PH_3}/\emptyset_{SiH_4}. \tag{4.2}$$

The gas flow rate ratio between ϕ_{TMB} and ϕ_{SiH4} is described as r_{TMB}

$$r_{TMB} = \emptyset_{TMB}/\emptyset_{SiH_4}. \tag{4.3}$$

The gas flow rate ratio between ϕ_{B2H6} and ϕ_{SiH4} is described as r_{B2H6}

$$r_{B_2H_6} = \emptyset_{B_2H_6}/\emptyset_{SiH_4}. \tag{4.4}$$

To investigate the properties of doped nc-Si layers, the n-type and p-type nc-Si layers were prepared on Corning glass substrates directly for deposition rate measurement and on the intrinsic a-Si layer coated glass substrates to provide the similar growth surface as for the deposition in SHJ solar cells. The samples are schematically illustrated in Fig. 4.1. The intrinsic a-Si interlayer was deposited with the parameters identical to the parameters for the passivation layer deposited in solar cells. Then the samples were characterized for the deposition rate r_d, crystalline volume fraction I_c, and conductivity σ for the sequent implementation in SHJ solar cells.

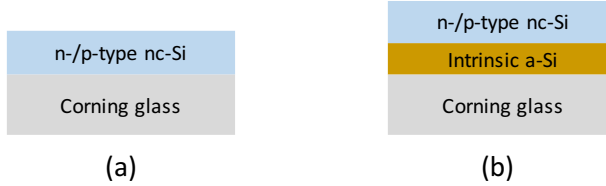|	
n-/p-type nc-Si	n-/p-type nc-Si
	Intrinsic a-Si
Corning glass	Corning glass
(a)	(b)

Fig. 4.1. Schematic illustration for n-type or p-type nc-Si layers deposited on Corning glass (a) without intrinsic a-Si layer; (b) with intrinsic a-Si layer underneath.

4.1.1 n-type nanocrystalline silicon layer

The n-type nc-Si layers were developed with variation of discharge powers, r_{SiH4}, and r_{PH3}. The substrate temperature and deposition pressure for n-type nc-Si layers were unchanged at 200°C and 2.5 mbar, respectively, as shown in Table 3.1 in section 3.1.2. The r_d, I_c, and σ variations of n-type nc-Si layers as a function of r_{SiH4} and power are shown in Fig. 4.2 with the constant r_{PH3} of 1. For the n-type nc-Si layers deposited on glass substrates, the r_d increases with the increase of r_{SiH4} at the deposition powers of 200-500 W, and the r_d is almost unchanged for n-type nc-Si deposited with 100 W when the r_{SiH4} increased from 0.01 to 0.02. Whereas the I_c and σ of the Si films decrease with the increase of r_{SiH4} except for the samples prepared with the power of 500 W which shows increased I_c and σ with the r_{SiH4} increased from 0.01 to 0.02. In general, the Si films deposited on the intrinsic a-Si layers show similar dependencies as compared to the samples deposited directly on glass, but with lower I_c and σ values which is related to the effect of a-Si on the nanocrystalline nucleation [84]. The low I_c for the n-type nc-Si layer deposited on intrinsic a-Si is affected by the intrinsic a-Si layer underneath and its influence on the Raman measurement with 532 nm laser.

Considering the required I_c and σ for nc-Si layer, the Si films prepared with r_{SiH4} of 0.01 and 0.02 were investigated in detail. Deposition rate, crystalline volume fraction, and conductivity as a function of discharge power are shown in Fig. 4.3. Generally, the n-type nc-Si layers deposited with r_{SiH4} of 0.01 shows higher I_c and σ, and lower r_d than the n-type nc-Si layer deposited with r_{SiH4} of 0.02 with the power increasing from 50 W to 300 W. The n-type nc-Si layers deposited on the intrinsic a-Si coated surface shows lower I_c and σ than the n-type nc-Si layers deposited on the glass directly due to the effect of amorphous Si. The variation trends for the layers deposited on the glass or amorphous Si are quite similar. For the n-type nc-Si layers deposited with r_{SiH4} of 0.01, the r_d, I_c, and σ for the layers deposited on glass increase with the power increase form 50 W to 200 W, and then are saturated or slightly decrease with the further increase of power. While for the layers deposited on the amorphous surface, the variation trends for the r_d and I_c versus power are not obvious, and the σ increases significantly with the power increased from 100 W to 200 W before saturation. For the n-type nc-Si layers deposited with r_{SiH4} of 0.02, the r_d, I_c, and σ for the layers deposited on glass increase with the increase of power. For the n-type nc-Si layer deposited
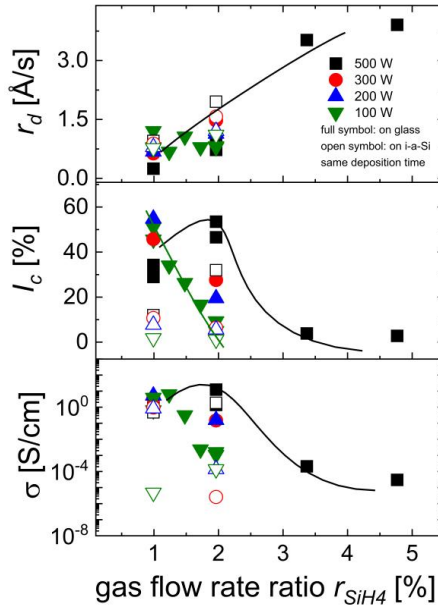

Fig. 4.2. Deposition rate, crystalline volume fraction, and conductivity of n-type nc-Si layers as a function of gas flow rate ratio r_{SiH4} in the power range of 100 W to 500 W.
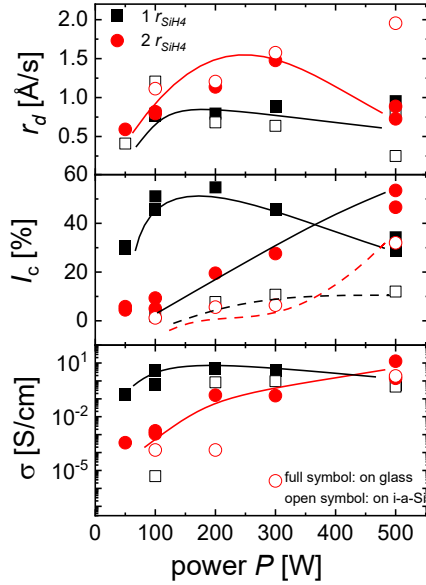
Fig. 4.3. Deposition rate, crystalline volume fraction, and conductivity of n-type nc-Si layers as a function of power from 50 W to 500 W with r_{SiH4} of 0.01 and 0.02.

with r_{SiH4} of 0.02 on a-Si surface, the r_d, I_c, and σ show the increase trend with the increase of power. There are the exceptions of the r_d drop at the power of 500 W for the layer deposited on glass and the slight decrease of σ for the layers deposited on the intrinsic a-Si in the power range of 100-300 W.

Out of the results shown in Fig. 4.3, the n-type nc-Si layer deposited on intrinsic a-Si with r_{SiH4} of 0.01 at the power of 200 W shows the highest conductivity. These parameters were chosen for layers deposition applied in SHJ solar cells.

Dependencies of r_d, I_c, and σ on r_{PH3} for the n-type nc-Si layers deposited with 200 W on intrinsic a-Si are presented in Fig. 4.4. There is no influence of r_{PH3} varied in the range of 0.5-2 on r_d, I_c, and σ observed. The I_c of n-type nc-Si layer is below 10 %, the σ is approximately 10^{-1} S/cm, and the r_d is approximately 0.8 Å /s. Taking this into consideration, the r_{PH3} of 1 was used combined with the r_{SiH4} of 0.01 and power of 200 W for n-type nc-Si layers deposition in SHJ solar cells.
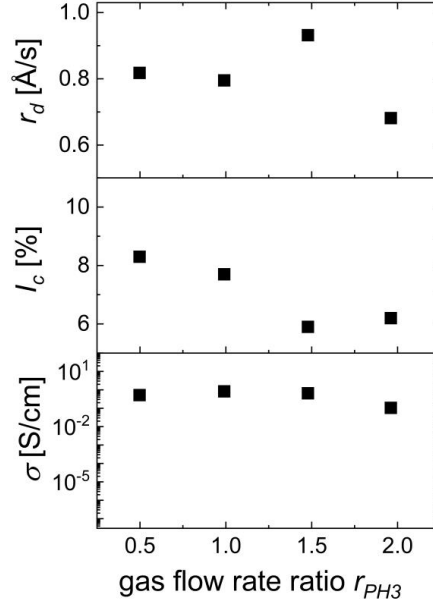
Fig. 4.4. Deposition rate, crystalline volume fraction, and conductivity variations of n-type nc-Si layers as a function of gas flow rate ratio r_{PH3}.
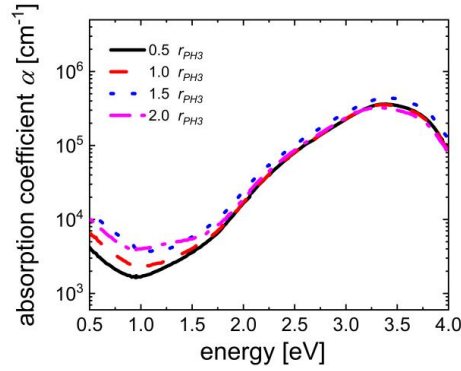
Fig. 4.5. Absorption coefficient as a function of energy for n-type nc-Si layers deposited with the gas flow rate ratio r_{PH3} in the range of 0.5-2.

Optical properties of the n-type nc-Si layers were characterized with PDS measurement. Dependence of absorption coefficient on energy are presented in Fig. 4.5 for n-type nc-Si layers deposited with the r_{PH3} range of 0.5 to 2. In the energy region of 0.5-2 eV, the absorption

coefficient increases with the increase of r_{PH3}. For the energy above 2 eV there is slight difference in the absorption coefficient with the increase of r_{PH3}. Since n-type nc-Si layer was used as window layer in the solar cells, the absorption in the high energy region is critical to the short circuit current of the solar cells. Thus, the r_{PH3} variation in the range of 0.5-2 does not play a big role on the parasitic absorption of the n-type nc-Si layer in the short wavelength region. Therefore, considering the r_{PH3} influence on the optical properties, the n-type nc-Si layer deposited with r_{PH3} of 1was chosen for application in SHJ solar cells, which is consistent with the previous development.
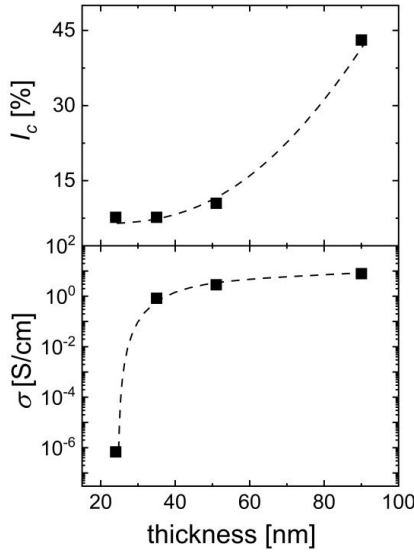

Fig. 4.6. Crystalline volume fraction and conductivity as a function of the thickness of n-type nc-Si layers deposited on intrinsic a-Si coated glass.

The n-type nc-Si layer thickness series was prepared with r_{PH3} of 1. Dependencies of I_c and σ on layer thickness are presented in Fig. 4.6. With the increase of Si layer thickness, I_c of n-type nc-Si layer increases from approximately 8 % to 43 % and σ increases from approximately 10^{-7} to 10^0 S/cm. Conductivity increases significantly as the layer thickness increases from 24 nm to 35 nm, which is typical transition from predominantly amorphous nucleation layer to nanocrystalline layer.

Considering the minimization of parasitic absorption in the functional layers of a cell, the thickness of the n-type window layer should be as low as possible while providing sufficient field effect to form n-n+ junction. A approximately 20-nm-thick n-type nc-Si on the intrinsic a-Si layer was initially chosen for the SHJ solar cell fabrication which corresponds to the 35 nm for the intrinsic a-Si / n-type nc-Si stack on glass in this case. The difference is related to correction factor 1.7 when planar glass substrate is replaces with textured wafer [85].

In conclusion, considering the electrical and optical properties of the n-type nc-Si layers, the following deposition parameters have been chosen for n-type nc-Si layers in SHJ solar cells: substrate temperature of 200°C, power of 200 W, r_{SiH4} of 0.01, r_{PH3} of 1, pressure of 2.5 mbar, and thickness of 20 nm.

4.1.2 p-type nanocrystalline silicon layer

Based on the development of n-type nc-Si layer, the p-type nc-Si layers were developed at the same power of 200 W and temperature of 200°C. Trimethyl borane or diborane were used as doping precursor gases for the p-type nc-Si layer depositions. Dependencies of r_d, I_c, and σ on r_{TMB} are presented in Fig. 4.7. The r_d, I_c, and σ of p-type nc-Si layers deposited on glass substrate shows decrease trend with the increase of r_{TMB} for both the center and corner positions where the substrates placed in the deposition chamber. The p-type nc-Si layers deposited on intrinsic a-Si show lower value due to the intrinsic a-Si layer growth surface. For the layers deposited on glass, with the increase of r_{TMB} from 0 to 0.5 the r_d and σ first increase, then decrease with the further increase of r_{TMB}. The I_c decreases with the increase of r_{TMB}. For the p-type nc-Si deposited on intrinsic a-Si, the r_d of the samples prepared at the center and the corner of the deposition chamber shows opposite trends versus r_{TMB}, while the variation of r_d is in a very narrow range. The I_c decreases with the increases of r_{TMB}. The σ increase first then decrease with the increase of r_{TMB}.
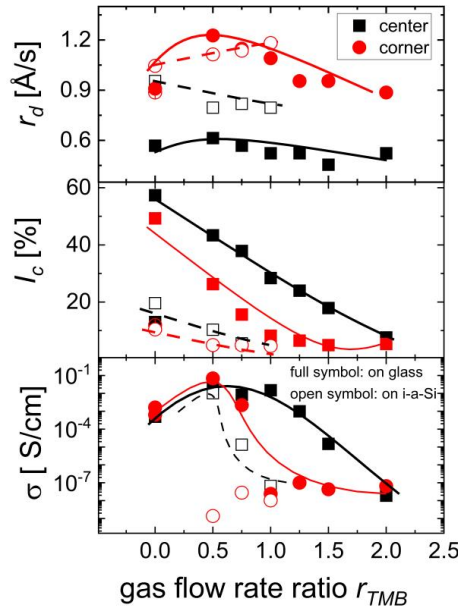

Fig. 4.7. Deposition rate, crystalline volume fraction, and conductivity variations of p-type nc-Si layers as a function of gas flow rate ratio r_{TMB}. Center and corner mean the sample position in deposition chamber.

For the r_{TMB} series of p-type nc-Si layer, an obvious uniformity was observed between the p-type nc-Si layers prepared at the corner and center of the deposition chamber. Thus, in order to find more appropriate deposition regime a series with variation of precursor gas pressure was prepared for p-type nc-Si layers. Dependencies of r_d, I_c, and σ on deposition pressure are presented in Fig. 4.8. With the increase of deposition pressure, the r_d decreases first and then increases which is opposite to the variation of I_c. Conductivity shows increase trend with the increase of pressure. The values of r_d, I_c, and σ for the p-type nc-Si layer prepared at the center are higher than that for the layers prepared at the corner of the deposition chamber. Results of pressure series shows that the uniformity problem cannot be simply solved by varying deposition pressure.

As an alternative boron doping source, B_2H_6 has been tested for p-type nc-Si layer deposition for the initial investigation. Results for the B_2H_6 series with p-type nc-Si deposited with r_{B2H6} of 0.5 are presented in Fig. 4.9. The p-type nc-Si layers deposited with TMB or B_2H_6 on glass were used as reference. Deposition time for p-type nc-Si layer deposited with B_2H_6 on intrinsic a-Si was reduced from 440s to 200s. Using the same deposition parameters to the deposition with TMB, the p-type nc-Si layer deposited with B_2H_6 on glass shows lower r_d, I_c, and σ. The p-type nc-Si layers deposited on intrinsic a-Si shows extremely low I_c and σ values. Further optimization is needed for the implementation of p-type nc-Si deposited with B_2H_6 for solar cells.
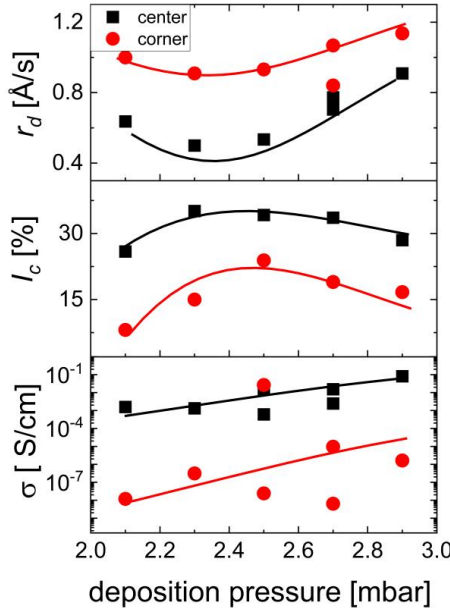

Fig. 4.8. Deposition rate, crystalline volume fraction, and conductivity variations of p-type nc-Si layers as a function of deposition pressure with TMB.
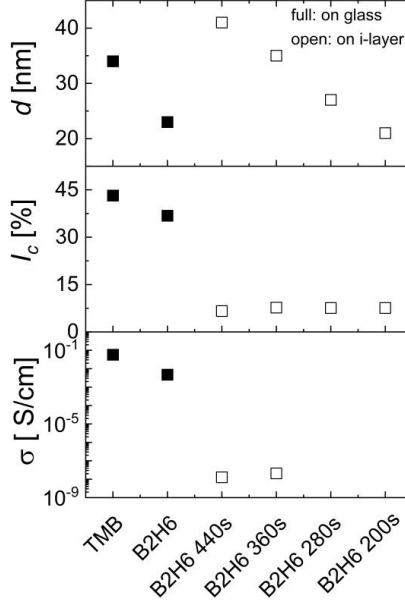
Fig. 4.9. Thickness, crystalline volume fraction, and conductivity variations of p-type nc-Si layers deposited with TMB or B_2H_6 on glass, and with B_2H_6 on intrinsic a-Si and varied deposition times of 440s, 360s, 280s, and 200s, respectively.

In conclusion, considering the electrical properties of the p-type nc-Si layer, the deposition parameters are chosen as follows: substrate temperature of 200ºC, power of 200 W, r_{SiH4} of 0.01, r_{TMB} of 0.5, pressure of 2.5 mbar, and thickness of 20 nm for the SHJ solar cell fabrication. The optical properties of the p-type nc-Si layers were not addressed here due to the rear-emitter structure of the solar cells where the absorption property is not critical. However, for the further optimization for very high efficiency solar cells, the absorption property of the p-type Si layer has to be taken into consideration.

4.2 AZO for SHJ solar cells

Al-doped zinc oxide, as more environmentally friendly, abundant and less costly material, is an attractive alternative to ITO in silicon heterojunction solar cells [16, 86]. Especially AZO prepared at room temperature has potential to reduces the thermal cost and improves the throughput. The techniques of magnetron sputtering, chemical vapor deposition (CVD) [87], and atomic layer deposition (ALD) [88] can be applied for the TCO deposited under 200ºC. Among the techniques, the radio frequency (RF) magnetron sputtering is one well-developed technique to deposit AZO film due to its high potential of better optical and electrical properties in AZO films with room

temperature process [89] and providing the material with uniform surface and a good adherence [90]. Nevertheless, the AZO sputtering process can lead to the passivation damage of the Si layer underneath which will be addressed in chapter 6.

4.2.1 AZO sputtered with varied pressures and power densities

To study the influence of the sputtering pressure on the optical and electrical properties of AZO films, pressure series of 0.1, 0.3, 0.5, 1 and 2 Pa has been prepared on 1.1-mm-thick Corning EAGLE glass. The pressure series was prepared with the 1 wt.% AZO target and 2.0 W/cm^2 power density relate to the target area of 75 cm × 10 cm at room temperature. Depositions are performed in dynamic mode with the carrier moving back and forward in front of the target at the speed of 4.5 mm/s with 5 steps. The thickness as a function of sputtering pressure is shown in Fig. 4.10. With the increase of sputtering pressure, the AZO layer thickness decreases which is due to decreased average ion energy and, therefore, reduced sputtering yield.
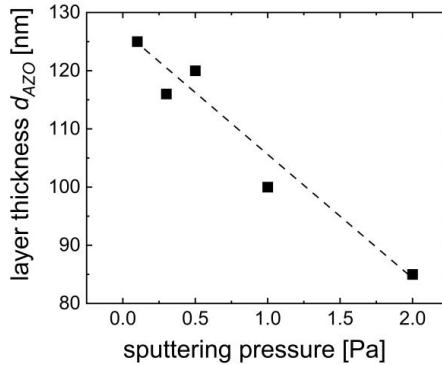
Fig. 4.10. Thickness of AZO layer as a function of sputtering pressure from 0.1 Pa to 2 Pa.

Since the AZO in SHJ solar cells will go through the annealing which will be typically carried out after metallization, the AZO samples on glass were annealed as well to examine the variation of the AZO properties. Thus, optical and electrical properties of AZO after annealing are evaluated. Optical properties of AZO layers deposited with varied sputtering pressures after annealing are presented in Fig. 4.11. The films sputtered with the pressure of 0.3-1 Pa show similar transmittance *T* and absorptance *A*. The absorptance exceeds 80 % in the wavelength range of 400-1300 nm and
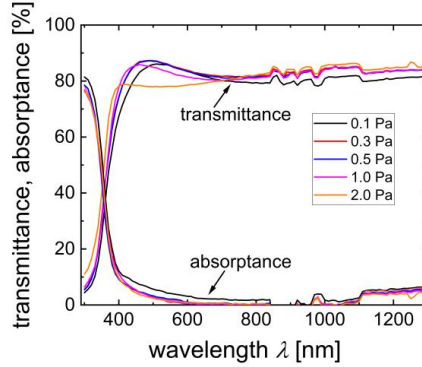
Fig. 4.11. Transmittance and absorptance spectra of AZO films after annealing as a function of sputtering pressure from 0.1 Pa to 2 Pa. The unusual shape in the curves is from the measurement setup.

is below 5 % in the wavelength range of 450-1300 nm. The films sputtered with 0.1 Pa shows lower transmittance and higher absorptance compared to the films sputtered at 0.3-1 Pa due to the higher thickness. The films sputtered at 2 Pa with thinner layer shows low transmittance in the wavelength range of 400-600 nm which is presumably due to the influence of the high pressure on the microstructure of the AZO film.

The carrier mobility μ, carrier concentration n and resistivity ρ evaluated from Hall measurement for AZO film deposited with different pressures measured after annealing are shown in Fig. 4.12. The carrier concentration has no obvious dependency on pressure until the decrease at the pressure of 2 Pa. The resistivity increases with the increasing sputtering pressures, accompanied with the decrease of mobility. Increase of sputtering pressure increases the particle density which results in the reduction of the mean free path and the energy of the particles. Speculatively higher ion energy at low sputtering pressures contributes to the improvement in crystallinity and the network relaxation. These improvements contribute to the higher mobility and lower resistivity of AZO films.

From the equation of $R_{sheet} = 1/qn\mu d_{AZO}$ reduction of sheet resistance R_{sheet}, reducing resistivity as well, can only be achieved with the increase of μ and n since the q is the electron charge and thickness d_{AZO} is fixed for the antireflection purpose. Thus, the trade-off between μ and n are tested for the properties of AZO layers. Considering the requirement for high mobility, sputtering

Fig. 4.12. Carrier concentration n, carrier mobility μ, and resistivity ρ from Hall measurement of AZO films annealing as a function of sputtering pressure from 0.1 Pa to 2 Pa.

pressure of 0.1 Pa has been chosen as the pressure for the AZO development due to the highest mobility in the pressure series.
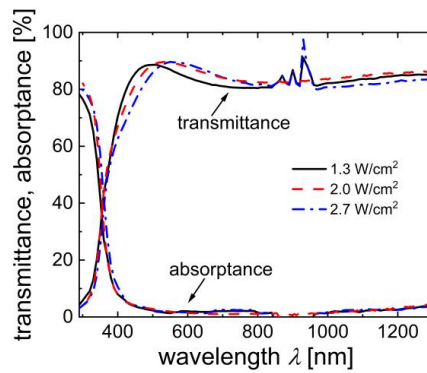
Fig. 4.13. Transmittance and absorptance spectra of AZO films after annealing as a function of sputtering power densities of 1.3, 2.0, and 2.7 W/cm^2, respectively.

Influence of power densities on AZO properties was studied as well. Power densities of 1.3, 2.0, and 2.7 W/cm^2 were used for the AZO sputtering. All AZO films sputtered with varied power densities and measured after annealing shows similar absorptance and comparable transmittance at film thickness of 125-145 nm as shown in Fig 4.13. The transmittance for the AZO sputtered with 1.3 W/cm^2 was slightly lower than the AZO sputtered with the power density of 2.0 and 2.7 W/cm^2. Electrical parameters of the films sputtered with different power densities are presented in Fig. 4.14. The μ, n, and ρ values are varied in small range with the increase of power density. AZO sputtered with 2.0 W/cm^2 power density shows the highest mobility compered to mobilities in the AZO films sputtered with 1.3 and 2.7 W/cm^2. In general, there is no obvious difference between these three power densities in terms of both optical and electrical properties. Considering the optimal power density for the AZO sputtering, power density of 2.0 W/cm^2 has been chosen for AZO in SHJ solar cells due to its proper optical property and higher mobility compared to the AZO sputtered with other power densities.

With the analysis on the results of the AZO sputtering pressure series and the power densities variation, the sputtering pressure of 0.1 Pa and power density of 2.0 W/cm^2 have been fixed for the following AZO development with varied substrate temperatures and doping concentrations.
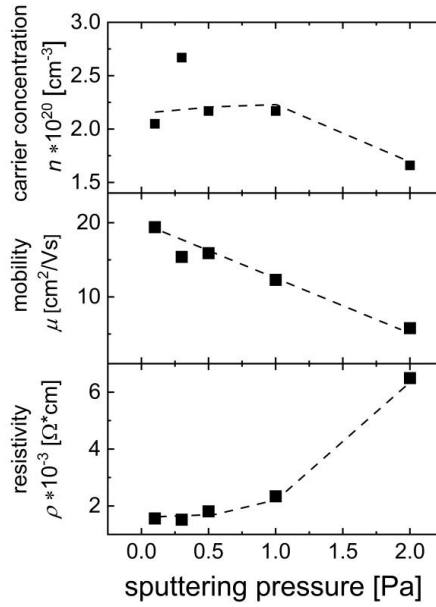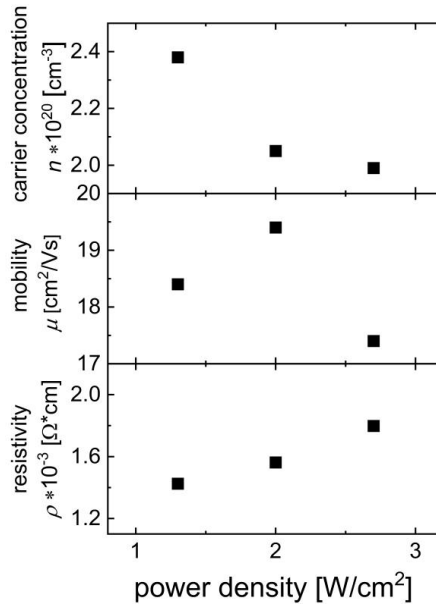

Fig. 4.14. Carrier concentration n, carrier mobility μ, and resistivity ρ from Hall measurement for AZO films after annealing as a function of sputtering power densities of 1.3, 2.0 and 2.7 W/cm^2, respectively.

4.2.2 AZO sputtered with varied heater temperatures, doping levels and gas precursor

To avoid the possible damage from the high substrate temperature during AZO sputtering to the Si layers underneath, the AZO films were sputtered at the substrate temperature lower than 200ºC at which the Si layers were deposited. However, in the AZO sputtering system, only the heater temperature instead of the substrate temperature can be controlled directly. To convert the heater temperature to the substrate temperature, the temperature sensitive stripes were pasted on the wafer surface at the opposite side of the plasma to detect the actual substrate temperature during sputtering. The heater temperatures of 170ºC and 250ºC are related to the substrate temperatures of 150ºC and 200ºC with 20-30 min pre-heating. In this section the AZO films were sputtered with the heater temperatures of 25ºC (RT), 120ºC, 150ºC, 170ºC, 210ºC, and 250ºC, respectively.

Transmittance and absorptance spectra for the AZO films sputtered at varied substrate temperatures with 1 wt.% target are presented in Fig. 4.15. Optical properties of AZO films in the states of as-deposited and annealed are plotted for comparison. All AZO films deposited in the heater temperature range of 25-250ºC show similar transmittance and absorptance, and the annealing, which is identical to be used in SHJ solar cell fabrication, has slightly influence on transmittance and absorptance. The average absorptance in the 300-1200 nm wavelength range is approximately 5 %, the value even can be as low as approximately 0.5 % in the wavelength range of 400-1200 nm. The transmittance spectra for all the AZO films are approximately above 80% from 400 nm. Increase in heater temperature slightly improved the transmittance and reduced the absorptance of the AZO film. Post-deposition annealing leads to slight increase in transmittance for the AZO films sputtered at the heater temperature below 170ºC. All in all, the heater

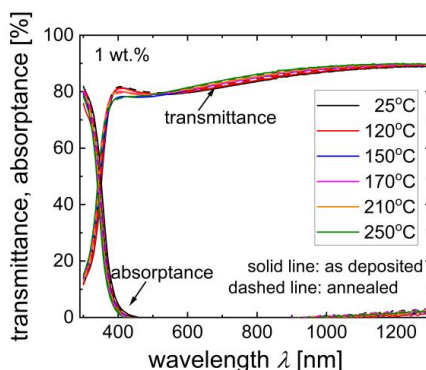Fig. 4.15. Transmittance and absorptance spectra of AZO films as a function of sputtering heater temperature from 25ºC to 250ºC with 1 wt.% AZO target. The T/R is measured without considering the absorptance and reflectance of the glass substrate.

temperature increasing during AZO sputtering and the post-deposition annealing has only slight influence on the AZO optical properties.

Electrical parameters of AZO films as a function of sputtering heater temperatures are presented in Fig. 4.16. With increase of the heater temperature mobility and carrier concentration firstly increase then decrease, while the resistivity decreases first then increases. For the heater temperature below 170°C, the post-deposition annealing reduces the resistivity and increases the carrier concentration. Especially for the AZO film sputtered at RT, both the mobility and resistivity show great improvement compared to the AZO film sputtered at other heater temperatures. However, for the AZO film deposited at the temperature above 170°C, the annealing has a negative effect on the film resistivity and mobility, and for the carrier concentration there is no clear trend. It can be seen as well that higher as-deposited mobilities have been achieved for the heater temperature above 170°C, however, it is reduced after annealing. Overall, both the increase of heater temperature and post-deposition annealing only results in a small variation for the electrical parameters of the AZO films.

In view of both optical and electrical properties of the AZO films sputtered at different heater temperatures, RT sputtered AZO has potential to be implemented in SHJ solar cells for low thermal budget and high throughput.
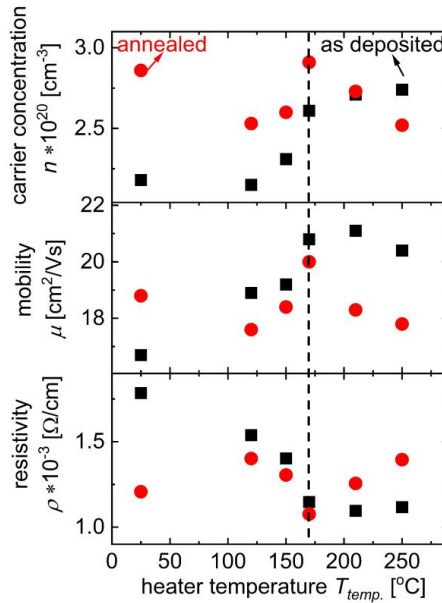

Fig. 4.16. Carrier concentration n, carrier mobility μ, and resistivity ρ from Hall measurement for AZO films as a function of sputtering heater temperatures from 25°C to 250°C with 1 wt.% AZO target.
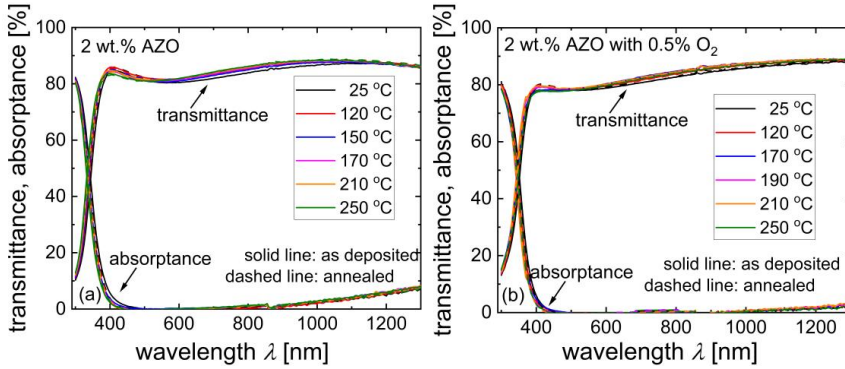
Fig. 4.17. Transmittance and absorptance spectra for AZO films as a function of sputtering heater temperature from 25°C to 250°C with (a) 2 wt.% AZO target and pure Argon precursor; (b) 2 wt.% AZO target and 0.5% O_2 in the Argon precursor.

In order to study the influence of target doping concentration on the properties of AZO films, 2 wt.% AZO target was used for sputtering with the precursors of pure argon and argon with 0.5% O_2. Fig. 4.17 presents the transmittance and absorptance spectra of AZO film sputtered with 2 wt.% target at varied heater temperatures in the states of as-deposited and annealed. Similar behaviors have been observed in the series of AZO sputtered with 1 wt.% AZO target. Both heater temperature and post-deposition annealing have merely slight influence on the transmittance and absorptance spectra. Compared to the AZO films deposited with pure Argon precursor, adding of oxygen contributes to the improvement in the absorptance of the long wavelength region resulting from the reduced free carrier absorption due to the reduced carrier concentration. The electrical properties of the AZO films further prove it as shown in Fig. 4.18. Fig. 4.18(a) presents the electrical parameters of AZO sputtered with 2 wt.% target and pure Argon precursor at varied heater temperatures. There is no obvious influence of the heater temperature on the resistivity, mobility and carrier concentration. The carrier density of the as-deposited AZO films increases with the increase of the heater temperature. The post-deposition annealing increases n with the heater temperature under 170°C and slightly decreases n for further increases of temperature. The carrier mobility for all the AZO in this series shows degradation after annealing. The resistivity increases after annealing except for the AZO film deposited at RT, where the resistivity is reduced. Fig. 4.18(b) presents the electrical parameters for the AZO sputtered with 0.5% O_2 adding to the precursor gas. For the heater temperature below 210°C, ρ decreases with the μ and carrier n increases with the increase of heater temperature. For the AZO film deposited at 250°C, the ρ

increases with the decreased *n* and *μ* compared to the AZO sputtered at lower heater temperatures. The post-deposition annealing has slight influence on the parameters at each temperature.

Fig. 4.18. Carrier concentration *n*, carrier mobility *μ*, and resistivity *ρ* from Hall measurement for AZO films as a function of sputtering heater temperature from 25°C to 250°C: (a) with 2 wt.% AZO target and pure Argon precursor; (b) with 2 wt.% AZO target and 0.5% O_2 in Argon precursor.

   To get an overview on the three different kinds of AZO, the optical properties of AZO after annealing are presented in Fig. 4.19. The heater temperature during AZO sputtering has slight influence on the optical properties of the AZO films sputtered with different target doping concentrations and gas precursors. Considering the reduce of the thermal budget, RT sputtered AZO is an optimum choice for the SHJ solar cells. To get an overview of the AZO performance at RT, the optical properties are presented again in Fig. 4.20. AZO films sputtered with 2 wt.% target shows a slightly higher absorption in the long wavelength region due to its higher carrier concentration compared to the AZO films sputtered with 1 wt.% target. Introduction of O_2 contributes to the reduction of the absorptance making the optical properties of AZO films sputtered with 2 wt.% target comparable to the AZO films sputtered with 1 wt.% target. Thus, in the view of optical properties of the AZO films, the RT sputtered AZO with 1 wt.% target or with 2 wt.% target and the adding of oxygen in the precursor are good options for SHJ solar cells.

Fig. 4.19. Transmittance and absorptance spectra for AZO films as a function of sputtering heater temperature from 25°C to 250°C with 1 wt.% target, 2 wt.% target, and 2 wt.% AZO target with 0.5% O_2 in the Argon precursor after annealing.
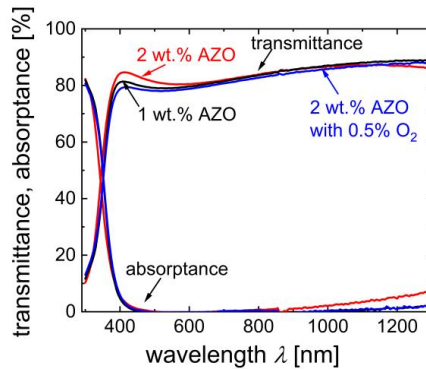
Fig. 4.20. Transmittance and absorptance spectra for the AZO films sputtered with 1 wt.% target, 2 wt.% target, and 2 wt.% AZO target with 0.5% O_2 in the Argon precursor at RT.
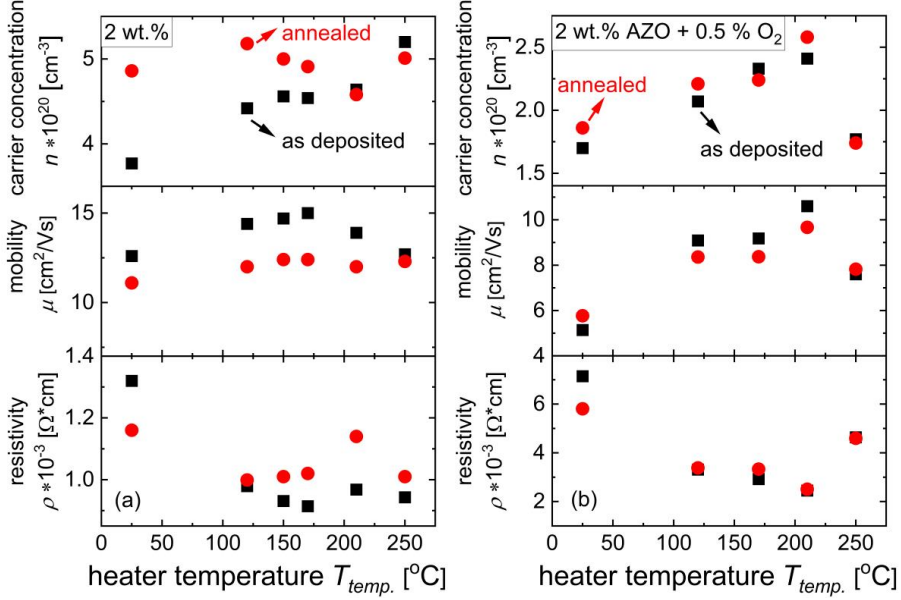
Fig. 4.21. Carrier concentration n, carrier mobility μ, and resistivity ρ from Hall measurement for AZO films as a function of sputtering heater temperature from 25°C to 250°C with 1 wt.% target, 2 wt.% target, and 2 wt.% AZO target with 0.5% O_2 in the Argon precursor after annealing

Electrical properties of AZO films with different target doping concentrations and precursors are presented in Fig. 4.21. AZO films sputtered with 2 wt.% target show approximately twice higher carrier concentration, twice lower carrier mobility and similar resistivity to AZO films sputtered with 1 wt.% target. Introduction of oxygen improves the absorptance as shown in Fig. 4.20 due to the decreased carrier concentration. However, it further decreases carrier mobility, thereby increases resistivity significantly. Therefore, considering the electrical properties of the AZO films and reduce of thermal budget, RT sputtered AZO with 1 wt.% target was chosen for the SHJ solar cell development.

A series of 130-nm-thick AZO films was prepared at varied heater temperatures with 2 wt.% target to study the thickness effect comparing to the 80-nm-thick AZO films. Optical properties of the AZO films are presented in Fig. 4.22 and the electrical properties are presented in Fig. 4.23. Same to the AZO series developed above, the sputtering temperature and post-deposition annealing have slight influence on the optical properties of AZO film with the thickness of 80 or 130 nm. Overall the 130-nm-thick AZO films show higher absorption, especially in the long
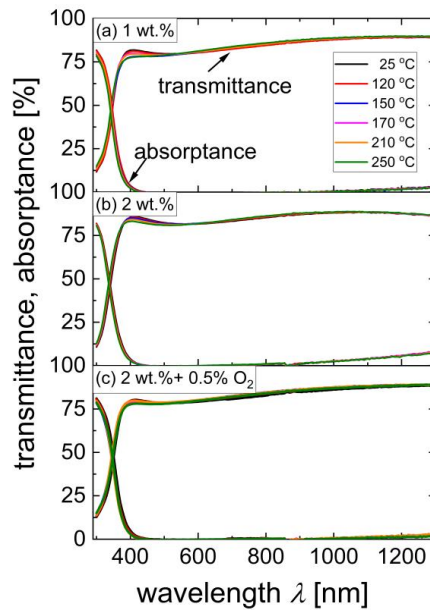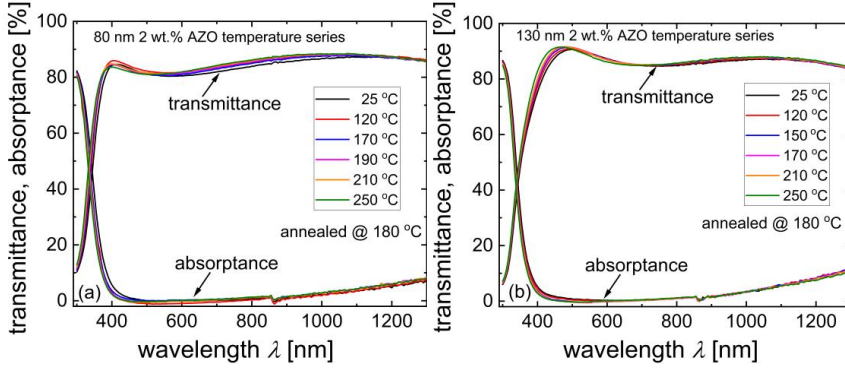
Fig. 4.22. Transmittance and absorptance spectra of AZO films as a function of sputtering heater temperature from 25℃ to 250℃ with the thickness of (a) 80 nm and (b) 130 nm.

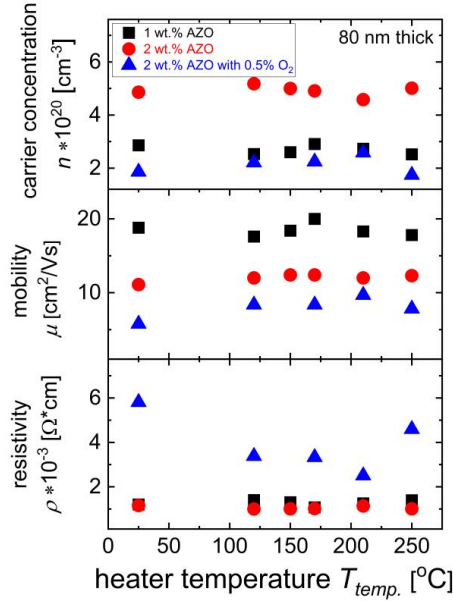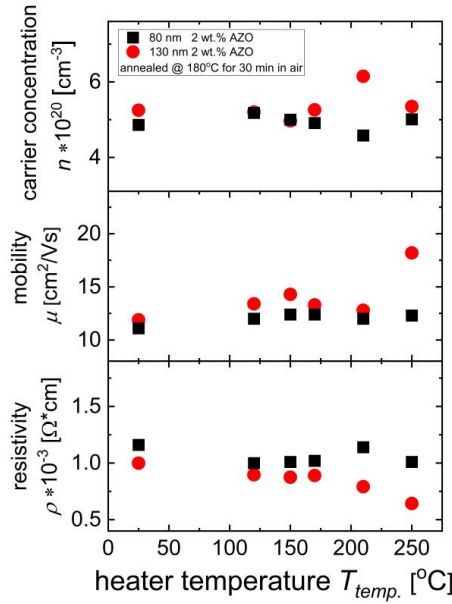Fig. 4.23. Carrier concentration n, carrier mobility μ, and resistivity ρ from Hall measurement of AZO films as a function of sputtering heater temperatures from 25°C to 250°C with the thickness of 80 nm and 130 nm.

wavelength region than the 80-nm-thick AZO film. In Fig. 4.23, 130-nm-thick AZO layers show slightly higher carrier concentration and mobility compared to the 80-nm-thick AZO film. Slight

lower resistivity is observed as well for the thicker layer especially for the films sputtered with high heater temperatures. Application of thick AZO in SHJ solar cells needs taking the parasitic absorption and anti-reflection function into consideration as well.

4.3 Short summary

In this chapter, doped nc-Si layers and AZO films for SHJ solar cells have been developed and their properties have been characterized. The Si layers were deposited on glass substrates to obtain the deposition rate and on the intrinsic a-Si layer coated glass substrates mimicking the deposition conditions in SHJ solar cells. The deposition power, silane and phosphorus flow rate ratios (r_{SiH4}, r_{PH3}), and thickness for n-type nc-Si layer were varied. The results show that the parameter set of substrate temperature of 200ºC, power of 200 W, r_{SiH4} of 0.01, r_{PH3} of 1, pressure of 2.5 mbar, and thickness of 20 nm is most appropriate for SHJ solar cells. The TMB flow rate ratio r_{TMB}, deposition pressure and doping gas for p-type nc-Si layer were varied to find proper deposition parameters. Based on the current results, the parameter set of substrate temperature of 200ºC, power of 200 W, r_{SiH4} of 0.01, r_{TMB} of 0.5, pressure of 2.5 mbar, and thickness of 20 nm has been chosen as most appropriate for further SHJ solar cell development.

For AZO film development, the gas pressure and power density for sputtering were firstly set down. Then the AZO layers have been sputtered with varied temperatures, target doping concentration, gas precursor, and thickness. Optical and electrical properties of AZO films have been characterized before and after the annealing mimicking post metallization annealing. Results show that heater temperature has slight influence on both optical and electrical properties of the AZO films sputtered with varied doping target concentrations and precursors gases. Thus, room temperature sputtering process is believed to be the optimal for solar cell fabrication to save the thermal budget. For the RT sputtering process, the AZO films sputtered with 2 wt.% target show slightly higher absorption in the long wavelength region due to its higher carrier concentration compared to the AZO films sputtered with 1 wt.% target. Introduction of O_2 to sputtering precursor gas results in reduction of the absorptance making optical properties of AZO films sputtered with 2 wt.% target comparable to the properties of AZO films sputtered with 1 wt.% target. As for the electrical properties, AZO films sputtered with 2 wt.% target show approximately two times higher carrier concentration, half of the mobility and similar resistivity to AZO films sputtered with 1 wt.% target. Introducing oxygen in the precursor gas leads to further decrease of mobility and increase of resistivity significantly compared to the AZO sputtered with 2 wt.% target and pure argon. In conclusion, considering both the optical and electrical properties of the AZO films, the RT sputtered AZO with 1 wt.% target is expected to be optimal TCO for implementation into SHJ solar cells.

Chapter 5 AZO and doped nc-Si applied in SHJ solar cells

This chapter deals with application of different doped Si layers and Al-doped zinc oxide layers in silicon heterojunction solar cells. The SHJ solar cells were fabricated in rear emitter configuration on n-type Czochralski wafers. The n-type Si layer was used at the front as a window layer with front surface field function and the p-n junction was formed at the rear side of the device. The solar cells were either fabricated with the aperture size of 19 mm ×19 mm or full size on M2 wafers. Performance of the cells with different combinations of Si and AZO layers is summarized. Content of this chapter is divided into three sections. Section 5.1 summarizes the optical and electrical properties of n-/p-type amorphous/nanocrystalline Si layers applied in SHJ solar cells. Section 5.2 describes the application of various AZO films in SHJ solar cells in combination with different doped Si layers. The AZO layers in the cells have been prepared with different doping concentrations, sputtering substrate temperatures, and sputtering gas precursors. Contacts properties of AZO/doped Si layer stacks have been tested in SHJ solar cells as well. In the last part of this section, results of solar cell performance are summarized and potential of applying RT sputtered AZO in SHJ solar cells is discussed. Section 5.3 summarizes further optimization of the cells and describes the direction for future development of SHJ solar cells with AZO.

5.1 Optical and electrical properties of Si layers applied in SHJ solar cells

Four different doped Si layers of n-type a-Si, n-type nc-Si, p-type a-Si, and p-type nc-Si have been studied for the fabrication of SHJ solar cells. Absorption coefficient dependency on photon energy measured with PDS is presented in Fig. 5.1. Conductivity of Si layers is summarized in Table 5.1. The spectra in Fig. 5.1 are typical for every presented material class. The n-type nc-Si shows lower absorption coefficient in energy range of 2.0-3.3 eV compared to the n-type a-Si which is beneficial for the application at the front of cell to reduce parasitic absorption of high energy photons. Qualitatively same picture is observed when p-type nc-Si and p-type a-Si are compared, however, the difference in this case is smaller in high energy part of the spectra. This

difference in absorption properties between p-type a-Si and p-type nc-Si has minor influence on the performance of SHJ solar cells since these p-type layers were used at the rear side of the solar cell. Electrical properties of the contacts between AZO and doped Si layers are of critical importance for proper operation function of SHJ solar cells and therefore are in focus of this study.
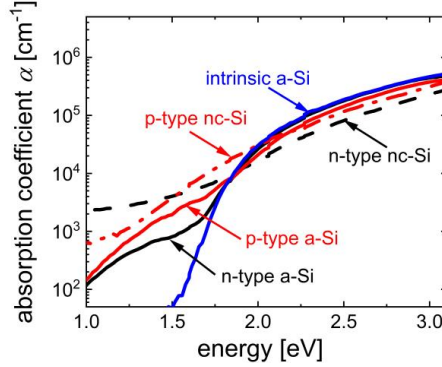
Fig. 5.1. Absorption coefficient measured with photothermal deflection spectroscopy of four kinds of doped Si layers: n-type a-Si, n-type nc-Si, p-type a-Si, and p-type nc-Si applied in SHJ solar cells. The absorption coefficient of the passivation layer of intrinsic a-Si is presented as well.

Four types of doped Si layers were prepared on glass substrates in order to characterize conductivity. It is known that the properties of thin-film Si layers are influenced by substrate up to the thickness of at least 50 nm [91, 92]. To mimic the conditions during SHJ solar cell fabrication, an 8.5-nm-thick intrinsic a-Si layer was deposited on glass prior to the doped Si layers. Due to the low dark conductivity σ_{dark} of 10^{-12}-10^{-9} S/cm for the intrinsic a-Si, contribution of these layers to the measured conductivity can be neglected. Note that the conductivities of Si layers prepared on Corning glass substrate were measured at room temperature in the dark and air with two thermally evaporated coplanar silver contacts which results in lateral conductivity. Conductivity in vertical direction cannot be measured with coplanar contacts and possible anisotropy is not detected. However, the lateral conductivity is used as an indication of qualitative variations of transversal conductivity in this work.

Table. 5.1. Thicknesses and conductivities of n-type a-Si, n-type nc-Si, p-type a-Si, and p-type nc-Si layers prepared on intrinsic a-Si covered glass substrate.

	n-type a-Si	n-type nc-Si	p-type a-Si	p-type nc-Si
thickness [nm]	192	35	118	35
conductivity [S/cm]	2.1×10^{-2}	8.3×10^{-1}	4.4×10^{-5}	1.0×10^{-2}

Table 5.1 contains layer thickness and lateral conductivity for n-type a-Si, n-type nc-Si, p-type a-Si, and p-type nc-Si layers with intrinsic a-Si layer underneath prepared for this study. Doped nc-Si layers show conductivities in magnitude of 10^{-1} S/cm for n-type and 10^{-2} S/cm for the p-type with the thickness of 35 nm for both layers. Doped a-Si layers show conductivities in magnitude of 10^{-2} S/cm for n-type a-Si and 10^{-5} S/cm for p-type a-Si, respectively, at the thickness above 100 nm. All conductivity values are typical for high quality doped layers which is a prerequisite for proper cell operation [93].

5.2 Implementation of AZO in SHJ solar cells

5.2.1 AZO sputtered at RT with 1 wt.% target in SHJ solar cells

Considering mass production requirements, AZO films prepared with common magnetron sputtering technique at room temperature were chosen to be applied in SHJ solar cells. AZO sputtered at room temperature has the advantage of low thermal budget and potential for high throughput. In this section, RT sputtered AZO was applied in SHJ solar cells in combination with four kinds of doped Si layers as shown in section 3.1.5. There were four 19 mm × 19 mm size cells
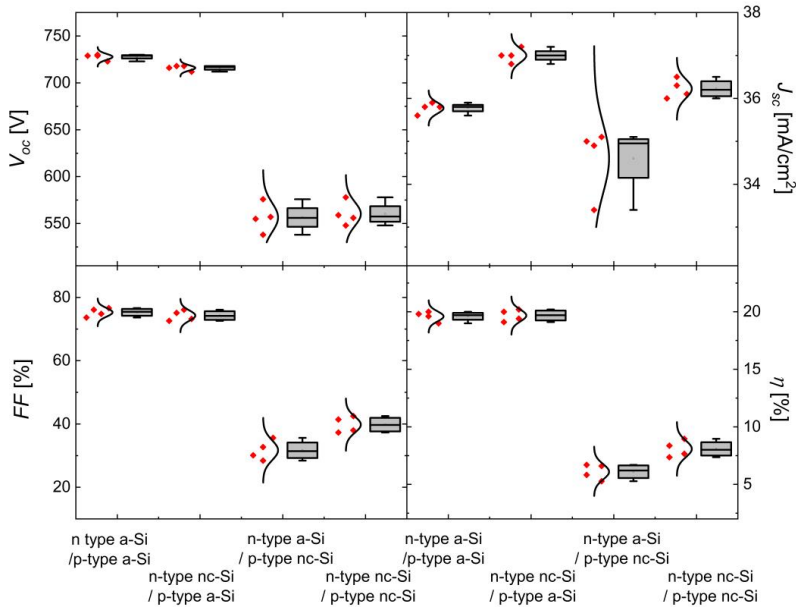

Fig. 5.2. Photovoltaic parameters of SHJ solar cells with the following four combinations of doped Si layers on the front and rear: (1) n-type a-Si / p-type a-Si, (2) n-type nc-Si / p-type a-Si, (3) n-type a-Si / p-type nc-Si, and (4) n-type nc-Si / p-type nc-Si. Same RT sputtered AZO with 1 wt.% target was used as TCO in all presented cells.

fabricated on the 78 mm × 78 mm size wafers to ensure statistical significance of the results. Cell photovoltaic parameters are presented in Fig. 5.2, J-V curves are shown in Fig. 5.3, and the internal quantum efficiency and 1-reflection spectra are presented in Fig. 5.4. The internal quantum efficiency was calculated as *IQE=EQE/(1-reflection)*.
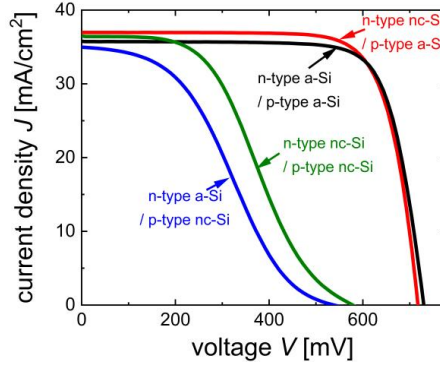

Fig. 5.3. Light current density-voltage curves of SHJ solar cells with the following four combinations of doped Si layers on the front and rear: (1) n-type a-Si / p-a-Si, (2) n-type nc-Si / p-type a-Si, (3) n-type a-Si / p-type nc-Si, and (4) n-type nc-Si / p-type nc-Si. Same RT sputtered AZO with 1 wt.% target was used as TCO in all presented cells.

It can be seen in Fig. 5.2 that the cells with p-type a-Si layer show normal cell operation with the photovoltaic parameters of V_{oc} above 700 mV, *FF* above 70 %, and η approximate 20 %. However, the SHJ solar cells with p-type nc-Si layer show poor photovoltaic parameters performance with V_{oc} approximate 550 mV, *FF* below 40 % and η below 10 % which is significantly lower compared to the solar cells with p-type a-Si layer. In terms of J_{sc}, the cells with n-type nc-Si layer show higher values due to the reduced parasitic absorption as compared to the cells with n-type a-Si layer. This is consistent with the observation in the light J-V curves as shown in Fig. 5.3. Meanwhile, it is also observed that there is strong s-shape in the J-V curves from the cells with p-type nc-Si layer which will be addressed further in chapter 7. As for the *IQE* response and 1-reflection spectra shown in Fig. 5.4, the active area $J_{EQE,\ active\ area}$ calculated from the active area *EQE* spectra are indicated in mA/cm^2. The cells with n-type nc-Si layer shows that the $J_{EQE,\ active\ area}$ values are above 38 mA/cm^2, while the cells with n-type a-Si layer shows the $J_{EQE,\ active\ area}$ values are approximate 37 mA/cm^2. The increase in $J_{EQE,\ active\ area}$ of the cells with n-type nc-Si layer is related to its higher *QE* response in the wavelength range of 350-700 nm which is consistent with the variations of J_{sc} values as well as with the light J-V curves as shown Fig. 5.3. However, unlike the contribution from n-type nc-Si layer, there is no difference in the *IQE* response in the wavelength region above 1000 nm for cells with both p-type a-Si and nc-Si layers.

After the successful application of n-type nc-Si as window layer in SHJ solar cells, several series with variations in Si layers and TCO have been prepared to explore ways to improve SHJ solar
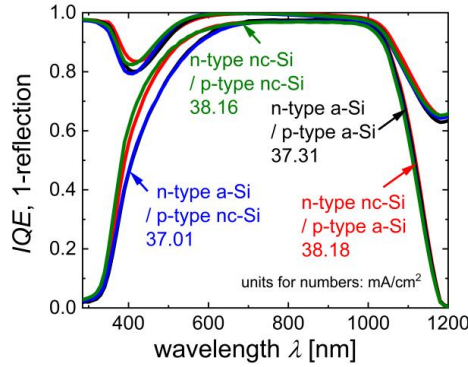
Fig. 5.4. Internal quantum efficiency response and 1-reflection spectra of SHJ solar cells with the following four combinations of doped Si layers on the front and rear: (1) n-type a-Si / p-type a-Si, (2) n-type nc-Si / p-type a-Si, (3) n-type a-Si / p-type nc-Si, and (4) n-type nc-Si / p-type nc-Si. Same RT sputtered AZO with 1 wt.% target was used as TCO in all presented cells.

cells performance. Generally, there are three requirements for the proper window layer applied in SHJ solar cells: (1) low parasitic absorption related to layer absorption coefficient and layer thickness, (2) good passivation combined with the intrinsic amorphous Si layer underneath, and (3) proper contact with the following TCO layers. Since the passivation quality was monitored during cell fabrication process, it has been found that high lifetime is achieved after the Si layer deposition, thus, the focus in this study is on the variation of n-type nc-Si layer thickness, TCO, and the contacts between doped Si layer and TCO.

For the n-type nc-Si layer thickness, 10- and 20-nm-thick n-type nc-Si layers were used in SHJ solar cells. The cells were measured prior to and after annealing, which is typically applied to the cells after metallization. The annealing was performed to form ohmic contact between TCO and Ag. Cell photovoltaic parameters of these cells are presented in Fig. 5.5. The SHJ solar cells with 20-nm-thick n-type nc-Si layer show higher V_{oc}, J_{sc}, and η compared to the cells with 10-nm-thick n-type nc-Si layer. Both of these two cells show comparable FF. For the cells with 10-nm-thick n-type nc-Si layer, annealing reduces V_{oc} and J_{sc}, while improves FF and slightly affects η. For the cells with 20-nm-thick n-type nc-Si layer, the annealing has a positive influence on the cell performance and improves V_{oc}, J_{sc}, FF and η. Cells with the 20-nm-thick n-type nc-Si, instead of the 10-nm-thick layer, show the potential to achieve an efficiency above 20 %.

Fig. 5.6 shows the light J-V curves for the cells with 10- and 20-nm-thick n-type nc-Si layers. The cell with 20-nm-thick n-type nc-Si shows higher short circuit current compared to the cell with 10-nm-thick n-type nc-Si layer which is observed from QE response as well in Fig. 5.7. The cell with 20-nm-thick n-type nc-Si shows a higher QE response in the whole wavelength region compared to the cell with 10-nm-thick n-type nc-Si layer.

Fig. 5.5. Photovoltaic parameters of the SHJ solar cells with 10 or 20 nm-thick n-type nc-Si, and p-type a-Si layers were used to form the junction at rear side of the cells.
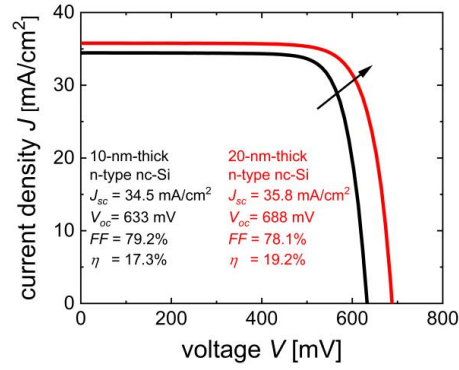
Fig. 5.6. Light current density-voltage curves of the SHJ solar cells with 10 nm- or 20 nm-thick n-type nc-Si, and p-type a-Si layers were used to form the junction at rear side of the cells. The photovoltaic parameters are indicated as inset.
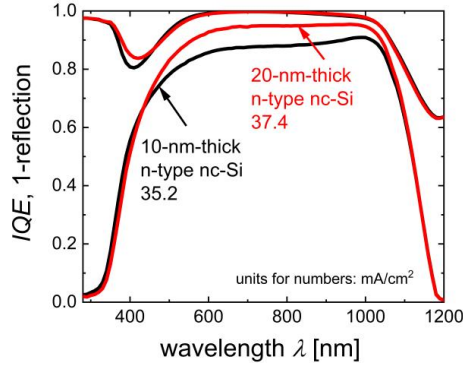
Fig. 5.7. Internal quantum efficiency and 1-reflection spectra of the SHJ solar cells with 10- or 20 nm-thick n-type nc-Si layer, and p-type a-Si layers were used to form the junction at rear side of the cells.

The contact resistances between n-type nc-Si layer and AZO were characterized with TLM measurement. Specific contact resistance ρ_c values which is a product of contact resistance and contact area were measured under dark and light, or before and after annealing of SHJ solar cells with 10- and 20-nm-thick n-type nc-Si layers. The results are presented in Fig. 5.8. Cells with 20-nm-thick n-type nc-Si layer show one order of magnitude lower resistance compared to the cells with 10-nm-thick n-type nc-Si layer. Both annealing and light condition reduces the contact resistance between AZO and 10-nm-thick n-type nc-Si layer. However, they have slight influence on the contact resistance between AZO and 20-nm-thick n-type nc-Si layer.
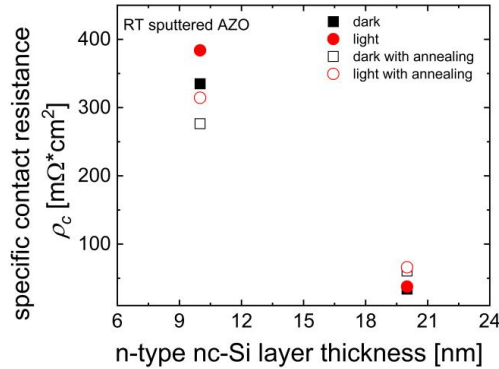
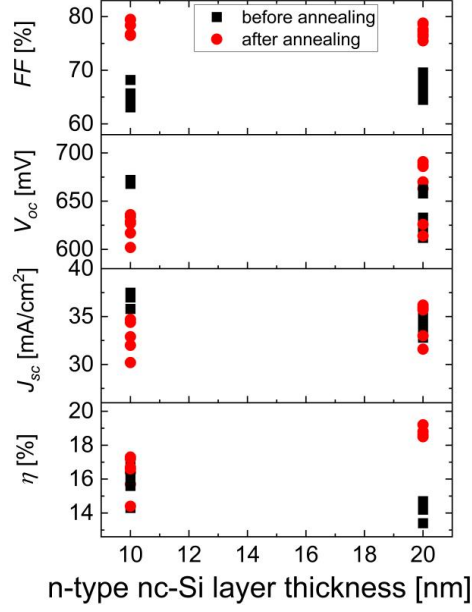Fig. 5.8. Specific contact resistance under dark and light, before and after annealing of the SHJ solar cells with 10- or 20-nm-thick n-type nc-Si layer, and p-type a-Si layers were used to form the junction at rear side of the cells.

Besides the RT sputtered AZO, reference ITO was introduced in SHJ solar cells as well to compare the cell performance to the cells with AZO. In these cells, 20-nm-thick n-type nc-Si layer was used as window layer. The TCO layer combinations of (1) ITO at front and rear side (ITO (f+r)), (2) ITO at front side and AZO at rear side (AZO(f) + ITO(r)), and (3) AZO at front and rear side (AZO (f+r)) were applied in SHJ solar cells. Cell photovoltaic parameters for the three kinds of solar cells with various TCO layer combinations are shown in Fig. 5.9. These three kinds of cells show comparable results. The cell with AZO(f) + ITO (r) presents slightly higher V_{oc}, FF and η among the three kinds of cells. The cell with both AZO contacts shows the highest J_{sc} among these three kinds of solar cells due to the lower absorption of AZO in the short and long wavelength region. The *IQE* spectra for these cells are shown in Fig. 5.10. Cells with AZO at both sides show higher *QE* response in the short and long wavelength region compared to the ITO counterparts. Cell with AZO (f+r) shows the active area $J_{EQE, active\ area}$ of 38.2 mA/cm^2 which is higher than the $J_{EQE, active\ area}$ values of 37.4 and 37.6 mA/cm^2 for the cells with ITO (f+r) and AZO (f) + ITO (r). From the cells results it can be concluded that RT sputtered AZO is a good substitute for the ITO as TCO contact in SHJ solar cells, even though the AZO material has its intrinsic limitation of the low carrier mobility. The following sections are focused on the application of various AZO films in the SHJ solar cells and the related cell performance.
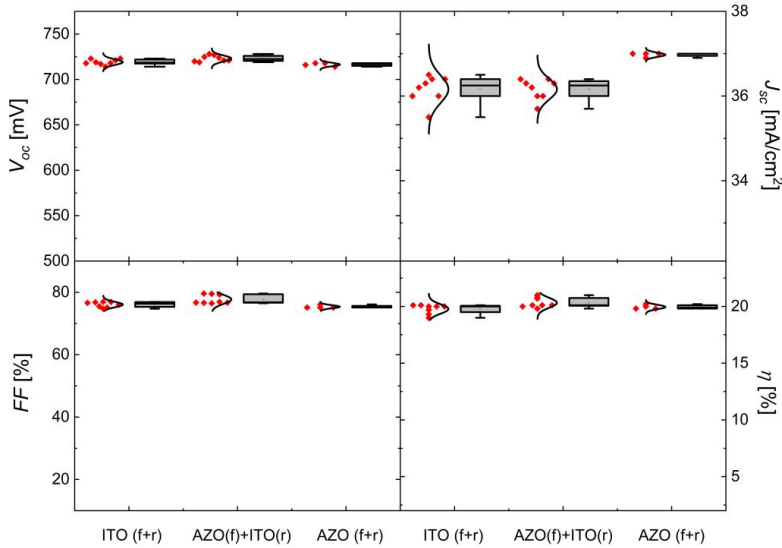
Fig. 5.9. Photovoltaic parameters of the SHJ solar cells with the TCO layer combinations: (1) ITO at front and rear sides ITO (f+r); (2) AZO at front side and ITO at rear side AZO (f)+ITO (r); and (3) AZO at front and rear sides AZO (f+r), respectively.
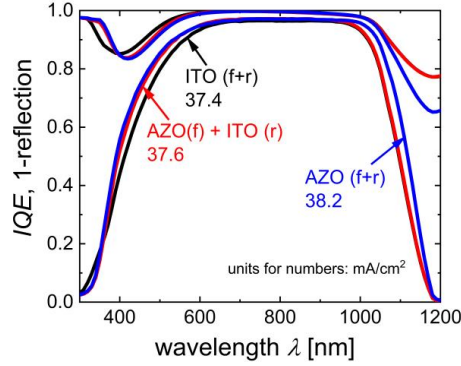
Fig. 5.10. Internal quantum efficiency and 1-reflection spectra of the SHJ solar cells with the TCO layer combinations: (1) ITO at front and rear sides ITO (f+r); (2) AZO at front side and ITO at rear side AZO (f)+ITO (r); and (3) AZO at front and rear sides AZO (f+r), respectively.

   In view of critical importance of passivation quality for the high excess carrier lifetime, QSSPC measurements have been carried out after each step in cell fabrication process: after the Si layer stack deposition, after TCO sputtering on the front and rear sides of the device, and after annealing. The implied open circuit voltage (iV_{oc}) acquired from lifetime measurement and the cell V_{oc} from the illuminated J-V measurement are summarized in Fig. 5.11. Reference ITO sputtering has no negative influence on the effective carrier lifetime and therefore iV_{oc}. However, the sputtering of AZO leads to significant decrease of iV_{oc} from 730 mV to 690 mV, which is, however, eliminated by the annealing performed after the metallization. There is a difference between the iV_{oc} values
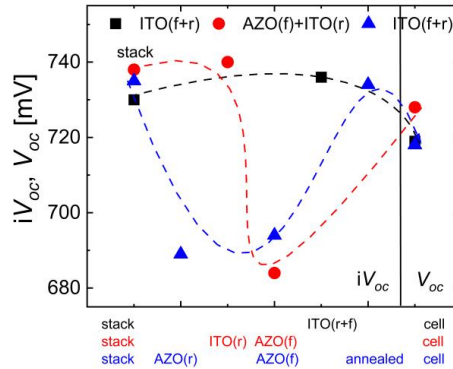
Fig. 5.11. Implied open circuit voltage (iV_{oc}) values acquired from QSSPC measurements during the cell fabrication process and the V_{oc} values acquired from the J-V measurements of the cells with the TCO layer combinations: (1) ITO at front and rear sides ITO (f+r); (2) AZO at front side and ITO at rear side AZO (f)+ITO (r); and (3) AZO at front and rear sides AZO (f+r), respectively.

after annealing and the V_{oc} measured in ready cell. The difference is to large extent attributed to the non-ideal carrier selective function of the selective contact stacks [94, 95].

In conclusion, performance of the cells with AZO is comparable to the cells with ITO after the typical post-metallization annealing. Thus, the investigation on the performance of solar cells with AZO at the front and rear side of the device is focused on in this study.

5.2.2 AZO sputtered at elevated temperatures with 1 wt.% target in SHJ solar cells

It is known from thin-film solar cell development that high temperature sputtering processes result in AZO with improved optical or electrical properties related to improved microstructure of the material [96]. In this section, the substrate temperatures of 150°C and 200°C well below the Si layer deposition temperature have been used for the AZO sputtering during cell fabrication process. The AZO layers sputtered at 150°C or 200°C were applied in the cells with four kinds of combinations of Si layers, which is consistent with the application of room temperature sputtered AZO in solar cells as discussed in section 5.2.1. Dependencies of photovoltaic parameters, J-V curves and *IQE* and 1-reflection spectra on the Si layer combinations show similar trends for the
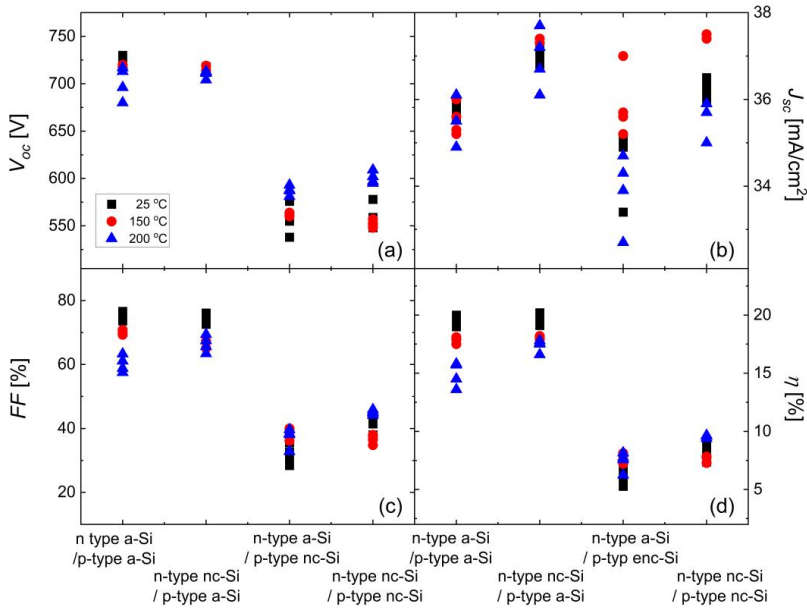
Fig. 5.12. Photovoltaic parameters of the SHJ solar cells with RT, 150°C, and 200°C sputtered 1 wt.% AZO and four combinations of silicon doped layers on the front and rear side: (1) n-type a-Si / p-type a-Si, (2) n-type nc-Si / p-type a-Si, (3) n-type a-Si / p-type nc-Si, and (4) n-type nc-Si / p-type nc-Si.
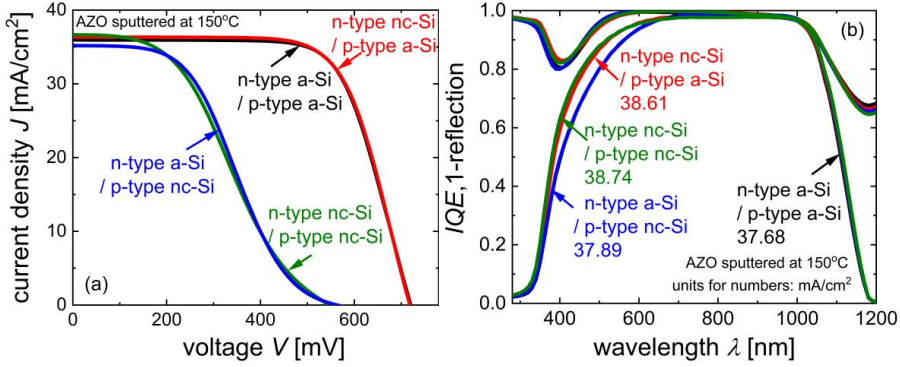
Fig. 5.13. (a) Light current density-voltage curves and (b) *IQE* and 1-reflection spectra of SHJ solar cells with AZO sputtered at 150°C and four combinations of doped Si layers on the front and rear sides: (1) n-type a-Si / p-type a-Si, (2) n-type nc-Si / p-type a-Si, (3) n-type a-Si / p-type nc-Si, and (4) n-type nc-Si / p-type nc-Si.

cells with AZO films sputtered at RT, 150°C and 200°C, respectively, as shown in Fig. 5.3, Fig. 5.4, Fig. 5.12, Fig. 5.13 and Fig. 5.14. Cells with n-type nc-Si layer show higher J_{sc} and *IQE* response in short wavelength region compared to cells with n-type a-Si layer. Cells with the p-type nc-Si layer show the extremely low V_{oc}, *FF* and η which is consistent with the s-shaped J-V curves shown in the Fig. 5.13(a) and Fig. 5.14(a).

There is no obvious improvement of the solar cell performance with AZO layers sputtered at 150°C and 200°C compered to cells with AZO sputtered at room temperature. Even though, higher
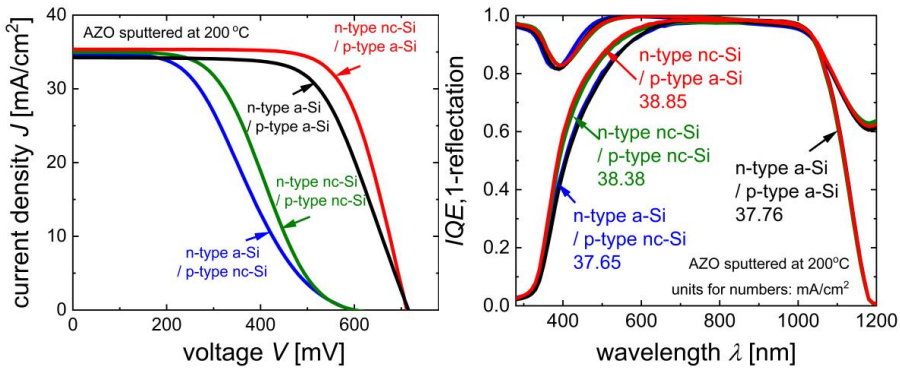
Fig. 5.14. (a) Light current density-voltage curves and (b) *IQE* and 1-reflection spectra of SHJ solar cells with AZO sputtered at 200°C and four combinations of doped Si layers on the front and rear sides: (1) n-type a-Si / p-type a-Si, (2) n-type nc-Si / p-type a-Si, (3) n-type a-Si / p-type nc-Si, and (4) n-type nc-Si / p-type nc-Si.

AZO sputtering temperature even results in the decrease of V_{oc}, J_{sc}, FF, and η for the cells with n-type nc-Si layer.

The cells with RT sputtered AZO shows higher V_{oc}, FF, and η compared to the cells with 150°C and 200°C sputtered AZO layers. Dependence of photovoltaic parameters of SHJ solar cells on AZO sputtering temperature indicates the potential of room temperature AZO sputtering process for SHJ solar cell mass production.

5.2.3 AZO sputtered with varied doping levels and precursors in SHJ solar cells

In order to explore the effect of AZO doping on the electrical contacts between doped Si layers and AZO, higher doping AZO films sputtered with 2 wt.% target were applied in SHJ solar cells. AZO layer sputtered with adding of oxygen to AZO sputtering chamber was tested in SHJ solar cells as well as an option to reduce the parasitic absorption. Considering the issue of s-shaped J-V curves observed in the cells with p-type nc-Si layers, the p-type a-Si layers were used to form the junction for the SHJ solar cells with the AZO variation in terms of doping concentrations and sputtering precursors. The n-type a-Si or n-type nc-Si layers were used at the front side of the cells.

Fig. 5.15 presents performance of the solar cells with 2 wt.% AZO sputtered at RT, 150°C and 200°C. For the cells with n-type a-Si layer, the increase of AZO sputtering substrate temperature results in the decrease of V_{oc}, FF, and η. For the cells with n-type nc-Si layer, the increase of AZO sputtering substrate temperature slightly increases V_{oc} and J_{sc} and slightly decreases FF and η. The cells with n-type nc-Si layer show higher J_{sc} compared to the cells with n-type a-Si layer confirmed by *IQE* response as presented in Fig. 5.16. By comparing the performances of the cells with the AZO films sputtered at RT, 150°C and 200°C, the cells with RT sputtered 2 wt.% AZO show the best performance.

As shown in the chapter 4, adding oxygen in the AZO sputtering precursor gas mixture can reduce the absorption in the long wavelength region while reduce the mobility and increase the resistivity as well. To investigate the influence of this trade-off between optical and electrical properties, 2 wt.% AZO films with 0.5% O_2 in the sputtering precursor gas mixture have been used in the SHJ solar cells. For this series of cells, the metallization has been optimized. A busbar surrounding design as shown in the Fig. 3.4(b) has been prepared with screen printing to reduce the metal fraction on the front of the device, thus improving the J_{sc} compared to the cells with the evaporated silver electrodes. Cells parameters with the 2 wt.% AZO sputtered with oxygen are presented in Fig. 5.17. With the increase of the substrate temperature during AZO sputtering, V_{oc}, FF, and η values decrease. The cells with n-type a-Si layer is more sensitive to the AZO sputtering temperature than the cells with n-type nc-Si layer. For both cells with n-type a-Si or n-type nc-Si layers, cells with AZO sputtered at 150°C show lower J_{sc} compared to the cells with AZO sputtered at RT and 200°C. The cells with AZO sputtered at 200°C show a slightly increased J_{sc} due to the optimized metallization.
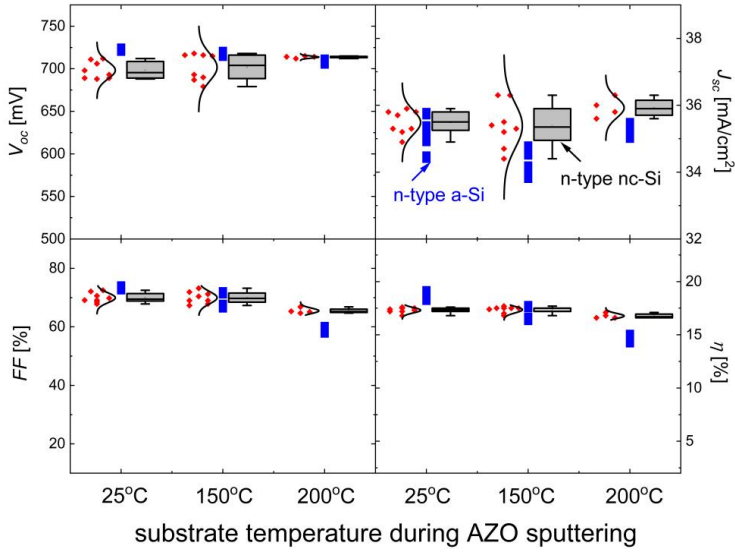
Fig. 5.15. Photovoltaic parameters of the SHJ solar cells with 2 wt.% AZO sputtered at 25ºC, 150ºC, and 200ºC, respectively. The n-type a-Si or nc-Si layers were used as window layer and p-type a-Si layer was used to form junction. The blue points are the parameters for the cells with n-type a-Si layer. The red diamond, distribution line and box are the parameters for the cells with n-type nc-Si layer.
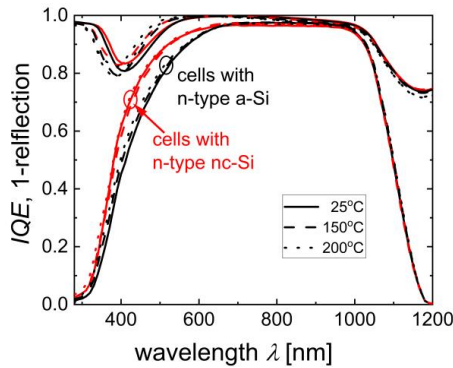
Fig. 5.16. Internal quantum efficiency and 1-reflection spectra of the SHJ solar cells with 2 wt.% AZO sputtered at 25ºC, 150ºC, and 200ºC, respectively. The n-type a-Si or nc-Si layers were used as window layer and p-type a-Si layer was used to form junction.
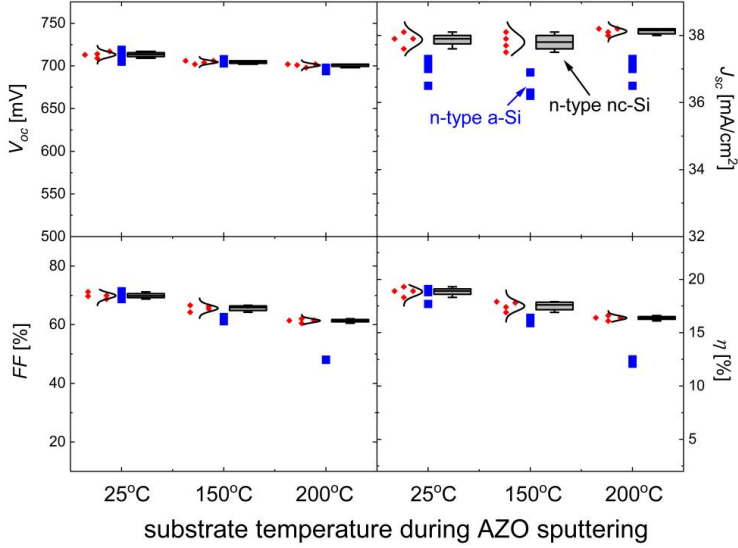
Fig. 5.17. Photovoltaic parameters of the SHJ solar cells with AZO sputtered at 25°C, 150°C, and 200°C with 2 wt.% AZO and 0.5% O_2 in the sputtering precursor gas mixture. The n-type a-Si or nc-Si layers were used as window layer, and p-type a-Si layer was used to form junction. The blue points are the parameters for the cells with n-type a-Si layer. The red diamond, distribution line and box are the parameters for the cells with n-type nc-Si layer.

Fig. 5.18 shows the I-V curves for the cells with the AZO sputtered at 25°C, 150°C and 200°C, respectively. For the cells with n-type a-Si or n-type nc-Si layers, increasing AZO sputtering
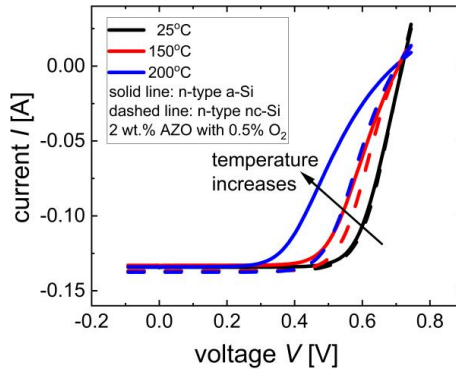
Fig. 5.18. Current-voltage curves of the SHJ solar cells with 25°C, 150°C, and 200°C sputtered 2 wt.% AZO with 0.5% O_2 in the sputtering gas precursor. The n-type a-Si or nc-Si layers were used as window layer and p-type a-Si layer was used to form junction.

temperature leads to the decrease of *FF*. In this case, the AZO film sputtered with 2 wt.% target is not a proper TCO material for SHJ solar cells.

Fig. 5.19 shows *IQE* and 1-reflection spectra for the cells with AZO sputtered at varied temperatures together with calculated values of $J_{EQE, \, active \, area}$. The cells with n-type nc-Si layer show higher *IQE* response in the short wavelength region compared to the cells with n-type a-Si layers. The higher AZO sputtering temperature slightly increases the cell reflection and decreases *IQE* response in short wavelength region.
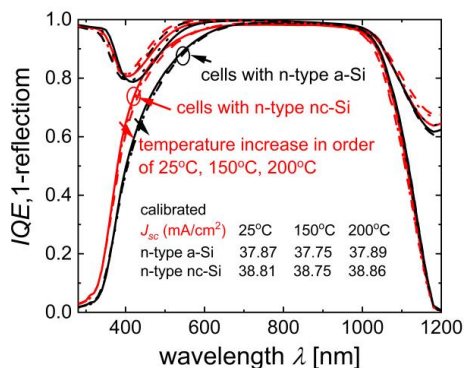
Fig. 5.19. Internal quantum efficiency and 1-reflection spectra of the SHJ solar cells with 25°C, 150°C, and 200°C sputtered 2 wt.% AZO with 0.5% O_2 in the sputtering gas precursor. The n-type a-Si or nc-Si layers were used as window layer and p-type a-Si layer was used to form junction.

In conclusion, increase of substrate temperature has a negative influence on the performance for the cells with AZO sputtered with 2 wt.% target with or without oxygen in the precursor gas mixture. RT sputtering process is still the most optimal for solar cells in the AZO temperature series sputtered with 2 wt.% target and oxygen. Finally, for the AZO films sputtered with 1 wt.% target, 2 wt.% target and 2 wt.% target and oxygen, room temperature is the optimal substrate temperature during AZO sputtering process for SHJ solar cells.

5.2.4 Contact resistance at the interface between AZO and Si layer

The contact at the interface is critical for cell performance. In this section the specific contact resistances at the interfaces of AZO/Ag and doped Si/AZO are acquired by transfer length method measurement. The TLM structure are prepared on the cell stack as shown in Fig 3.4(a) and the TLM method is shown in section 3.2.2.1. In these cells, all the AZO films are deposited at room temperature. The contact resistances within the front stack are acquired from the prepared solar cells. However, the contact resistances within the rear stack of cells can only be acquired by preparing the p-type doped layer on p-type Si wafer to get rid of the junction influence on the TLM

measurement. Thus, the contact resistance measurements are divided into two sections for descriptions of front stack and rear stack of the device.

As for the front stack of cell, the contact resistance at the interface between AZO and Ag are presented in Fig. 5.20. The contact resistances below 3.2 mΩ*cm^2 have been acquired for all the cells with 1 wt.% and 2 wt.% AZO films, which indicates the proper contact between AZO and Ag.
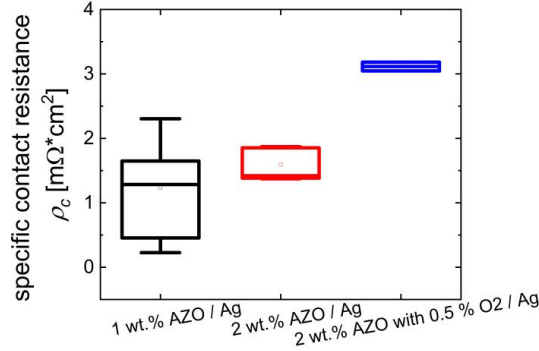
Fig. 5.20. Specific contact resistances at the interface between AZO and silver on n-type nc-Si growth surface for AZO sputtered with 1 wt.% target, 2 wt.% target, and 2 wt.% with oxygen in 19 mm × 19 mm SHJ solar cells.

The contact resistances for the front layer stack of AZO and n-type a-Si are summarized in Fig. 5.21(a) and for the front layer stack of AZO and n-type nc-Si are summarized in Fig. 5.21(b). The n-type Si layers show ohmic contact to the AZO layers with different AZO doping concentrations and precursors gas mixtures. There is an exception for the front layer stack of 2 wt.% AZO with
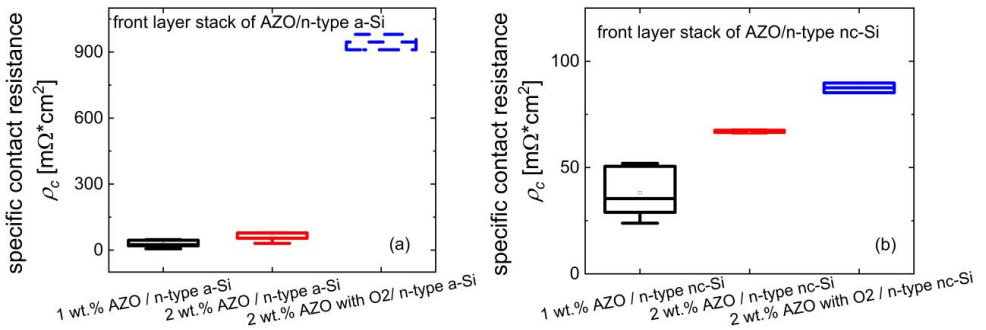
Fig. 5.21. Specific contact resistances for (a) front layer stack of AZO and n-type a-Si layers and (b) front layer stack of AZO and n-type nc-Si layers in 19 mm × 19 mm SHJ solar cells.

O_2 / n-type a-Si with high contact resistance marked in dashed box. The contact resistances for the 2 wt.% AZO with both n-type a-Si and n-type nc-Si layers are higher than the contact resistances for the 1 wt.% AZO / n-type Si layers, and even higher in the case when the O_2 is added into the precursor gas during sputtering. This further shows the advantage of the 1 wt.% AZO for the application in the SHJ solar cells.

As for the layer stack at the rear side, the contact resistances between TCO and Ag on p-type a-Si or p-type nc-Si are presented in Fig. 5.22(a). The TCO/Ag contacts for both of ITO and AZO on p-type a-Si and AZO on both of p-type a-Si and p-type nc-Si layer show low contact resistances approximately 5 mΩ*cm^2 or even lower. The contact between TCO and Ag show usual ohmic character. The contact resistances for rear layer stack of TCO and p-type Si layers are summarized in Fig. 5.22(b). The contact resistance between AZO and p-type a-Si is slightly lower than the contact resistance of ITO/p-type a-Si. However, for the AZO contact with p-type nc-Si layer, non-ohmic I-V curve is acquired from the TLM measurement, indicating carrier transport issues which will be addressed in chapter 7.
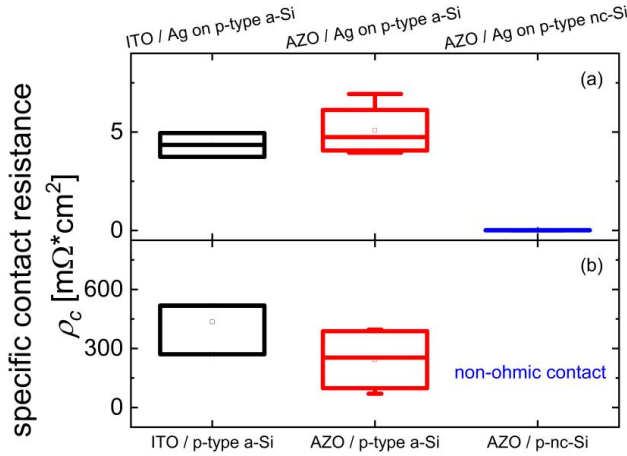
Fig. 5.22. Specific contact resistance for (a) TCO (AZO or ITO) and silver contact on p-type a-Si and p-type nc-Si layers and (b) rear layer stacks of TCO and p-type a-Si or nc-Si layers.

5.2.5 Result summary for both 19 mm × 19 mm and M2 size SHJ solar cells

The SHJ solar cells have been studied with various combinations of AZO and doped Si layers. The AZO films were sputtered with 1 wt.% target, 2 wt.% target and 2 wt.% target with 0.5% O_2 in the precursor gas at the substrate temperatures of 25°C, 150°C, and 200°C. The AZO films have been applied in the SHJ solar cells with four Si layer combinations as shown in Fig. 3.5. Cells with n-type nc-Si layer show higher J_{sc} compared to the cells with n-type a-Si layer. Cells with p-type a-Si layers show proper cell characteristics, and the cells with p-type nc-Si layers show improper

s-shaped J-V curves. Summary of the cell parameters is presented in Fig. 5.23. Dependencies of V_{oc} on target doping concentration and the precursor gas change do not show obvious trends. However, the V_{oc} values decreases with the increase of the AZO sputtering temperatures except for the AZO sputtered at 150ºC which may be due to the scatters in wafer quality or cleaning. Due to the higher doping for the 2 wt.% AZO target, higher carrier density of AZO layer results in higher absorption, thus lower J_{sc} values of cells with 2 wt.% AZO as compared to the cells with AZO sputtered with 1 wt.% target. Since the screen-printing method was used for the solar cells with the AZO sputtered with oxygen, the cell J_{sc} values are not comparable to the cells with evaporated silver and can only indicate the influence of the AZO sputtering temperature. In the case of J_{sc} value variation, the AZO sputtering temperature do not play a big role. However, the increase of AZO sputtering temperature reduces the FF obviously. The FF decreases with the increase of target doping as well. As for the η, it decreases with the increase of AZO sputtering temperature and AZO target doping concentration, and the highest η is acquired with the 1 wt.% RT sputtered AZO.
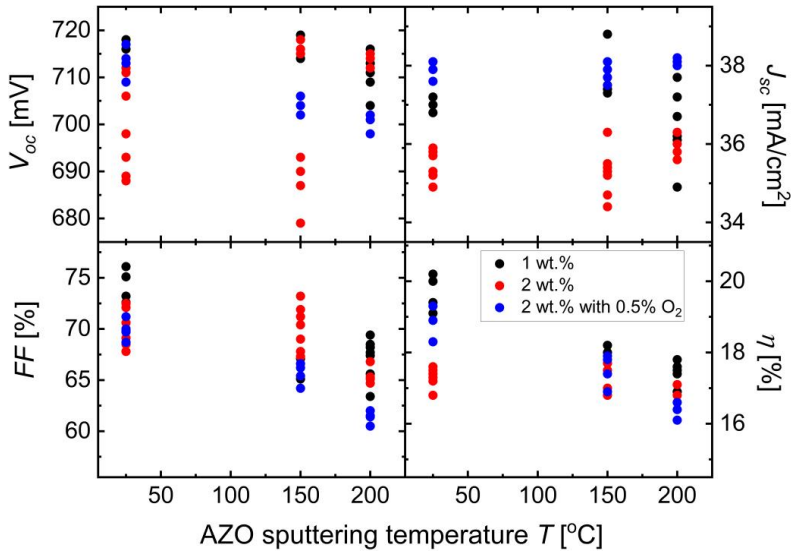
Fig. 5.23. Photovoltaic parameters (a) V_{oc}, (b) J_{sc}, (c) FF, and (d) η for the SHJ solar cells with 1 wt.% and 2 wt.% AZO sputtered at 25ºC, 150ºC, and 200ºC. The n-type nc-Si layer is used as window layer and p-type a-Si layer is used to form the junction.

The *IQE* and 1-reflection spectra of the SHJ solar cells with the AZO sputtered with 1 wt.% and 2 wt.% AZO targets at each temperature are shown in Fig. 5.24(a)-(c) and with AZO sputtered with 1 wt.% AZO target at 25ºC, 150ºC, and 200ºC are presented in Fig. 5.24(d). Generally, the *IQE* response variations show similar trends for each AZO sputtering temperature. The SHJ solar cells with AZO sputtered with 2 wt.% target show a lower *QE* response in the long wavelength region due to the higher free carrier absorption resulting from the higher carrier density in the AZO film. The SHJ solar cells with the AZO sputtered with 2 wt.% target with oxygen show slightly higher QE response in the short wavelength region due to the lower parasitic absorption. The SHJ solar cells with the AZO sputtered with 2 wt.% target with oxygen do not show the significant improvement in *QE* response compared to the cells with AZO sputtered with 1 wt.% target, but with the sacrifice of the conductivity. In this case the *IQE* response of the SHJ solar cells with the AZO sputtered with 1 wt.% target at 25ºC, 150ºC, and 200ºC are summarized in the Fig. 5.22(d). There is slight improvement in the short wavelength region with the increase of the AZO sputtering temperature. The *IQE* response variation proves that the AZO layer sputtered with 1 wt.% target at room temperature is the most suitable sputtering condition among studied conditions for SHJ solar cell fabrication.
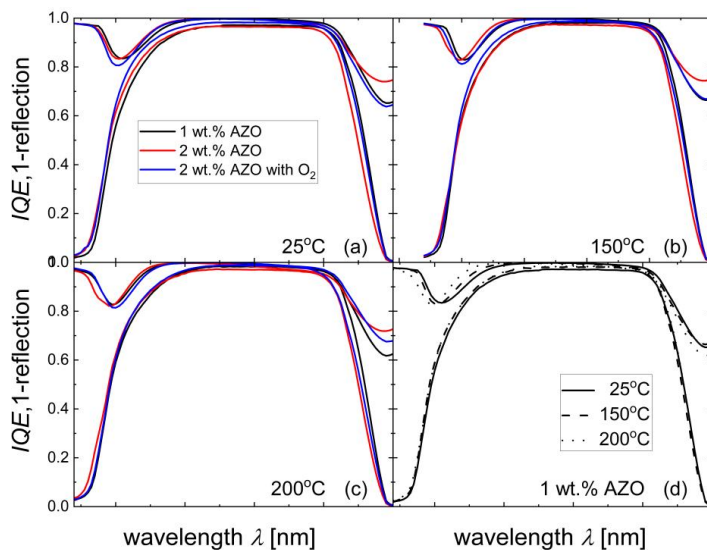
Fig. 5.24. Internal quantum efficiency and 1-reflection spectra of the SHJ solar cells with AZO sputtered with 1 wt.% and 2 wt.% targets at (a) 25ºC, (b) 150ºC, (c) 200ºC, and (d) with 1 wt.% AZO sputtered at 25ºC, 150ºC, and 200ºC, respectively. The n-type nc-Si layer is used as window layer and p-type a-Si layer is used for the junction formation.

With the established fabrication process chain for the M2 size wafers, the RT sputtered 1wt.% AZO and n-type nc-Si window layer were used to fabricated the M2 cells. In the M2 SHJ solar cells, 5 busbars front design was used during the screen printing. The J-V curve, *IQE* and 1-reflection response and the Electroluminescence spectra are presented in Fig. 5.25. The cell parameters are indicated with the J-V curve in Fig. 5.25 (a). The optimization for the M2 size solar cell will be focused in further.
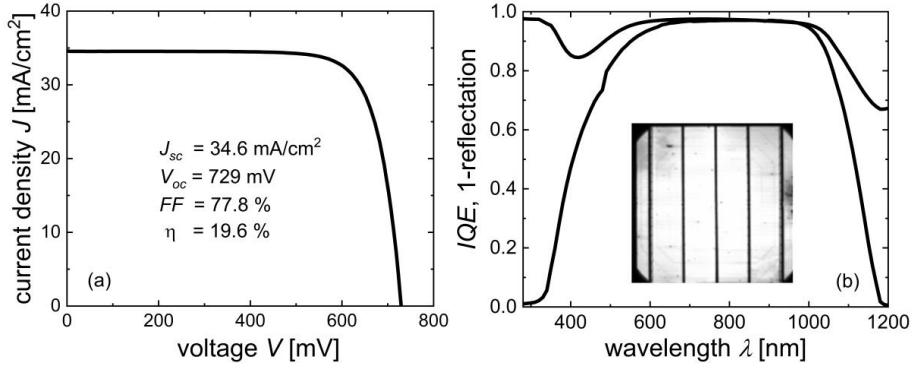
Fig. 5.25. (a) Light current density-voltage curves and (b) *IQE* response and 1-reflection spectra with the inset of the electroluminescence graph for the five busbar M2 SHJ solar cell.

5.3 Short summary

This chapter summarizes the application of AZO sputtered with various substrate temperatures, target doping concentrations, and precursors gas mixture in SHJ solar cells. AZO layers sputtered with 1 wt.% target, 2 wt.% target, and 2 wt.% target with 0.5% O_2 in precursor gas at the substrate temperatures of 25°C, 150°C, and 200°C have been applied in SHJ solar cells with four combinations of Si layers. The cells with n-type nc-Si layer presents higher J_{sc} as compared to the cells with n-type a-Si layer. The cells with p-type a-Si layer show proper cell characteristics, however, the cells with p-type nc-Si layer show improper cell characterizations with strong s-shaped J-V curves.

Variation of V_{oc} of solar cells does not show obvious trend over target doping concentration and precursor gas mixture during AZO sputtering. The V_{oc} value shows decrease trend with the increase of AZO sputtering temperatures. Lower J_{sc} values were observed for the cells with AZO sputtered with 2 wt.% target compared to the AZO sputtered with 1 wt.% target, which is due to the higher carrier density in AZO film resulting in higher parasitic absorption. AZO sputtering temperature have slight influence on J_{sc} variation. The *FF* decreases with increase of AZO sputtering temperature, target doping concentration, and adding of oxygen in the precursor gas during sputtering. The η decrease with the increase of the AZO sputtering temperature and AZO target

doping concentration. The highest η is acquired with the 1 wt.% RT sputtered AZO. The AZO sputtering parameters have slight influence on QE response. The cells with the three kinds of AZO films show comparable QE response at each sputtering temperature. Contact resistance between 1 wt.% AZO and n-type nc-Si layers is lower than the contact resistance between 2 wt.% AZO and n-type nc-Si. Therefore, RT sputtered 1 wt.% AZO is the most optimal set of parameters among studied options for SHJ solar cells. The efficiency of 21.2 % for the 19 mm × 19 mm cell was achieved with V_{oc} = 720 mV, J_{sc}= 39.1 mA/cm^2, and FF = 75.4 %. The efficiency of 19.3 % for the M2 size cell was achieved with V_{oc} = 732 mV, J_{sc}= 36.2 mA/cm^2, and FF = 72.8 %.

Chapter 6 Influence of AZO sputtering in SHJ Solar Cells

  This chapter describes the influence of AZO sputtering on the effective carrier lifetimes of Si layer stacks in SHJ solar cells. High effective carrier lifetime is a prerequisite for high open circuit voltage of SHJ solar cells and is achieved with surface passivation by intrinsic a-Si layer followed by doped Si layers. Measurements of the effective carrier lifetime τ_{eff} in wafers with Si layer stacks provide valuable information for process control and optimization of SHJ solar cells. In this work, dependencies of effective carrier lifetime on excess carrier density Δn have been measured with Quasi Steady-State Photo Conductance technique after silicon layer deposition, AZO sputtering, annealing in cell fabrication process, and AZO removal in investigation. Typical values of τ_{eff} at the Δn of 10^{15} cm^{-3}, implied open circuit voltage (iV_{oc}), and implied fill factor (iFF) have been extracted out of the QSSPC data. The effective carrier lifetime curves and the values of τ_{eff} are indicative for passivation quality in the Si layer structures, while iV_{oc} shows the lifetime limit of V_{oc} in SHJ solar cell, and the iFF shows the lifetime limit of FF [97].

  This chapter consists of three sections. The first section focuses on the influence of AZO sputtering on the effective carrier lifetime of symmetrical structures with intrinsic a-Si / n-type nc-Si (i/n stack) or intrinsic a-Si/p-type a-Si (i/p stack) on both sides of wafer. In this section, the influence of pressure and substrate temperature during AZO sputtering on the carrier lifetime in i/n and i/p symmetrical stacks has been investigated. Effect of room temperature sputtered AZO on the passivation in i/n symmetrical stacks with n-type nc-Si layer deposited with different r_{SiH4} was studied as well. The second section focuses on the influence of room temperature sputtered AZO on the passivation of cell precursors with i/n stack at front side and i/p stack at the rear side. In this section the influence of AZO geometry on the effective carrier lifetime curve is also addressed. The third section summarized the work carried out in this chapter.

6.1 Influence of AZO sputtering on the i/n and i/p symmetrical structures

In order to investigate the influence of AZO sputtering on the effective carrier lifetime in Si layer stacks, QSSPC measurements have been performed on symmetric structures after Si layer deposition, AZO sputtering, and annealing. The process sequence is presented in Fig. 6.1 (first three steps). The symmetrical structures are either i/n stack with nanocrystalline layer or i/p stack with amorphous layer on both sides of the wafers. Similar procedure has been applied to the SHJ solar cell precursor stacks in section 6.2. Same AZO sputtering parameters have been applied to the front and rear sides of the symmetrical stacks. The following annealing at either 180°C for 30 min or 190°C for 40 min in air is compatible with the typical sintering or curing step [98] applied after metallization in SHJ solar cell fabrication process. Variation in annealing parameters is related to the optimization of metallization process and has negligible influence on the properties of AZO films.

Every new layer prepared on Si layer stack may change the effective carrier lifetime either due to the impact of preparation process on the existing layers, or the properties of the new layer itself, e.g. via field effect. In this case AZO sputtering process may damage the underlying layers and at the same time the presence of AZO film may change occupation of the electronic states in the interface region. Both of them can affect effective carrier lifetime. In order to separate the impact of AZO sputtering process from the effect of the presence of AZO itself on the effective carrier lifetime, the AZO film was removed by 0.5 wt.% HCl solution after annealing shown as the last step in Fig. 6.1.

The wet chemical etching was chosen as a robust and simple method to remove AZO, however, it is known that exposure of thin-film Si layers to air or aqueous solutions may influence conductivity [99, 100] or charge state of defects in thin-film Si layers [101] which in turn may influence the effective carrier lifetime. In order to study possible influence of HCl solution etching on the effective carrier lifetime, QSSPC measurement was conducted before and after i/n and i/p stacks exposed to 0.5 wt.% HCl solution, respectively.
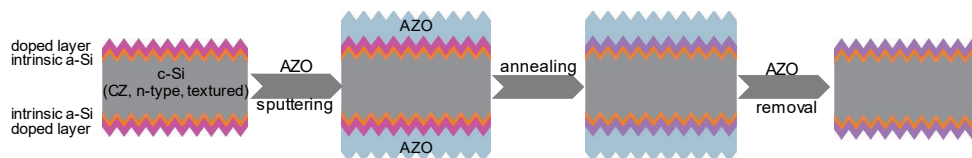
Fig. 6.1. Treatment procedures on i/n and i/p symmetrical stacks with doped Si layers on both sides of wafer in sequence of Si layer stack deposition - AZO sputtering - annealing - AZO removal.
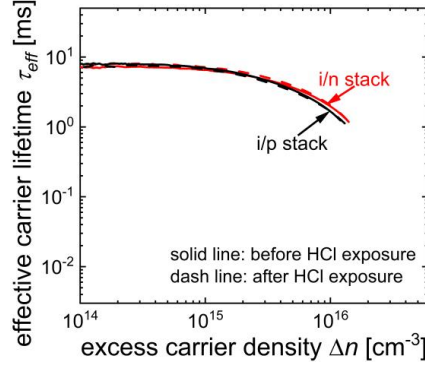
Fig. 6.2. Effective carrier lifetime versus excess carrier density curves for i/n and i/p symmetrical stacks before and after 0.5 wt.% HCl solution exposure.

The effective carrier lifetime dependencies on excess carrier density are presented in Fig. 6.2. For both i/n and i/p stacks, exposure to 0.5 wt.% HCl solution has no influence on the measured effective carrier lifetime curves. The related variations of iV_{oc} and iFF values are presented in Fig. 6.3. The iV_{oc} values before and after HCl etching are 748 mV and 750 mV for i/n stack; and 748 mV and 745 mV for i/p stack. The iFF values before and after HCl etching are 85.2% and 85.3%
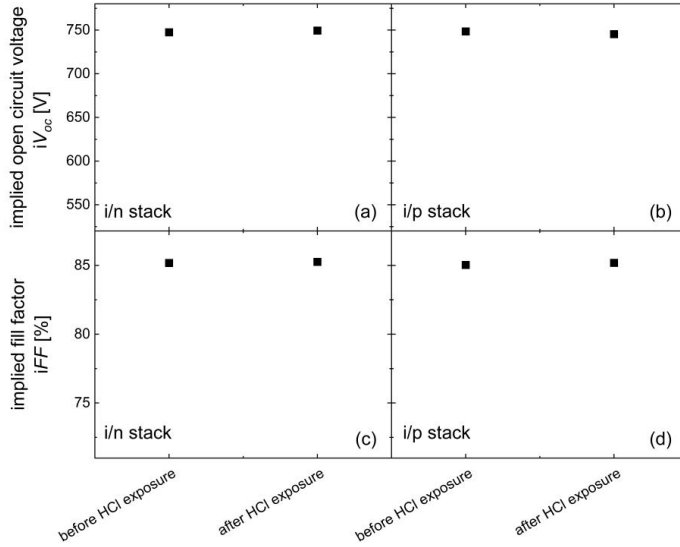
Fig. 6.3. Implied open circuit voltage (iV_{oc}) and implied fill factor (iFF) variations for i/n and i/p symmetrical stacks before and after 0.5 wt.% HCl solution exposures.

for i/n stack, and 85.0% and 85.2% for i/p stack. It can be concluded that HCl etching has no influence on both lifetime and iV_{oc} and iFF values of the measured samples. Therefore, removing AZO by exposing to 0.5 wt.% HCl solution provides a practical way to evaluate the effective carrier lifetime after AZO sputtering process.

6.1.1 Influence of AZO sputtering parameters on the i/n and i/p symmetrical structure

Effect of the pressure during AZO sputtering on effective carrier lifetime in symmetrical structures has been studied and the lifetime variations are presented in Fig. 6.4. The AZO depositions for the pressure series with 0.1, 0.3, and 0.5 Pa were performed at room temperature. Results for all samples in pressure series show qualitatively same trends: high initial carrier lifetime is significantly reduced after AZO sputtering and mostly recovered after annealing. The samples with i/n stack show almost complete recovery after annealing. Further removal of AZO slightly improves the effective carrier lifetime as shown in Fig. 6.4(a)-(c). However, the samples with i/p stack show incomplete lifetime recovery after annealing in the low excess carrier density region which is eliminated by AZO removal shown in Fig. 6.4(d)-(f). These results indicate that on the one hand the detrimental effect of AZO sputtering process on Si layers is eliminated

Fig. 6.4. Effective carrier lifetime versus excess carrier density curves for i/n (a)-(c) and i/p (d)-(f) symmetrical stacks with the treatment procedures: Si layer stack deposition - AZO sputtering - annealing - AZO removal. The experiments have been performed at room temperature with three AZO sputtering pressures: 0.1, 0.3, and 0.5 Pa as noted in each graph.

completely by annealing and on the other hand the presence of AZO film results in the reduction of the effective carrier lifetime in the low excess carrier density region. This latter reduction could result from work function mismatch between AZO and Si layer which contributed to the reduction of field effect passivation [102].

Fig. 6.5 shows the influence of AZO sputtering pressures on the values of iV_{oc} and iFF in the symmetrical stacks with the treatment procedures: Si layer deposition, AZO sputtering, annealing, and AZO removal. For both i/n and i/p stacks with different AZO sputtering pressures, the variations of iV_{oc} and iFF show same trends and are consistent with the effective carrier lifetime variation with the same treatment procedures. High iV_{oc} and iFF are achieved after Si layer deposition. AZO sputtering reduces iV_{oc} and iFF significantly. The following annealing recovers the iV_{oc} and iFF and further AZO removal has no effect on the values variation. Note that the incomplete recovery at low carrier density in i/p stacks shown in Fig. 6.4 has no influence on iV_{oc} and iFF. In summary the pressure variation does not alter neither the detrimental effect of AZO sputtering on the τ_{eff}, iV_{oc} and iFF, nor the way it is recovered upon annealing.

Fig. 6.5. Implied open circuit voltage and implied fill factor variations for i/n (a), (c) and i/p (b), (d) symmetrical stacks with the treatment procedures: Si layer stack deposition - AZO sputtering - annealing - AZO removal. The experiments have been performed at room temperature with three AZO sputtering pressures: 0.1, 0.3, and 0.5 Pa as noted in each graph.

Increase of substrate temperature of AZO sputtering has obvious influence on the effective lifetime of both i/n and i/p symmetrical stacks as presented in Fig. 6.6. The degradation of the effective carrier lifetime after AZO sputtering at 150°C is much smaller as compared to the RT process and at 200°C there is no degradation observed. Qualitatively the effect of the elevated substrate temperature is consistent with the fact that the degradation of the effective carrier lifetime is eliminated by annealing. Except for these observations the damage observed in samples after AZO sputtering at RT and 150°C was eliminated by post-deposition annealing. Consistently no influence of post-deposition annealing on the samples after AZO sputtered at 200 °C has been observed. Comparing i/n and i/p stacks in Fig. 6.6, the dependence of effective carrier lifetime on all treatment procedures are nearly same for both i/n and i/p stacks with different substrate temperatures except for the low excess carrier density region in i/p stacks. In the case of i/p stack presence of AZO reduces effective carrier lifetime in the low excess carrier density region for all temperatures which is consistent with Ref. [102].
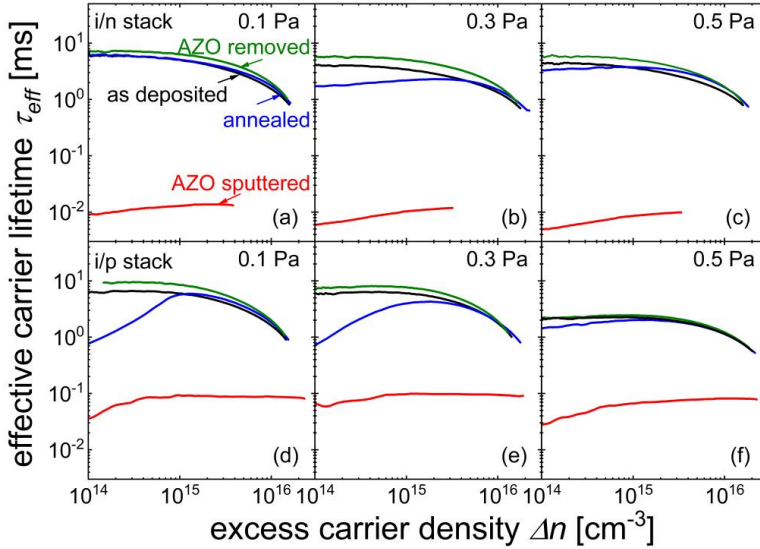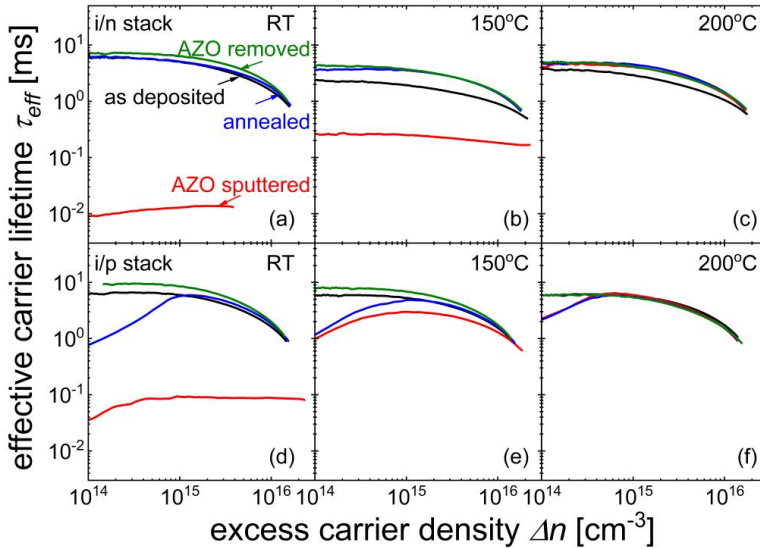

Fig. 6.6. Effective carrier lifetime versus excess carrier density curves for i/n (a)-(c) and i/p (d)-(f) symmetrical stacks with the treatment procedures: Si layer stack deposition - AZO sputtering - annealing - AZO removal. The experiments have been performed with pressure of 0.1 Pa at three substrate temperatures: RT, 150°C, and 200°C as noted in each graph.

Similarly, for the AZO substrate temperature series, the variation of iV_{oc} and iFF in the symmetrical stacks upon with the treatment procedures: Si layer deposition, AZO sputtering, annealing, and AZO removal are presented in Fig. 6.7. Increase in temperature reduces degradation of both iV_{oc} and iFF after AZO sputtering due to in-situ annealing. The annealing step contributes to the recovery of iV_{oc} and iFF for the AZO sputtering at RT and 150°C, especially the RT case. There is no decrease of iV_{oc} and iFF after AZO sputtering at 200°C and both annealing and AZO removal have no influence on the variation of iV_{oc} and iFF due to the high substrate temperature during AZO sputtering.
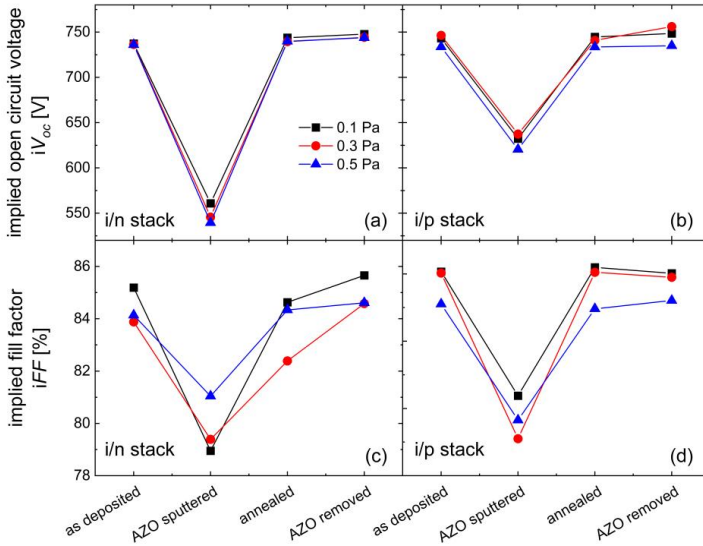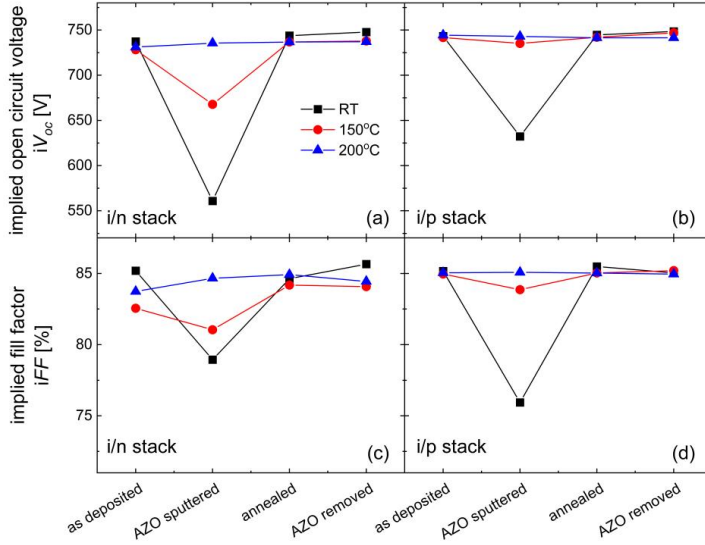

Fig. 6.7. Implied open circuit voltage and implied fill factor variations for i/n (a), (c) and i/p (b), (d) symmetrical stacks with the treatment procedure: Si layer stack deposition - AZO sputtering - annealing - AZO removal. The experiments have been performed with pressure of 0.1 Pa at three AZO sputtering substrate temperatures: RT, 150°C, and 200°C as noted in each graph.
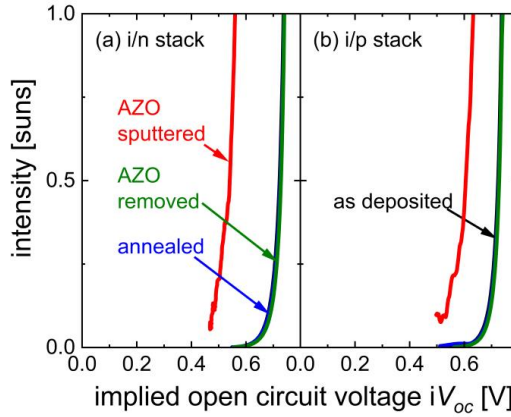
Fig. 6.8. Light intensity versus implied open circuit voltage curves for (a) i/n, and (b) i/p symmetrical stacks with the treatment procedure: Si layer stack deposition - AZO sputtering - annealing - AZO removal. The experiments have been performed with AZO sputtered at RT and pressure of 0.1 Pa.
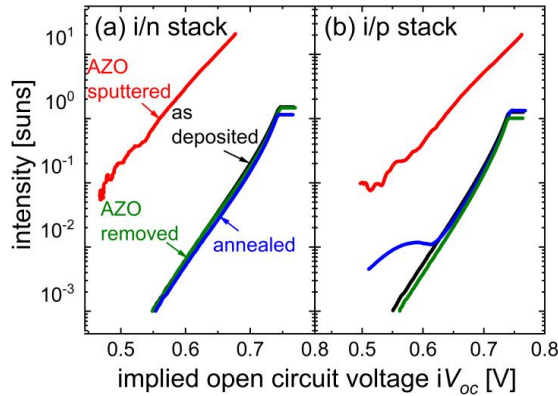
Fig. 6.9. Light intensity versus implied open circuit voltage curves for (a) i/n, and (b) i/p symmetrical stacks with the treatment procedure: Si layer stack deposition - AZO sputtering - annealing - AZO removal. The experiments have been performed with AZO sputtered at RT and pressure of 0.1 Pa. The light intensity axis was converted into logarithm scale from Fig. 6.8.

It can be seen in Fig. 6.4 and Fig. 6.6 that the i/n stack with nanocrystalline phase is more sensitive to the influence of the AZO sputtering or the ion bombardment than i/p stack with the amorphous phase. The lifetime degradation after AZO sputtering for the i/n stack with n-type nanocrystalline Si is severer than the degradation for i/p stack with p-type amorphous Si. There is a lifetime decrease region in the low excess carrier density region for the i/p symmetrical stack

after annealing. Since this decrease in low excess carrier density region has no influence on the variation of lifetime, iV_{oc} and iFF, it is meaningful to study whether it has influence on the I-V characterization of SHJ solar cells. The dependence of light intensity on iV_{oc} for both i/n and i/p stacks with the AZO sputtered at RT and with 0.1 Pa were compared in Fig. 6.8 with the same treatment procedures. It shows the same variation trends for both i/n and i/p stacks. The AZO sputtering decreases the light response of the stacks, and the annealing recovers it, while the further AZO removal has no influence on it. To observe further details, the light intensity axis shown in Fig. 6.8 was converted into logarithm scale as presented in Fig. 6.9. It can be seen clearly that there is an unusual bend in the i/p stack after annealing which is clearly related to the lifetime decrease in the low excess carrier density region as shown in Fig. 6.4 or Fig. 6.6. Since solar cell works in the high injection region, this unusual bend has no influence on the output of the solar cell under 1-sun illumination.

6.1.2 Influence of AZO sputtering on varied i/n symmetrical structure

For further investigation of the AZO sputtering influence on passivation in n-type Si layers, the AZO layer was sputtered at RT with 0.1 Pa pressure on the n-type Si layers with varied ϕ_{SiH4}/ϕ_{H2}
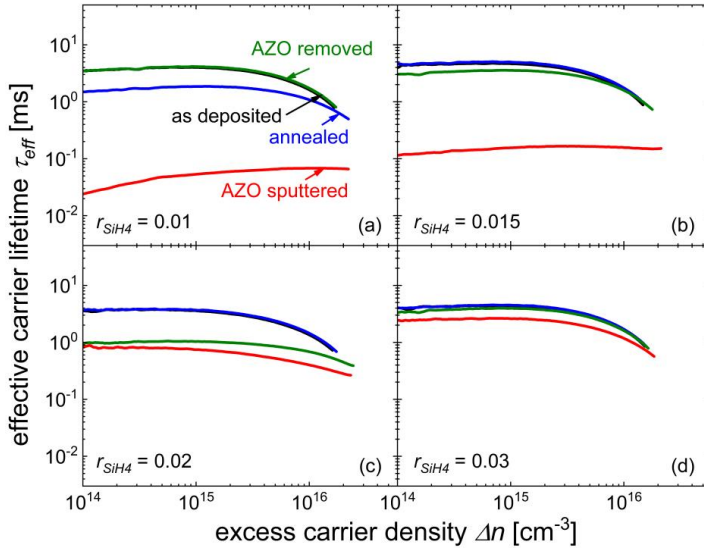
Fig. 6.10. Effective carrier lifetime versus excess carrier density curves for i/n symmetrical stacks deposited with the gas flow rate ratio r_{SiH4} of 0.01, 0.015, 0.02, and 0.03 with the treatment procedures: Si layer stack deposition - AZO sputtering - annealing - AZO removal. The AZO was sputtered at RT with pressure of 0.1 Pa. The n-type Si layers are deposited with same thickness.

Fig. 6.11. Implied open circuit voltage and implied fill factor variations for i/n symmetrical stacks deposited with r_{SiH4} of 0.01, 0.015, 0.02, and 0.03 with the treatment procedures: Si layer stack deposition - AZO sputtering - annealing - AZO removal. The AZO was sputtered at RT with pressure of 0.1 Pa. The n-type Si layers are deposited with same thickness.
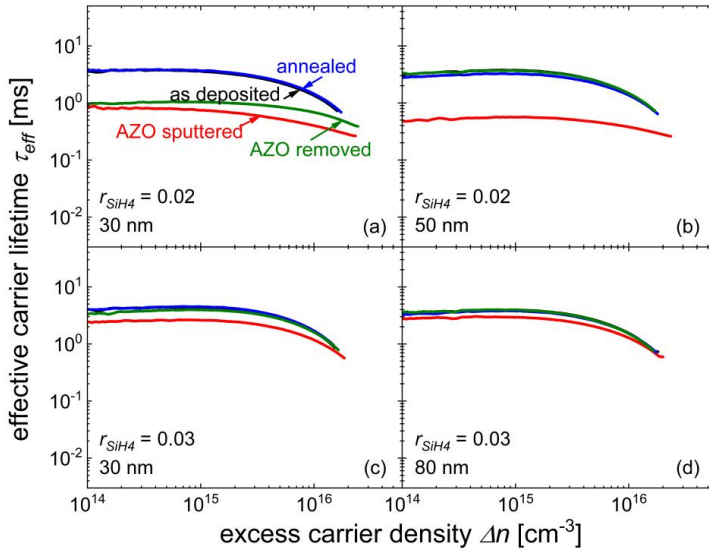
Fig. 6.12. Effective carrier lifetime versus excess carrier density curves for i/n symmetrical stacks deposited at the r_{SiH4} of 0.02 with the thickness of 30 nm and 50 nm, and r_{SiH4} of 0.03 with the thickness of 30 nm and 80 nm in the treatment procedures: Si layer stack deposition - AZO sputtering - annealing - AZO removal. The AZO was sputtered at RT with pressure of 0.1 Pa.

flow rate ratios r_{SiH4} and layer thickness. The r_{SiH4} of 0.01, 0.015, 0.02, and 0.03 have been tested for n-type Si layer with the same thickness. The variation of lifetime is presented in Fig. 6.10 and variations of iV_{oc} and iFF are presented in Fig. 6.11.

Fig. 6.10 shows that the lifetime degradation after AZO sputtering has been reduced by increasing r_{SiH4}. The annealing step can effectively recover the damage form AZO sputtering and AZO removal does not influence carrier lifetime. The behavior of the lifetime dependencies is translated into the variation of iV_{oc} and iFF. As observed in Fig. 6.11 that the iV_{oc} and iFF values decrease after AZO sputtering, recover after annealing, and are not affected by the AZO removal. It can be obviously seen that increase of r_{SiH4} reduces the degradation of both iV_{oc} and iFF values.

For the n-type Si layers deposited with r_{SiH4} of 0.02 and 0.03, different thicknesses have been prepared to study the influence of AZO sputtering on the passivation of Si layers. The lifetime variation is presented in Fig. 6.12 and the variation of iV_{oc} and iFF values is presented in Fig. 6.13. For the n-type Si layers deposited with r_{SiH4} of 0.02 or 0.03, dependencies of lifetime for n-type Si layers deposited with varied thickness on the treatment procedures are quite similar. In line with this, the variations of iV_{oc} and iFF values only have slight difference between the two thicknesses series of n-type nc-Si layers deposited with r_{SiH4} of 0.02 or 0.03 as shown in Fig. 6.13. There is a scatter for the lifetime curve of Si layer deposited with r_{SiH4} of 0.02 and thickness of 30 nm measured after AZO removed in Fig. 6.12(a). The related iV_{oc} and iFF points in Fig. 6.13(a) and
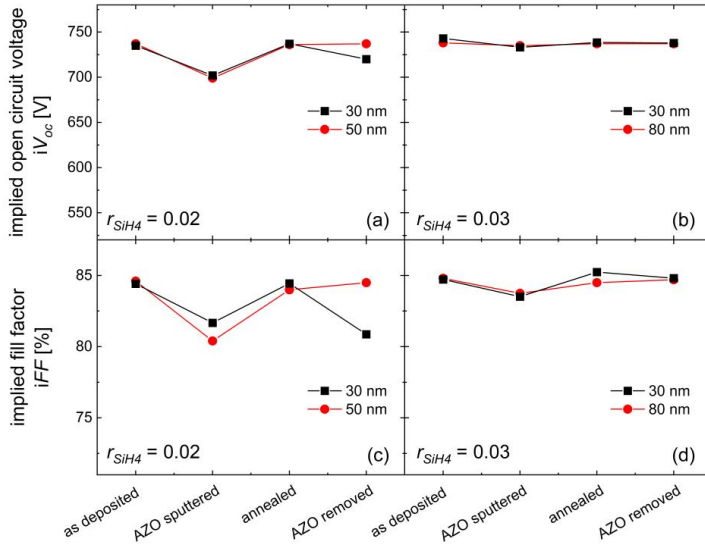
Fig. 6.13. Implied open circuit voltage and implied fill factor variations for i/n symmetrical stacks deposited at r_{SiH4} of 0.02 with the thickness of 30 nm and 50 nm, and r_{SiH4} of 0.03 with the thickness of 30 nm and 80 nm in the treatment procedures: silicon layer stack deposition - AZO sputtering - annealing - AZO removal. The AZO was sputtered at RT with pressure of 0.1 Pa.

Fig. 6.13(c) are also related to it. Therefore, AZO sputtering is more critical to the interface between Si layer and the c-Si wafers instead of the Si layer bulk itself [103].

The significant degradation of the passivation quality after AZO sputtering process could be related to either ion bombardment damage [104] or light-induced degradation from the plasma luminescence during sputtering process [103, 105]. The annealing process recovers the effective carrier lifetime from the damage introduced by AZO sputtering process and similar observations have been reported for ITO with a-Si:H layers [106]. It can be speculated that the improvement of passivation quality results from the passivation of defects, e.g. dangling bonds due to the diffusion of hydrogen from the trapped states at the a-Si:H/c-Si interface and in the a-Si:H bulk during the annealing [104, 107]. For further investigation on the damage mechanism, a quartz glass can be applied in front of the symmetrical stacks during AZO sputtering to distinguish the influence of ion bombardment and plasma luminescence on the degradation of effective carrier lifetime.

6.2 Influence of AZO on SHJ solar cell precursors

After the study of symmetrical structures, the measurements of effective carrier lifetime were carried out after each fabrication step in SHJ solar cell precursor prior to the metallization to monitor the passivation quality. In the cell fabrication, the annealing step to recover lifetime is combined with the curing step after metallization. In this way the effective carrier lifetime cannot be measured after annealing to investigate the recovery after AZO sputtering. Therefore, the cell stacks without metallization have been processed as follows: Si layer deposition, AZO sputtering, and annealing, which is schematically presented in Fig. 6.14. Annealing step was performed prior to metallization in order to access the value of effective carrier lifetime after annealing. The evolution of effective carrier lifetime of the cell stack over the process sequence is presented in
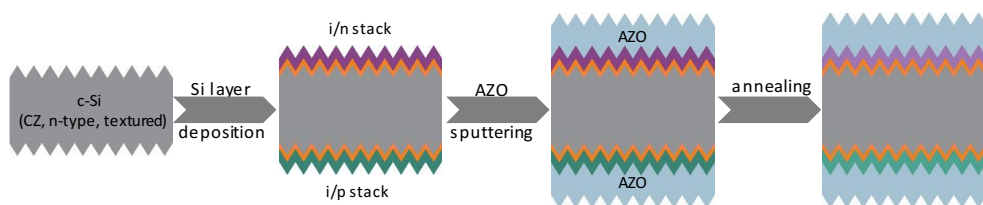
Fig. 6.14. Schematically illustration for the steps applied to the cell stack in the sequence of Si layer stacks deposition - AZO sputtering - annealing. Compared to the SHJ solar cells, the cell stack has the same structure, while with this sample, annealing was applied directly after the AZO sputtering and no further metallization.
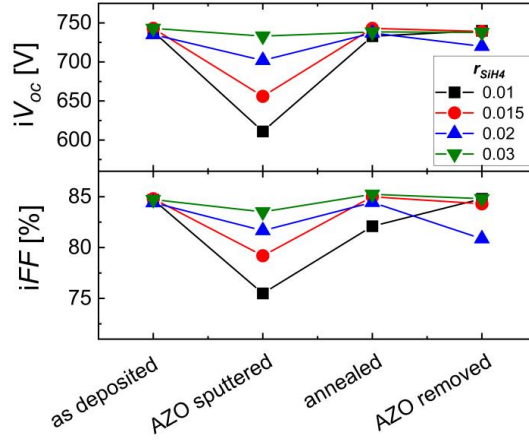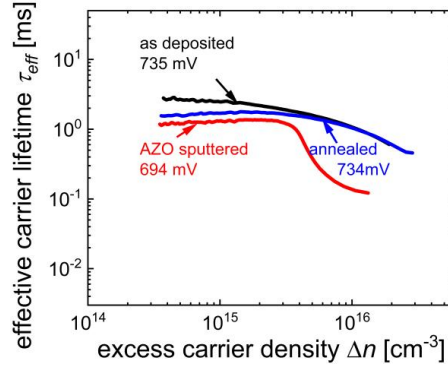
Fig. 6.15. Effective carrier lifetime versus excess carrier density curves for cell stacks with patterned AZO with the treatment procedure: Si layer stack deposition - AZO sputtering - annealing.

Fig. 6.15. Dependencies in Fig. 6.15 show that the effective carrier lifetime is reduced after AZO sputtering, and there is a severe reduction of effective carrier lifetime in the high excess carrier density region leading to rather unusual sharp bend of the lifetime curve at Δn approximately 5×10^{15} cm^{-3}. This unexpected feature has been presented in our previous work [108]. Qualitatively this severe decrease of the effective carrier lifetime (sharp bend in lifetime curve) was observed in all solar cell precursors prior to metallization with AZO geometry presented in Fig. 6.16. However, this sharp bend in lifetime curves did not appear in the symmetrical structures with AZO prepared on full area. In the cell precursor case the area of the inductive sensor of the QSSPC setup is covered by a combination of AZO area and non-AZO area as shown in Fig. 6.16. The patterned AZO geometry in cell stacks results in the unusual shape of lifetime curve compared to the typical curve from the full area AZO covered samples. Therefore, the sharp bend in the lifetime curve after AZO sputtering shown in the Fig. 6.15 is attributed to a measurement artifact.
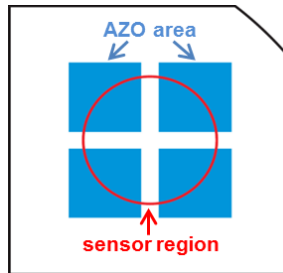
Fig. 6.16. Illustration of AZO geometry on 78 mm × 78 mm size wafer with four 19 mm × 19 mm size solar cells and its alignment in the effective carrier lifetime measurement with QSSPC.

In order to verify the effect of AZO geometry, the same treatment procedure was applied to the i/n and i/p symmetrical stacks with patterned AZO shown in Fig. 6.16. The treatment process is presented in Fig. 6.17 and the effective carrier lifetime variation is shown in Fig. 6.18.
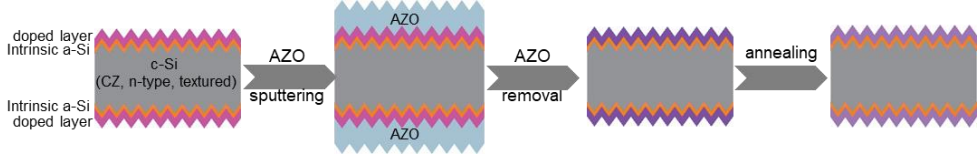
Fig. 6.17. Treatment procedures on the i/n and i/p symmetrical stack with doped silicon layers in the sequence of Si layer stack deposition - AZO sputtering - AZO removal - annealing.

In Fig. 6.18 it can be seen that both symmetrical stacks show similar lifetime evolution trends. High effective carrier lifetime is achieved after Si layer deposition, while decreases significantly after sputtering of patterned AZO and shows obviously sharp bends at the excess carrier density approximately 3×10^{15} cm^{-3}. This sharp bend was disappeared after that the patterned AZO was removed, which is further proved that the sharp bend in lifetime curve is from the AZO geometry in the SHJ solar cells. It points out the importance for the proper measurement with proper structure.

Detailed analysis of the sample geometry effect requires simulations to account for carrier diffusion with spatial resolution which can be done in future. For the presented dataset the lifetime measurements performed on the cell structures with patterned AZO are not analyzed further.

In order to access the influence of AZO deposition on the lifetime, iV_{oc} and iFF in cell precursors the equivalent samples with full area AZO coverage was prepared and the lifetime variation over the treatments is presented in Fig. 6.19. The variation of effective carrier lifetime follows the same
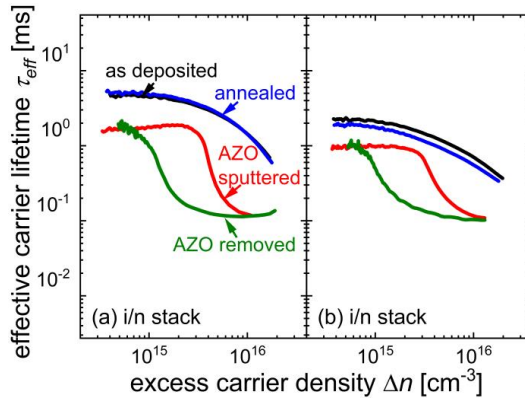
Fig. 6.18. Effective carrier lifetime versus excess carrier density curves for (a) i/n and (b) i/p symmetrical stacks with patterned AZO with the treatment procedure: Si layer stack deposition - AZO sputtering - AZO removal - annealing.
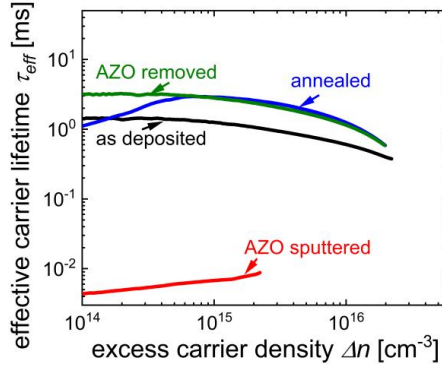
Fig. 6.19. Effective carrier lifetime versus excess carrier density curves for solar cell stack with full AZO coverage following the treatment procedure: Si layer stack deposition - AZO sputtering - AZO removal - annealing.

trend as the symmetrical stacks and the iV_{oc} values are 716 mV after Si layer deposition, 537 mV after AZO sputtering, and 735 mV after annealing. This high iV_{oc} value after annealing indicates the potential of high V_{oc} for solar cells and the potential to apply room temperature sputtered AZO in SHJ solar cells.

6.3 Short summary

The influence of AZO sputtering on the effective lifetime of symmetrical structures with intrinsic a-Si/n-type nc-Si (i/n stack) or intrinsic a-Si/p-type a-Si (i/p stack) on both sides of Si wafer has been explored. The lifetime has been monitored after each treatment step of the stack preparation procedure in the sequence of Si layer stack deposition, AZO sputtering, annealing, and AZO removal. The effects on carrier lifetime originates from either AZO sputtering process or the presence of AZO layer itself. Varied pressures and substrate temperatures during AZO sputtering and different r_{SiH4} for n-type Si layer deposition have been investigated for their influence on the passivation in i/n and i/p symmetrical structures.

Generally high initial carrier lifetime after Si layer deposition is significantly reduced after AZO sputtering and mostly recovers after annealing. The detrimental effect of AZO sputtering process on passivation of Si layers is eliminated completely by annealing. While, less-recovered effective carrier lifetime in the low excess carrier density region was observed for the i/p stack, which is from the presence of AZO. The possible reason for it is the work function mismatch between AZO and Si layer contributed to the reduction of field effect passivation, thus reducing the lifetime.

For the symmetrical stacks, the pressure variation did not alter neither the detrimental effect of AZO sputtering on the τ_{eff}, iV_{oc}, and iFF, nor the way it recovered upon annealing. Increase of substrate temperature of AZO sputtering has obvious improvement on the effective carrier lifetime

of both i/n and i/p symmetrical structures due to the in-situ annealing. Higher ratio of r_{SiH4} for the n-type Si layer contributes to reducing AZO sputtering damage which may due to the increased amorphous phase in Si layer. The thickness of the Si layer did not play a big role during the AZO sputtering.

During the AZO sputtering, the ion bombardment and plasma illuminance may result in the damage of the defects passivation in Si layers. Influence of AZO patterning on the dependencies of effective carrier lifetime on excess carrier density was tested. The results point out that the proper measurement has to avoid TCO patterns with feature size smaller than QSSPC sensor.

Lifetime monitoring performed on cell precursors has shown similar lifetime evolution upon treatment procedure as the symmetrical stacks studied earlier. After annealing, the lifetime in the low excess carrier density is not recovered completed for the i/p stack. The incomplete lifetime recovery has no influence on the iV_{oc} and iFF, thus the solar cell operation. Moreover, the results obtained from the research on the passivation of solar cell precursor are meaningful for the further loss analysis in SHJ solar cells.

Chapter 7 Contacts at the interfaces between AZO and p-type Si layers

This chapter describes the contact at the interface between AZO and p-type Si layer in SHJ solar cells. In general, there is low possibility of non-ohmic contact formation at the interface between AZO and n-type Si layer. In contrast, contact between AZO and p-type Si layers is often non-ohmic due to the Schottky barrier at the interface. The pronounced s-shaped current density-voltage characteristics of solar cells with p-type nc-Si shown in chapter 5 indicates the existence of the carrier collection barrier. Considering the potential to reduce series resistance in cells with more conductive p-type nc-Si layer and to reduce the contact barrier between p-type nc-Si layer and AZO, detailed study on cells with the combination of p-type nc-Si and AZO was performed.

In this chapter, the content is divided into four sections. Section 7.1 describes the investigation on the s-shaped J-V characteristic by introducing an extra p-type a-Si layer in SHJ solar cells. Section 7.2 describes the analysis of contact barrier at the interface between AZO and p-type nc-Si in the aspect of thermal activation and electrical properties. Section 7.3 presents optimization for the contact barrier with variations in p-type nc-Si layer with doping and thickness as well as application of a seed layer and variations in the AZO with sputtering temperature and doping concentrations. Section 7.4 summaries the work on the contact between the AZO and p-type nc-Si and provides directions for further optimization.

7.1 J-V characteristics for the SHJ solar cells with AZO and p-type Si layers

In chapter 5, the light J-V curves of SHJ solar cells with RT sputtered 1 wt.% AZO and different Si layer combinations of (1) n-type a-Si / p-type a-Si, (2) n-type nc-Si / p-type a-Si, (3) n-type a-Si / p-type nc-Si, and (4) n-type nc-Si / p-type nc-Si have been presented in Fig. 5.3. The solar cells with p-type a-Si layers show typical photodiode J-V characteristics. However, the solar cells with p-type nc-Si layers show pronounced s-shaped light J-V characteristics. Contrary to the expectations based on experience with thin-film Si solar cells [92], the combination of AZO and

p-type nc-Si layer appears to be most challenging in this case. Referred to the J-V characteristic of the cells with p-type a-Si layer, the front layer stack, the rear intrinsic a-Si layer, and the contact at the interface of AZO and silver have no contribution to the s-shaped J-V curve for the solar cells with p-type nc-Si layer. Therefore, the reasons for the s-shaped J-V curve of the cells with p-type nc-Si layer is either the non-optimized bulk properties of the p-type nc-Si layer or the poor contact at the interface of AZO and p-type nc-Si layer.

To identify the reasons for the s-shaped J-V curve, an extra p-type a-Si layer was introduced prior to or after the deposition of p-type nc-Si layer in the solar cells sketched in Fig. 7.1. Since the p-type nc-Si layers are presented in both cells with extra p-type a-Si layer, influence of the bulk property of p-type nc-Si layer on the s-shaped J-V characteristics is included in both cases, and the difference is the contact interfaces between AZO and p-type Si layers.

J-V curves for these two cells are compared with the reference cell with p-type nc-Si layer in Fig. 7.2. The reference cell shows s-shaped J-V curve with reduced V_{oc}. The cell with extra p-type a-Si layer which contacts to AZO shows proper light J-V characteristic and normal V_{oc} and low FF. The low FF is due to high bulk series resistance resulting from the increased thickness in the p-type Si layer stack. The proper J-V characteristic of this cell indicates that the contact between intrinsic a-Si and p-type nc-Si does not result in the s-shape in the J-V curve as well. The cell with p-type a-Si and p-type nc-Si layer which contacts to AZO shows s-shaped J-V curve with reduced V_{oc}, which is similar to the J-V curve from the cell with p-type nc-Si. The increased FF compared to the reference cell is due to the introduced p-type a-Si between intrinsic a-Si and p-type nc-Si layers. Therefore, the transport barrier at the interface of p-type nc-Si and AZO layer instead of the p-type nc-Si bulk property is the dominant reason for the s-shaped J-V characteristic.
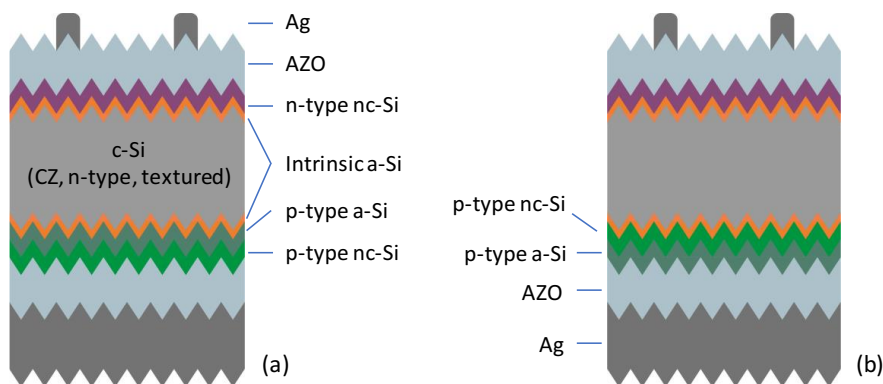
Fig. 7.1. Schematic illustrations for the cells with an extra p-type a-Si layer deposited prior to or after p-type nc-Si layer: (a) p-type nc-Si contacts with AZO, (b) p-type a-Si contacts with AZO.

Fig. 7.2. Light J-V curves for the SHJ solar cells with an extra p-type a-Si layer deposited prior to (p-type nc-Si layer contacts with AZO) or after p-type nc-Si layer (p-type a-Si contacts with AZO). The light J-V curve for the SHJ solar cells with p-type nc-Si was plotted as well for reference.

7.2 Analysis on the contact barrier between AZO and p-type nc-Si

The observed s-shaped J-V curves are usually related to a transport barrier which is expected to be thermally activated. Thus, the light J-V curves of the SHJ solar cell with p-type nc-Si layer were measured at the temperatures in the range of 25-75°C. The cell with p-type a-Si layer was measured at varied temperatures as well for reference. The light J-V curves for cells with either p-type a-Si or p-type nc-Si layers are shown in Fig. 7.3. All J-V curves of the cell with p-type a-Si layer show typical photodiode J-V characteristics with the increased measurement temperatures as shown in Fig. 7.3(a). Cell V_{oc} gradually decreases with the increase of measurement substrate temperature due to the increased saturation current. Cell J_{sc} slightly increases due to the slightly narrowed band gap. However, the light J-V curves of the SHJ solar cells with p-type nc-Si layer in Fig. 7.3(b) show obvious s-shape. With the increase of substrate temperature, the s-shape in light J-V curves is gradually vanishing. This thermal activation of the photocurrent is qualitatively consistent with a classical potential barrier for photogenerated charge carriers at the back contact of the device. Simultaneously the natural decrease of V_{oc} with temperature increase is observed. The cell J-V characteristics at elevated temperatures in the range of 25-75°C further prove that the contact property at the interface between p-type nc-Si and AZO is critical to diode behavior.
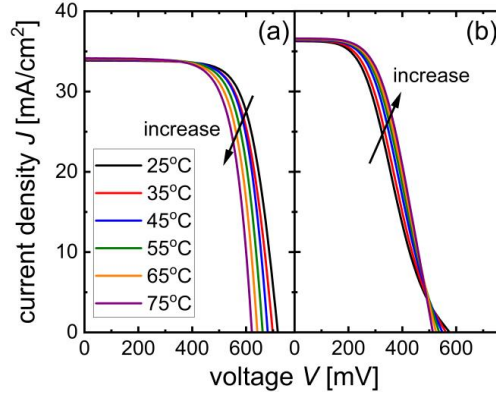
Fig. 7.3. Light J-V curves for the SHJ solar cells with (a) n-type a-Si and p-type a-Si; (b) n-type nc-Si and p-type nc-Si layer combinations measured at the temperatures of RT (25°C), 35°C, 45°C, 55°C, 65°C, and 75°C, respectively.

To further investigate on the barrier at the interface between p-type nc-Si and AZO, the I-V characteristic of the barrier were reconstructed using light I-V, dark I-V, and I_{sc}-V_{oc} curves of the solar cell with p-type nc-Si layer as shown in Fig. 7.4. The analysis was based on the series resistance extraction method [109, 110]. The I_{sc}-V_{oc} curve is not influenced by series resistance and therefore by the transport barrier. The voltage offset ΔV between light I-V and I_{sc}-V_{oc}, as well as between dark I-V and I_{sc}-V_{oc}, represents the voltage drop at the series resistance of the solar cell at a given current. The voltage offset between light I-V and and I_{sc}-V_{oc} is denoted as ΔV_l, and the offset between dark I-V and I_{sc}-V_{oc} as ΔV_d. The sign of the voltage offset is determined by the direction of the net current. For the case of an ohmic series resistance the ΔV depends linearly on
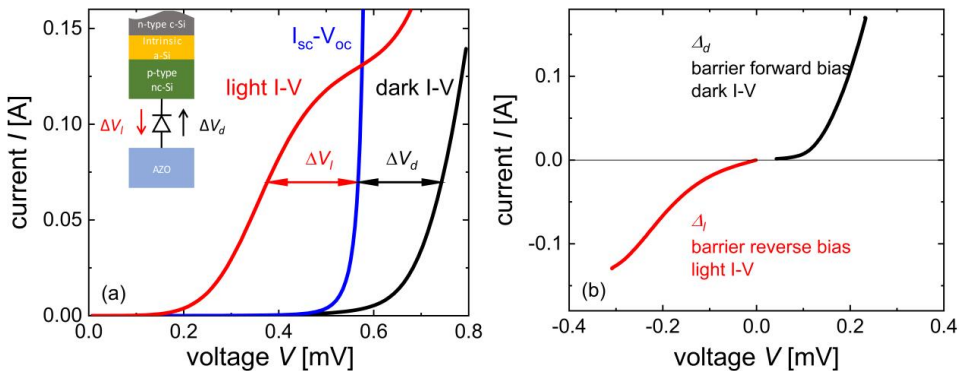
Fig. 7.4. Contact barrier between p-type nc-Si and AZO, (a) dark I-V, light I-V, and I_{sc}-V_{oc} curves with the interface schematic illustrated as the inset; (b) I-ΔV curve for the voltage offset of ΔV_l for the light I-V to I_{sc}-V_{oc} and ΔV_d for the dark I-V to I_{sc}-V_{oc} at the same current.

current. In the cell under consideration with p-type nc-Si / AZO contact the ΔV does not linearly depend on current which is dominated by the barrier. Therefore, the I-ΔV dependence is attributed to the I-V characteristic of the barrier shown in Fig. 7.4(b). The I-V characteristics of the barrier is nonlinear and non-symmetric with considerably higher resistance in the "light" branch. The I-V characteristic of the barrier is attributed to a poor-quality diode with low breakdown voltage. The diode is blocking for photocurrent and suppressing extraction of holes, therefore, heavily reduces *FF*.

7.3 Optimization on contact barrier between AZO and p-type nc-Si

The contact barrier at the interface between AZO and p-type nc-Si can be to the large extent attributed to poor extraction of photogenerated holes. Optimization on barrier has been addressed in this section with a series of experiments including variation of p-type nc-Si with doping, thickness, and seed layer and variation of AZO with doping and sputtering temperature.

7.3.1 Doping level, thickness, and seed layer in p-type nc-Si for contact barrier

Insufficient doping in the p-type nc-Si layer can be a reason for the barrier formation [73]. Considering it the flow rate ratio r_{TMB} for p-type nc-Si layer deposition was increased from 0.5 to 1 for the layer thickness of 10 and 20 nm, respectively. Influence of doping variation on the light J-V curves is presented in Fig. 7.5. For cells with 10- or 20-nm-thick p-type nc-Si layer, increase in doping of p-type nc-Si leads to noticeable improvement of J-V characteristics. Even though the J-V characteristics are not totally recovered, the application of p-type nc-Si with higher doping is beneficial for the cell performance.
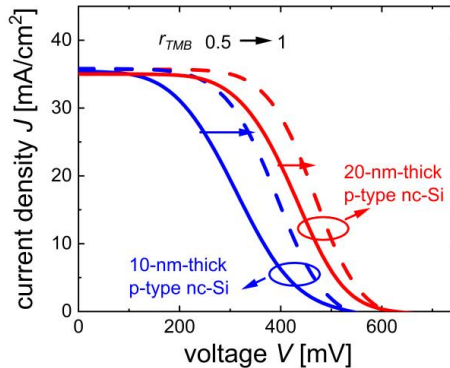
Fig. 7.5. Light J-V curves for the SHJ solar cells with 10- and 20-nm-thick p-type nc-Si layers with r_{TMB} of 0.5 and 1, respectively. The AZO in cells were sputtered with 2 wt.% target at RT.

As suggested in [92] insufficient conductivity of p-type nc-Si layer can lead to the formation of Schottky barrier at the p-type nc-Si / AZO interface. Conductivity in doped thin-film Si layers is strongly crystallinity dependent which is related to the increase in doping efficiency when crystalline volume fraction increases. The crystallinity in nc-Si films is thickness dependent as well, especially in the first 50 nm– the range where all doped layers in SHJ solar cells are prepared [91, 92]. To monitor the conductivity the p-type nc-Si layer was prepared on the glass substrate with the intrinsic a-Si layer underneath. The lateral conductivity is in the order of 10^{-2} S/cm for the p-type nc-Si layer thickness of 35 nm which corresponds to the thickness of approximately 20 nm on textured wafer.

Thus, the thickness of the p-type nc-Si layer was varied from 5 nm to 40 nm in SHJ solar cells as shown in Fig. 7.6(a). Compared to the initial thickness of 20 nm, decrease of p-type nc-Si layer thickness leads to the reduction of V_{oc} most likely due to the insufficient band bending in the p-n junction region. The s-shape in the J-V curves are reduced as well which may due to the increased fraction of amorphous phase in the film. This situation improves the contact between Si layer and AZO, which is consistent with the results for the cells with p-type a-Si layer. However, the cell with 40-nm-thick p-type nc-Si shows even more severe s-shaped J-V characteristic largely resulting from the high resistance of the thick layer. As an alternative approach to achieve higher crystallinity in p-type Si, a seed layer was introduced prior to the p-type nc-Si layer deposition. The seed layer was prepared with the same deposition parameter to the p-type nc-Si layer except for the doping gas and 100 s deposition time. The SHJ solar cell with the seed layer shows improvement in the shape of J-V characteristic and higher V_{oc} compared to reference cell without seed layer. Experiment with the seed layer indicates that the growth surface is critical to improve crystallinity in p-type nc-Si layer and contact performance with AZO. This observation is in line with Ref. [111] where a Si-oxide-treatment on the intrinsic a-Si is shown to be beneficial for
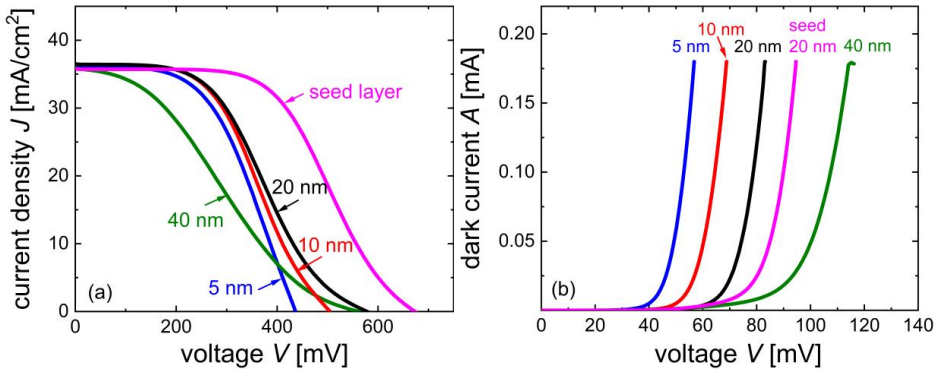
Fig. 7.6. Light J-V curves (a) and dark J-V curves (b) for the SHJ solar cells with seed layer and varied p-type nc-Si layer thickness of 5 nm, 10 nm, 20 nm, and 40 nm, respectively. The AZO films were sputtered at RT with 1 wt.% target.

crystallinity in p-type nc-Si layers. The dark J-V curves shown in Fig. 7.6(b) presents that the reverse saturation current decreased with the increase of the p-type nc-Si layer thickness.

Summarizing the experiments on the doping and thickness or seed layer for p-type nc-Si layers in SHJ solar cells, it can be concluded that higher doping and early nucleation of nc-Si layer are beneficial for the reduction of the series resistance in p-type nc-Si layer and for the contact resistance between the p-type nc-Si and AZO.

7.3.2 Sputtering temperatures and doping concentrations in AZO for contact barrier

The sputtering temperature and target doping concentration have influence on the properties of AZO films which in turn affect the contact at the interface with p-type nc-Si layer. Therefore, the AZO layers prepared with varied sputtering temperatures and doping concentration were applied in SHJ solar cells to test their contribution to solving the s-shaped light J-V problems.

In order to examine the effect of AZO sputtering temperature on the s-shaped J-V curve, a series of SHJ cells were prepared with 1 wt.% AZO sputtered at RT, 150°C, and 200°C, respectively. The J-V curves are presented in Fig. 7.7. The cells with AZO sputtered RT, 150°C, and 200°C exhibit pronounced s-shape J-V curves. There is no systematic improvement observed in the J-V characteristics. This is consistent with the slight influence of the sputtering temperature on the properties of AZO films on glass substrate shown in section 4.2.

Insufficient AZO doping can be another limitation for the formation of proper contact with p-type nc-Si. Therefore, the AZO films sputtered with 2 wt.% target were applied in the SHJ solar cells with the 10- or 20-nm-thick p-type nc-Si layers. Corresponding J-V curves are presented in Fig. 7.8. For both SHJ solar cells with 10- and 20 nm-thick p-type nc-Si, the AZO films sputtered with 2 wt.% target, thus with higher carrier concentration, have slight influence on J-V
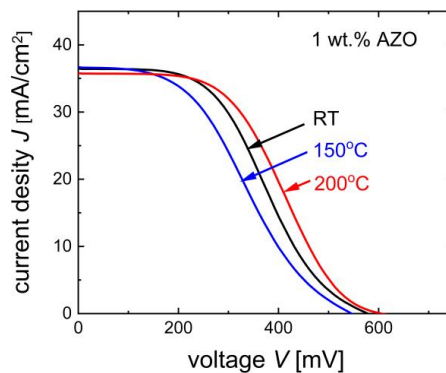
Fig. 7.7. Light J-V curves for SHJ solar cells with 1 wt.% AZO sputtered at the substrate temperature of RT, 150°C, and 200°C, respectively.

characteristic of the solar cells. The results indicate that doping concentration in AZO films is not the dominating limitation for the carrier collection at the interface between p-type nc-Si and AZO.
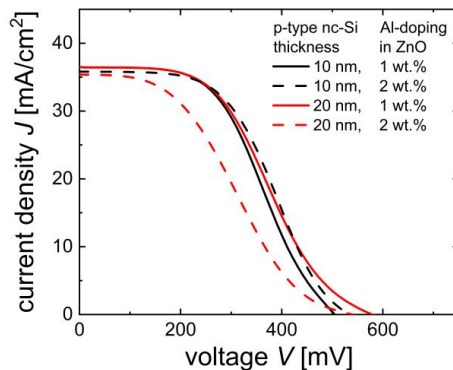
Fig. 7.8. Light J-V curves for SHJ solar cells with AZO sputtered with 1 wt.% and 2 wt.% target at RT and p-type nc-Si with the thickness of 10 nm and 20 nm.

Besides the material properties, the layer preparation order may also influence the interface between AZO and p-type nc-Si. In order to examine process related effects, a thin-film Si solar cell was prepared with the reversed preparation order of p-type μc-Si and AZO compared to the SHJ solar cells [112, 113]. Comparison of the J-V curves of SHJ solar cell with p-type nc-Si / AZO contact and thin-film Si solar cell with AZO / p-type μc-Si contact is presented in Fig. 7.9. Since the cells are almost twice different in current density, the J-V curves of SHJ cell were measured at different illumination intensities. Severe barrier is affecting the J-V characteristics of SHJ solar cell, and the thin-film Si cell with reversed orders of AZO/p-type layer shows proper J-V characteristic. From the comparison of these two cells, it can be concluded that the growth surface
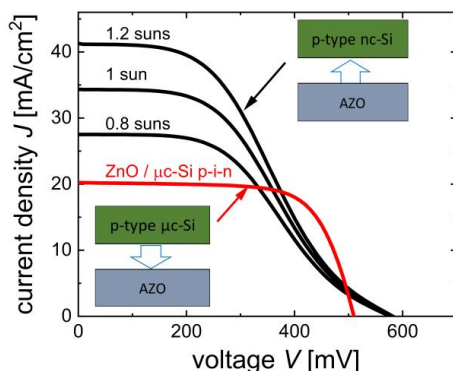
Fig. 7.9. Light J-V curves for μc-Si:H thin-film solar cell and SHJ solar cell with reverse deposition orders of AZO and p-type Si layer.

for p-type nc-Si layer plays an important role in the contact properties between p-type nc-Si layer and AZO speculatively related to the influence of the AZO sputtering process.

7.4 Short summary

In our work, Si layer combinations of (1) n-type a-Si / p-type a-Si, (2) n-type nc-Si / p-type a-Si, (3) n-type a-Si / p-type nc-Si, and (4) n-type nc-Si / p-type nc-Si were implemented in rear emitter SHJ solar cells on commercial textured n-type Czochralski Si wafers. The contact properties of AZO with varied Si layers were investigated in SHJ solar cells by varying the Si layer combinations. Among these four kinds of cells, pronounced s-shaped light J-V curves is observed for SHJ solar cells with p-type nc-Si layer. The cells with p-type a-Si layer show proper J-V characteristic. The s-shaped J-V characteristic is either due to the properties of the p-type nc-Si layer itself or due to the contact barrier at the interface with AZO.

Firstly, the reason for the s-shaped J-V curve was identified by measuring the J-V curves of the cells with introducing a p-type a-Si layer prior to or after the deposition of p-type nc-Si layer. In this way, the p-type nc-Si layers were included in both cells, while the interfaces with AZO were different. The J-V characteristics of these two cells show that the s-shape in J-V curve is to large extent attributed to the contact barrier at the interface between AZO and p-type nc-Si layer.

Then, the properties of the barrier were analyzed. The carrier collection barrier at the rear of the device is thermally activated. The voltage offsets between light I-V and I_{sc}-V_{oc} curves or dark I-V and I_{sc}-V_{oc} curves at the same current level have be extracted for the electrical property analysis of the barrier. The results shown typical asymmetrical non-linear I-V characteristic opposing holes collection.

Deposition parameters for the p-type nc-Si layer and AZO have been varied for proper contact at the interface. Increase of the doping in p-type nc-Si reduces the contact barrier. Variation of the thickness of p-type nc-Si and introducing of a seed layer show that the growth surface for the p-type nc-Si layer is crucial to its contact with AZO. However, the sputtering temperature and doping concentration in AZO film do not contribute to reducing the contact barrier. By comparing the deposition order of the p-type nc-Si and AZO to μc-Si:H thin-film cell, it can be concluded that the fabrication process or the growth surface, also affects the contact properties at the interface.

Further optimizations to the barrier at the interface between p-type nc-Si and AZO will be focused on the highly doped p-type nc-Si layer development and on the growth surface treatment for p-type nc-Si layer.

Chapter 8 Loss analysis in SHJ solar cells

This chapter describes loss analysis for the photovoltaic parameters of silicon heterojunction solar cells which is critical for cell optimization. The losses in V_{oc}, FF, R_s, and J_{sc} have been analyzed in detail. The first section introduces the theoretical limitation for the SHJ solar cells studied in this work. The second section describes the variation of V_{oc} during cell fabricating process. Implied open circuit voltage iV_{oc} has been measured after the Si layer deposition, AZO sputtering, annealing, and AZO removal from the QSSPC measurements. Open circuit voltage V_{oc} was measured with solar simulator from the I-V characterization and Suns-V_{oc} apparatus. The difference between iV_{oc} and V_{oc} values are studied to investigate the V_{oc} loss during cell fabrication process. The third section describes the fill factor losses by comparing experimental data to the theoretical limit. The implied fill factor iFF, pseudo fill factor (pFF) acquired from Suns-V_{oc} and I-V characterization, and the cell fill factor FF acquired from I-V characterization are compared to study the FF loss in the solar cells. The fourth section focuses on the series resistance analysis. The contributions from different layers and contacts at the interface were identified in this section. The fifth section describes the loss analysis in the short circuit current density of the solar cells with QE response and reflection spectra of the solar cells. This chapter on loss analysis is of importance to instruct future work.

8.1 Theoretical limits for the SHJ solar cells

Considering the loss in SHJ solar cells, comprehensive analysis of losses in a solar cell is performed with respect to the theoretical limits for specific parameters. Shockley and Queisser [114] presented the detailed balance limit efficiency for the p-n junction solar cells considering merely the radiative recombination and assuming the sun as the blackbody with temperature of 6000 K. The maximum efficiency of 30 % was calculated for Si solar cell with the band gap of 1.1 eV. To improve the calculation model, researchers took the Coulomb-enhanced Auger recombination which dominates the intrinsic loss mechanism or parasitic free carrier absorption (FCA) into consideration [115 - 118]. Moreover, the parameters to calculate the theoretical limit have been improved for the quantitative description of the intrinsic recombination properties

including the radiative and Auger recombination and other parameters relevant for the limit efficiency calculation including new reference solar spectrum, updated self-consistent optical parameters of intrinsic Si, new parameters for FCA, and the effect of band gap narrowing et al. [20, 119-121]. Based on the state-of-the-art modeling parameters and not considering the surface or defect assisted (Shockley-Read-Hall, SRH) recombination, Richter *et al*. calculated the limiting efficiency for the single junction solar cells under 1-sun illumination AM 1.5G at 25°C on the assumption of a perfect Lambertian light trapping scheme [20, 122]. The highest theoretical efficiency 29.4 % was predicted for a solar cell with 110-μm-thick undoped c-Si wafer. The related photovoltaic parameters are $V_{oc} = 761$ mV, $J_{sc} = 43.3$ mA/cm^2, and $FF = 89.3$ % [17].

For the cells prepared in this work, 170-μm-thick n-type textured crystalline Si wafers were used to fabricated SHJ solar cells. Applying the wafer thickness of 170-μm and the resistivity of approximately 3 Ω·cm^2 into the theoretical limitation calculation as shown in [20], the approximately parameters are $\eta = 29.1$ %, $V_{oc} = 752$ mV, $J_{sc} = 43.7$ mA/cm^2, and $FF = 88.6$ %. These theoretical limit values are applied in the following loss analysis for the cell photovoltaic parameters.

8.2 Loss analysis for the open circuit voltage of SHJ solar cells

To analyze the open circuit voltage loss, either iV_{oc} or V_{oc} values were measured after each cell fabrication step for both 19 mm ×19 mm size and M2 size cells. The iV_{oc} values were measured with QSSPC after Si layer deposition, after the AZO sputtering, after annealing, and after the AZO removal as shown in black columns in Fig. 8.1. The V_{oc} values were measured either with Suns-V$_{oc}$ as shown in red columns or sun simulator as shown in green column. The theoretical limit is shown in blue column. For the 19 mm ×19 mm size cells, since they are fabricated in the 78 mm × 78 mm size wafers, the sensor region of QSSPC measurement is covered with the combination region of the AZO covered area from the solar cells and the non-AZO covered area from the surrounding area as shown in section 6.2. To improve the accuracy of the passivation evaluation after AZO sputtering for small cells, the samples with full area covered AZO on 78 mm × 78 mm size wafer were prepared with the same deposition parameters to the solar cells for the QSSPC measurement.

In Fig. 8.1 the steps of cells treatment are labeled on x-axis. Fig. 8.1(a) shows the iV_{oc} or V_{oc} variations for 19 mm ×19 mm cells in the order of iV_{oc} measured after Si layer deposition, AZO sputtering, annealing, and AZO removal for the cell precursors with full area covered AZO, the iV_{oc} after Si layer deposition for the cell precursor with patterned AZO, the V_{oc} measured from Suns-V$_{oc}$ after patterned AZO sputtering, annealing, and metallization, and the V_{oc} measured from I-V after metallization. Fig. 8.1(b) shows the iV_{oc} or V_{oc} variations for M2 cell in the order of iV_{oc} measured after Si layer deposition, AZO sputtering, and annealing, the V_{oc} measured from Suns-V$_{oc}$ after AZO sputtering, annealing, and metallization, and the V_{oc} measured from I-V after metallization.
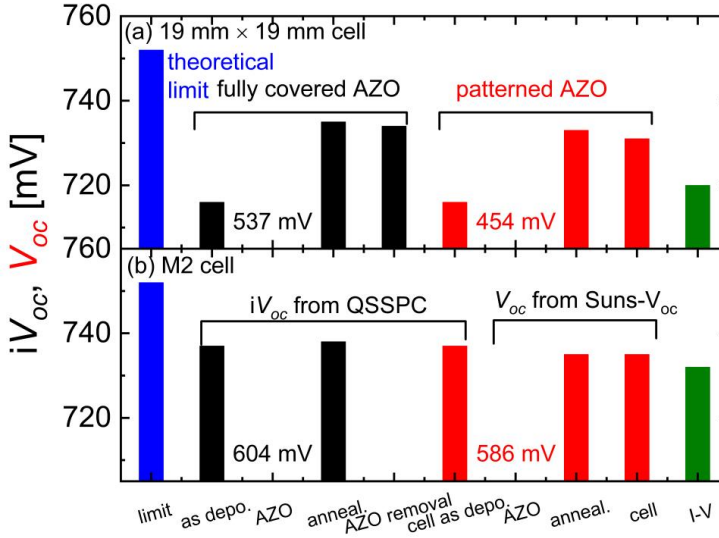
Fig. 8.1. Open circuit voltage summary: the theoretical limit V_{oc} of solar cell, iV_{oc} variation after Si layer deposition, AZO sputtering, annealing, and AZO removal, and the V_{oc} variation after AZO sputtering, annealing, and metallization in the SHJ solar cells with the cell area of (a) 19 m × 19 mm, (b) M2.

Compared to the V_{oc} theoretical limit, the V_{oc} values achieved from I-V characterization are approximately 30 mV and 20 mV lower for the cells with the sizes of 19 mm × 19 mm and M2, respectively. This difference to large extent is attributed to the surface or SRH recombination, and the non-ideal carrier selectivity.

For 19 mm × 19 mm cells, AZO sputtering reduces the iV_{oc} of cell precursor with fully covered AZO to 537 mV which is consistent with the lifetime degradation as discussed in chapter 6. The iV_{oc} values are recovered after annealing. The iV_{oc} measured after the subsequent AZO removal proves that the damage on the passivation of the Si layers from the AZO sputtering has been totally recovered by the annealing. The cell precursor used for patterned AZO shows the same iV_{oc} value after Si layer deposition as the cell precursor with full area covered AZO. In this way, these two samples with full area covered AZO and patterned AZO are comparable. After AZO sputtering, the Suns-V_{oc} measurement has been used to monitor the V_{oc} variation. Similar trend to iV_{oc} has been observed V_{oc} decreases after AZO sputtering and recovers after annealing. However, there is a approximately 15 mV V_{oc} decrease from the iV_{oc} value after annealing to the ready cell I-V characterization. The difference is largely attributed to the sample geometry with high ratio of perimeter to area resulting in high recombination in the perimeter region [123], the measurement contact structure for small cell, and non-ideal carrier selectivity of the selective contact stacks [94, 95]. The Suns-V_{oc} measurements after cell precursor annealing and metallization show the similar

V_{oc} values to the iV_{oc} value after annealing. The V_{oc} difference between the results acquired from Suns-V_{oc} and I-V is still not clear.

For the cells fabricated on M2 size wafers, high iV_{oc} values achieved after the Si layer deposition are reduced after the AZO sputtering and recovered after annealing. There is also slight V_{oc} decrease of approximately 5 mV from the iV_{oc} value after annealing to the V_{oc} value from the I-V characterization which is subjected for further investigation.

The SHJ solar cells on M2 size wafers show less V_{oc} loss respects to the iV_{oc} after annealing, which is supposingly related to the lower ratio of perimeter to area resulting in lower recombination in the perimeter region compared to the 19 mm × 19 mm solar cells in the 78 mm × 78 mm wafers and better carrier selective contact. The M2 size wafers should be the major cell substrate for the further optimization work combined with the developed M2 size cell fabrication chain.

8.3 Loss analysis for the fill factor of SHJ solar cells

Fill factor is another key parameter for solar cell performance and shows the power generation capabilities. In this section, two methods of loss analysis on *FF* were used: the first one is based on a two-diode model as discussed in Ref. [124], and the second one is based on the comparison of measured parameters like i*FF*, p*FF*, and *FF* with theoretical limit.
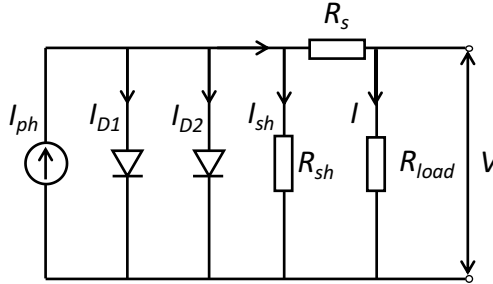
Fig. 8.2. Equivalent circuit for the two-diode model used for *FF* loss analysis.

The *FF* is limited by the carrier recombination and the ohmic resistances of series resistance R_s and shunt resistance R_{sh}. In the calculation, a two-diode solar cell model schematic illustrated in Fig. 8.2 was used to account for the recombination and resistance influence with the parameters indicated as well. There are two saturation current densities J_{01} and J_{02} for the two diodes, and series and shunt resistance of R_s and R_{sh} considered in the model. For the *FF* loss resulting from the carrier recombination, there are two major contributors. One is the recombination in the quasi-neutral bulk and at the two cell surfaces which set the practical upper limit for the fill factor of crystalline Si solar cells which is related to J_{01} [125]. Another one is the recombination in the space

charge region or at the edge or the high defect density localized regions [126-128] which further decreased the *FF* which related to J_{02}.

With the two-diode model, the *FF* was analyzed by the calculation with the formulas Eq. 8.1-8.9 and the input parameters of V_{oc}, J_{sc}, *FF*, η, V_{mp} (voltage at maximum power point), J_{mp} (current density at maximum power point), R_s and R_{sh} [124]. The following parameters are acquired: FF_{J01} determined without considering R_s, R_{sh} and J_{02}, FF_0 determined without considering R_s and R_{sh}, ΔFF_{Rs} defined as the *FF* loss from R_s, ΔFF_{Rsh} defined as the *FF* loss from R_{sh}, ΔFF_{J02} defined as the *FF* loss due to J_{02} related recombination, and p*FF* determined without considering the R_s. The difference between p*FF* and *FF* is related to *FF* loss due to R_s, and the difference between FF_0 and p*FF* is related to *FF* loss due to R_{sh}. The input and output parameters are summarized in Table 8.1 and the *FF* loss related to the recombination and ohmic resistance are presented in Fig. 8.3.

$$FF_{J01} = \frac{kT_{temp.}}{qV_{oc}} \cdot \frac{(W[z]-1)^2 \exp(W[z]-1)}{\exp(qV_{oc}/kT_{temp.}-1)}, z = \exp[1 + qV_{oc}/kT_{temp.}], \quad (8.1)$$

$$FF_0 = FF + \frac{J_{mpp}^2 R_s}{V_{oc}J_{sc}} + \frac{(V_{mpp}+J_{mpp}R_s)^2}{R_{sh}V_{oc}J_{sc}}, \quad (8.2)$$

$$\Delta FF_{Rs} = \frac{J_{mpp}^2 R_s}{V_{oc}J_{sc}}, \quad (8.3)$$

$$\Delta FF_{Rsh} = \frac{(V_{mpp}+J_{mpp}R_s)^2}{R_{sh}V_{oc}J_{sc}}, \quad (8.4)$$

$$\Delta FF_{J02} = FF_{J01} - FF_0, \quad (8.5)$$

Table. 8.1. Input parameters of V_{oc}, J_{sc}, *FF*, η, V_{mp}, J_{mp}, R_s and R_{sh} acquired from the J-V and J_{sc}-V_{oc} measurement for the *FF* loss analysis and the output parameters for the *FF* loss components.

input			output		
Parameter	Value	unit	Parameter	Value	unit
V_{oc}	720.3	mV	FF_{J01}	84.89	%
J_{sc}	39.07	mA/cm^2	FF_0	81.05	%
FF	75.45	%	ΔFF_{Rs}	5.50	%
η	21.23	%	ΔFF_{Rsh}	0.10	%
V_{mpp}	586.1	mV	ΔFF_{J02}	3.84	%
J_{mpp}	36.23	mA/cm^2	*pFF*	80.95	%
R_s	1.18	Ω•cm^2			
R_{sh}	7.39E+03	Ω•cm^2			

$$FF_{J_{01}} = pFF + \Delta FF_{R_{sh}} + FF_{J_{02}}, \tag{8.6}$$

$$FF_0 = pFF + \Delta FF_{R_{sh}}, \tag{8.7}$$

$$FF = FF_{J_{01}} - \Delta FF_{J_{02}} - \Delta FF_{R_s} - \Delta FF_{R_{sh}}, \tag{8.8}$$

$$FF = pFF - \Delta FF_{R_s}, \tag{8.9}$$

in which the $W[z]$ is the Lambert W-function.
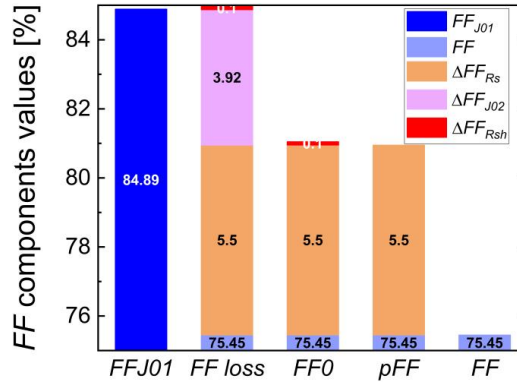
Fig. 8.3. *FF* distribution and *FF* losses related to R_s, R_{sh}, J_{01} and J_{02}.

According to the calculations, the main *FF* losses are from R_s and J_{02} related recombination. The *FF* loss from the J_{02} related recombination mainly depends on the nature of the trap state, the width of the depletion region, and the lifetime of both electron and holes, metal contact recombination, meaning the interface defect states [124].

Using the second approach for the loss analysis - comparison of i*FF*, p*FF*, and *FF* to the theoretical limit - the following losses were identified. The *FF* component analysis is presented in Fig. 8.4. The ΔFF_{R_s} loss of 4.9 % from p*FF* to *FF* is due to the high series resistance from the non-optimal metallization. A loss of 3.2 % in *FF* from i*FF* of 83.5 % to p*FF* of 80.3 % acquired from I_{sc}-V_{oc} measurement is due to the carrier selectivity of the selective contact stacks and the shunt resistance which, however, has negligible effect due to typically high shunt resistance. The i*FF* acquired from QSSPC measurement represents the recombination limited *FF* value resulting from the J_{01} and J_{02} related recombination. The measured i*FF* is physical equivalent to the FF_0 from the two-diode model calculation. It can be seen that there are differences between these two characterization methods for the *FF* loss analysis. The reason can be that the QSSPC measurement is non-contact technique, while for the I-V measurement the selective contact plays a role during the carrier extracting which affects the *FF*. Compared to the theoretical limit of *FF* of 88.6 %,
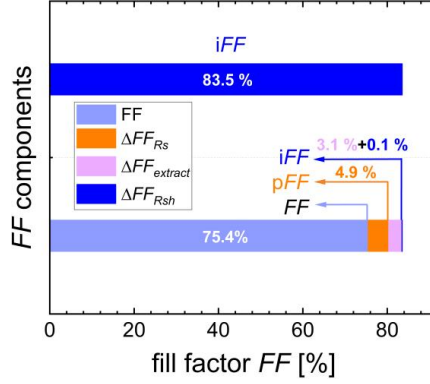
Fig. 8.4. i*FF* and *FF* components related to R_s, R_{sh}, and carrier extraction with the results acquired from QSSPC, I-V, and I_{sc}-V_{oc} measurements.

there is total loss of 13.2 % as for the solar cells. The *FF* loss of 4.9 % is from the R_s, and the *FF* loss of 3.1 % is from the imperfect carrier selectivity of the contacts.

From the two-diode model fitting as shown in Fig. 8.5, the J_{01} = 24.5 fA/cm^2 and J_{02} = 70 nA/cm^2 are calculated with the equivalent circuit calculator form the PV lighthouse. Thus, the current related to the J_{01} and J_{02} recombination is calculated as:

$$J_{loss,J_i} = J_i \exp(qV_{oc}/n_i\,kT - 1). \tag{8.10}$$
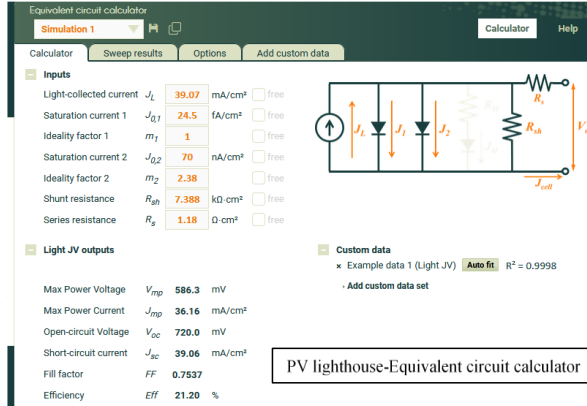
Fig. 8.5. Two-diode model fitting for the J_{01} and J_{02} with equivalent circuit calculator from the PV lighthouse.

in which i is 1 or 2. With the calculation, $J_{loss,J01}$ = 11.23 mA/cm^2 and $J_{loss,J02}$ = 3.11 mA/cm^2. The current loss due to the J_{02} related recombination is limited by the material properties and the cell surface passivation. The current loss related to the J_{02} related recombination is mainly due to the recombination in the junction region.

In conclusion, the series resistance and the J_{02} related recombination play big roles in the *FF* loss. The analysis related the series resistance will be addressed in detail in the section 8.4.

8.4 Loss analysis for the series resistance of SHJ solar cells

Series resistance is the dominant factor of *FF* loss, therefore, a detailed analysis of series resistance components has been performed. The series resistance is the sum of the resistances from each layer and the contact resistances at the contact interfaces among the layers as shown in Eq. 8.11. Referred to the cell structure, the schematic illustration of each resistance component is shown in Fig. 8.6. The resistivities of the films were acquired by conductivity measurement or Hall measurement. The contact resistances at the interfaces were obtained by the transfer length method (TLM). The front i/n stack and rear i/p stack are considered as a whole, respectively. Among all the interfaces, the contact interfaces between AZO and Si layers are the most critical. The series resistance components and the calculation are summarized as follows:

$$R_{s,total} = R_s^{front\ finger} + R_s^{front\ AZO/Ag} + R_s^{front\ AZO} + R_s^{AZO/front\ (i/n)} + R_s^{front\ (i/n)} +$$
$$R_s^{front\ (i/n)/wafer} + R_s^{wafer} + R_s^{wafer/rear\ (i/p)} + R_s^{rear\ (i/p)} + R_s^{rear\ (i/p)/AZO} + R_s^{rear\ AZO} +$$
$$R_s^{Ag/AZO} + R_s^{rear\ Ag}. \tag{8.11}$$
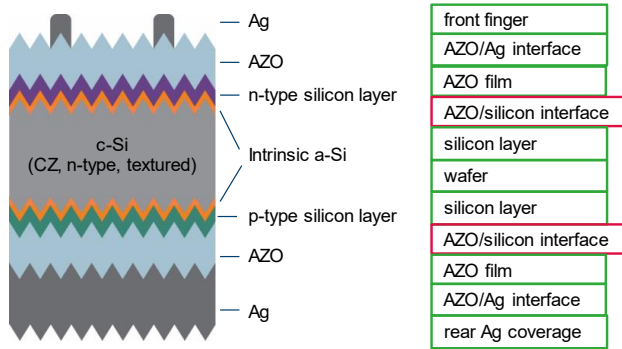
Fig. 8.6. Schematic illustration of each component contributing to the series resistance in SHJ solar cells.

97

The SHJ solar cells were fabricated with the same AZO films at the front and rear sides. In the TLM measurement, the contact resistances at the interfaces of AZO/front (i/n) and front (i/n)/wafer were measured as a whole as $R_s^{AZO/(i/n)/wafer}$ due to the low resistivity of the c-Si wafer. The situation is the same at rear side with the $R_s^{wafer/(i/p)/AZO}$ describing the contact resistances at the interfaces of wafer/rear (i/p) and rear (i/p)/AZO at the rear side. In this way, the formula is rewritten as

$$R_{s,total} = R_s^{front\,finger} + 2R_s^{AZO} + R_s^{front\,(i/n)} + R_s^{wafer} + R_s^{rear\,(i/p)} + +R_s^{rear\,Ag} +$$
$$2R_s^{AZO/Ag} + R_s^{AZO/(i/n)/wafer} + R_s^{wafer/rear\,(i/p)/AZO}, \tag{8.12}$$

where the items in the first line of the formula are the resistances form the layers and the items in the second line of the formula are the contact resistances at the interfaces. Moreover, it is widely believed that the $R_s^{AZO/front\,(i/n)}$ and $R_s^{(i/p)/AZO}$ dominate in the combined contact resistances of $R_s^{AZO/(i/n)/wafer}$ and $R_s^{wafer/(i/p)/AZO}$, respectively. Thus, the $R_s^{AZO/front\,(i/n)}$ and $R_s^{(i/p)/AZO}$ are used in the following description.

The calculation process for each component is shown as follows:

(1) $R_s^{front\,finger}$, $R_s^{rear\,Ag}$, and R_s^{AZO}

The front finger design is shown in Fig. 3.4(b) in chapter 3. The cell aperture area is 19 mm × 19 mm with 10 fingers and the busbar is surrounding the aperture area. The finger width is 50-60 μm and the busbar width is 1 mm. The resistivity of the silver paste is 2.0×10^{-4} Ω·cm and the height of the finger and busbar is 16 μm.

Considering the cell design with only fingers covering the cell aperture area and the calculation requirement with the "Grid" module from PV lighthouse, a finger was taken out and used as a busbar to fit the "H" pattern as shown in Fig. 8.7. The parameters used for the rear contact are the default values since the full-area-covered Ag electrode was used in our case and the rear Ag resistance is not considered in this case. The calculation result of $R_s^{front\,finger}$=1.65 Ω·cm^2.

At the rear side of the solar cell, the Ag covers all the cell area. The same height of 16 μm with the finger was used for the calculation. Thus, the $R_s^{rear\,Ag}$ is calculated as

$$R_s^{rear\,Ag} = 2.0 \times 10^{-4} \times 16 \times 10^{-4} = 3.2 \times 10^{-7}\ \Omega \cdot cm^2.$$

For the bulk resistance of the AZO film, the resistivity of the AZO film is 1.2×10^{-3} Ω·cm, the thickness is approximately 80 nm, and the path length for current collection is 1 mm, thus the R_s^{AZO} is calculated as

$$R_s^{AZO} = 1.2 \times 10^{-3} \times (80 \times 10^{-7} + 0.1\ ) = 1.2 \times 10^{-4}\ \Omega \cdot cm^2.$$

(2) $R_s^{front\,(i/n)}$, $R_s^{rear\,(i/p)}$, and R_s^{wafer}

The resistivity of the n-type, p-type, intrinsic Si layers, and wafer are 1.2, 2.3×10^4, 1.5×10^5 (light) and 3 $\Omega{\cdot}cm^2$, respectively. The thicknesses of the n-type, p-type, intrinsic Si layers, and the wafer are 20 nm, 10 nm, 5 nm and 170 μm, respectively. Thus, the resistances for each layer are calculated as

$$R_s^{front\ n} = 1.2 \ \times 20 \times 10^{-7} = 2.4 \times 10^{-6} \ \Omega \cdot cm^2 \,,$$

$$R_s^{rear\ p} = 2.3 \ \times 10^4 \times 10 \times 10^{-7} = 2.3 \times 10^{-2} \ \Omega \cdot cm^2 \,,$$

$$R_s^{i} = 1.5 \ \times 10^5 \times 5 \times 10^{-7} = 7.5 \times 10^{-2} \ \Omega \cdot cm^2,$$

$$R_s^{wafer} = 3 \ \times 170 \times 10^{-4} = 5.1 \times 10^{-2} \ \Omega \cdot cm^2 \,.$$

(3) $R_s^{AZO/Ag}$, $R_s^{AZO/front(i/n)}$, and $R_s^{rear\ (i/p)/AZO}$

Fig. 8.7. Front finger series resistance calculation with the "Grid" module from PV lighthouse.

The contact resistances at the interfaces in SHJ solar cell are measured with TLM structure prepared on the wafers identical to the ones used for cells. The contact resistance at the interface of Ag and AZO is measured with the structure schematic illustrated in the Fig. 3.6(b). The $R_s^{AZO/Ag}$ is 4.2×10^{-3} $\Omega \cdot cm^2$.

The contact resistance measured with the structure schematic illustrated in Fig. 3.6(c) is a combination of the contact resistances at the interface of AZO and Si layer and the interface of Si layer and wafer. Meanwhile, the wafer base has a lower resistivity due to the high thickness compared to the Si layers. The $R_s^{front(i/n)/AZO}$ is 6.7×10^{-2} $\Omega \cdot cm^2$.

Due to the n-type base, the interface between p-type a-Si and wafer is in the p-n junction region, thus s-shaped I-V curves were observed in the TLM measurement from which the contact resistance cannot be extracted. Thus, a p-type textured wafer was used to test the contact resistance with the similar structure shown in Fig. 3.6 (c). The $R_s^{rear\,(i/p)/AZO}$ is approximately 0.3 $\Omega \cdot cm^2$

With the resistance calculation for each item in the bulk and at the interface, the resistance components contributing to the total series resistance are listed in Table 8.2. The total series resistance of the solar cell from the calculation is 2.25 $\Omega \cdot cm^2$, which is only 1.3 % difference from the measured R_s of 2.22 $\Omega \cdot cm^2$ from the I-V characterization. The data is presented in form of pie diagrams in Fig. 8.8 as well. All series resistance components are shown in Fig. 8.8(a). The highest series resistance component is from the front finger. The second and the third high resistances components are contact resistance between the AZO and i/p Si layer stack and the bulk resistance of the i/p stack itself. Fig. 8.8(b) shows that the 83.3 % of the cell series resistance is from the bulk resistance of the layers in solar cells, and 16.7 % of the cell series resistance is from the resistances at interfaces. Fig. 8.8(c) shows the resistance distribution in the bulk. The major resistance from the layers is front finger resistance, then the resistances of i/p stack and i/n stack contributed to the

Table. 8.2. Distribution of each resistance components contributing to the series resistance of the SHJ solar cells.

Parameter bulk	resistance $\Omega \cdot cm^2$	Parameter interface	resistance $\Omega \cdot cm^2$
front finger	1.65	AZO/Ag	8.4E-3
AZO	1.2E-4	AZO/front (i/n)	6.7E-2
front (i/n)	7.5E-2	rear (i/p)/AZO	0.30
wafer	5.1E-2		
rear (i/p)	9.8E-2		
rear Ag	3.2E-7		
sum	1.87	sum	0.38

second and third high values for the total bulk resistance. Fig. 8.8(d) shows the resistance distribution at the interfaces. The resistance at the interface between the AZO and i/p Si layer stack is 79.9 % of the total contact resistance at the interface. While the resistance at the interface of AZO and i/n Si layer stack is 17.9 % of the total contact resistance.

In conclusion, the high series resistance of the solar cells is mainly from the high front finger resistance, high contact resistance at the interface of AZO and i/p Si layer stack, and the resistance of the i/p stack. Among these three factors, high resistance of the front finger contributes the most to the cell series resistance. In the view of bulk resistance, aside for the front finger resistance, the resistances of rear i/p and front i/n Si layer stacks are the following factors to be considered for R_s optimization. In the view of the interface resistance, aside for the resistance at the interface of AZO rear i/p, the interface between AZO and front i/n Si layer stack is the following factor to be considered for the R_s optimization. The resistance of the AZO, Ag, and their contact is low enough to be neglected.
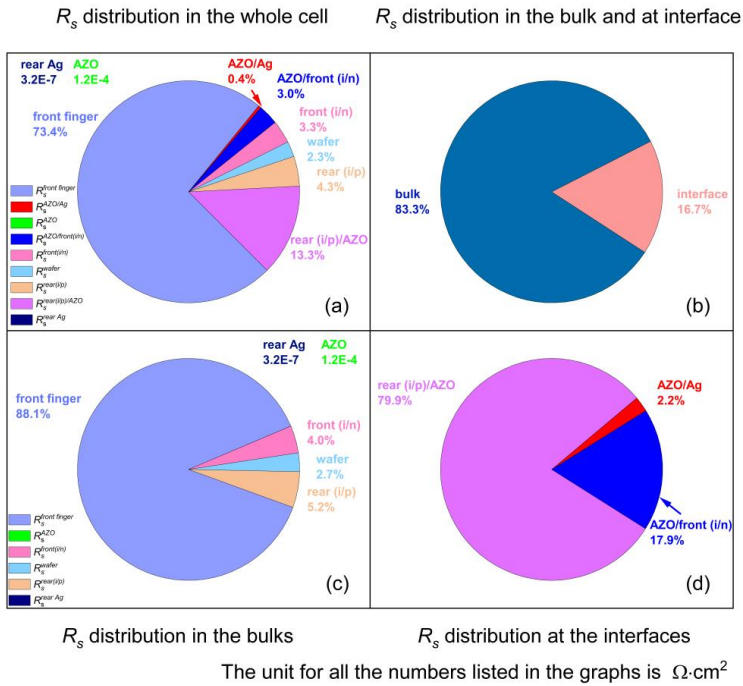
Fig. 8.8. Schematic illustration of the series resistance distribution in SHJ solar cells: (a) each series resistance component in solar cells; (b) series resistance distribution in the bulk and at the interface; (c) resistance distribution of each layer; (d) resistance distribution at the interface between layers.

8.5 Loss analysis for the short circuit current density of SHJ solar cells

To investigate the optical loss of the SHJ solar cells, the short circuit current density loss from the reflection and absorption of each component were identified and quantified. The current loss analysis is based on the *QE* characterization. Both the *QE* response and the reflection spectra were analyzed in the wavelength region 300-1200 nm. The short circuit current density related to the response of each item X to the AM1.5G light spectrum are calculated from formula as follows:

$$J_{sc} = \int qX\emptyset_{inc}d\lambda = \int \frac{q\cdot\lambda}{hc} AM1.5G(\lambda)Xd\lambda = \frac{q}{hc} \int \lambda AM1.5G(\lambda)Xd\lambda. \qquad (8.13)$$

The J_{sc} values were calculated from the AM1.5G spectrum, without the front reflection, the *EQE* response, and the active area *EQE* response of the solar cells [129]. The physical meaning and the calcualtion formula of each short circuit current density are listed in the following Table 8.3. The R_{OPAL} in the Table describes the front surface reflection from the non-metallized area of solar cells without considering the reflectance from the rear side of cells [130]. It is obtained from the simulation carried with "OPAL2" module from PV loghtouse with the input parameters of thickness and refractive index/extinction coefficient of the i/n stack and AZO on the front as shown in Fig. 8.9. Note that the input parameters for the simulation are acquired from ellipsometry measurement for the layers prepared on glass substrate with the same deposition parameters as in the solar cell. This difference can contribute to the mismatch as shown in Fig. 8.10(a). The physical meaning and calcualtion formulas are listed in Table 8.4 for the short circuit current density loss components related to the front surface reflection, the losses in short, medium and long wavelength regions, the shadowing, and the light ecape from the front and rear side of cell area without

Table 8.3. Physical meaning and calcualtion formulas for the current density values with the situations: the AM1.5G spectrum, without the front reflection simulated by "OPAL2", the *EQE* response, and the active area *EQE* response of the solar cell.

symbol	physical meaning	formula
$J_{AM1.5G}$	The *J* generated from the AM1.5G spectrum	$J_{AM1.5G} = \frac{q}{hc} \int_{300}^{1200} \lambda AM1.5G(\lambda)d\lambda$
$J_{1-front\,refl.}$	The *J* generated without the front reflection simulated by "OPAL2" model	$J_{1-front\,refl.} = \frac{q}{hc} \int_{300}^{1200} \lambda AM1.5G(\lambda)[1 - R_{OPAL}(\lambda)]d\lambda$
$J_{sc,EQE}$	The *J* generated witht the EQE response	$J_{sc,EQE} = \frac{q}{hc} \int_{300}^{1200} \lambda AM1.5G(\lambda)EQE(\lambda)d\lambda$
$J_{EQE,active\,area}$	The *J* generated witht the active area EQE response	$J_{EQE,active\,area} = \frac{q}{hc} \int_{300}^{1200} \lambda AM1.5G(\lambda)EQE_{active\,area}(\lambda)d\lambda$

metallization. Note that though the cells prepared in this work have mostly full area back meatllization, the analysis of $J_{rear\ escape}$ could be benefit for the bifacial cell design in further applications. Here, the $J_{rear\ escape}$ is only to be explaned, but not for the following analysis. The transmission T_{cell} and reflection R_{cell} were measured with the photo spectrometer on the cell area without metallization. The active area EQE response, 1-$R_{front\ refl.}$, and 1-R_{cell} spectra are presented in Fig. 8.10(a), short circuit current density related to each contributing conponenet over the wavelength are plotted in Fig. 8.10(b), and the distribution for the short circuit current denisty contributing conponenets and the current loss contributing conponenets are shown in Fig. 8.10(c) and Fig. 8.10(d).

The short circuit current distribution is presented in Fig. 8.10(c). The first column shows the current density $J_{AM1.5G}$ of 45.9 mA/cm^2 which a solar cell can get from the AM1.5G spectrum in the wavelength range of 300-1200 nm with all the incident photons converted to electrons. The scecond conlumn presents the combination of $J_{front\ refl.}$ and $J_{1-front\ refl.}$ with the values of 0.7 and 45.2 mA/cm^2, respectively. The combination of $J_{front\ refl.}$ and $J_{1-front\ refl.}$ is equal to the current denisty measured from the AM1.5G spectra. The $J_{front\ refl.}$ describes the current loss related to the front reflection simulated by "OPAL2" module. However, since the wafer thickness was assumed infinitem, the influence of the rear side was not considered. The third column presentes the active area EQE response $J_{EQE,\ active\ area}$ of 38.7 mA/cm^2 related to the area without metallization. The

Table 8.4 Physical meaning and calcualtion formulas for the current density losses: from the front reflection of non-metallization area in solar cell, in the short, medium and long wavlength regions, from the front shadowing, and from the light escape in the front and rear side of the cell without metallization. In our case, rear escape is not taken into consideration.

symbol	physical meaning	formula
$J_{front\ refl.}$	The J loss from the front reflection simulated by "OPAL2"	$J_{front\ refl.} = \frac{q}{hc}\int_{300}^{1200} \lambda AM1.5G(\lambda)R_{OPAL}(\lambda)d\lambda$
J_{short}	The J loss in the short wavelength region	$J_{short} = \frac{q}{hc}\int_{300}^{600} \lambda AM1.5G(\lambda)[1 - R_{cell}(\lambda) - T_{cell}(\lambda) - EQE(\lambda)]d\lambda$
J_{medium}	The J loss in the medium wavelength region	$J_{medium} = \frac{q}{hc}\int_{600}^{1000} \lambda AM1.5G(\lambda)[1 - R_{cell}(\lambda) - T_{cell}(\lambda) - EQE(\lambda)]d\lambda$
J_{long}	The J in the long wavelength region	$J_{long} = \frac{q}{hc}\int_{1000}^{1200} \lambda AM1.5G(\lambda)[1 - R_{cell}(\lambda) - T_{cell}(\lambda) - EQE(\lambda)]d\lambda$
$J_{shadowing}$	The J loss from the front shadowing of solar cell	$J_{shadowing,loss} = J_{EQE} \times f_{metal}$
$J_{front\ escape}$	The J loss due to the light escape from the front side of solar cell	$J_{front\ escape,loss} = \frac{q}{hc}\int_{850}^{1200} \lambda AM1.5G(\lambda)[R_{cell}(\lambda) - R_{OPAL}(\lambda)]d\lambda$
$J_{rear\ escape}$	The J loss due to the light escape from the rear side of cell without meatllization	$J_{rear\ escape,loss} = \frac{q}{hc}\int_{850}^{1200} \lambda AM1.5G(\lambda)T_{cell}(\lambda)d\lambda$

fourth column shows the combination of the J_{sc} from QE response 37.4 mA/cm^2 and the shadowing loss $J_{shadowing}$ of 1.3 mA/cm^2 which equals to the products of the $J_{sc, EQE}$ and the metal fraction f_m in the cell aperature area. The fifth column shows the combination of $J_{sc, EQE}$ and the total current density loss $J_{total\ loss}$ of 8.4 mA/cm^2 in the solar cells which is merely approximately 0.1 mA/cm^2 lower than the $J_{AM1.5G}$. This difference could result from the mismatch in the short wavelength region shown in Fig. 8.10(a) which is attributed others.

The last column shows the short circuit current density loss distribution from the components of front reflection simulated by "OPAL2", the shadowing, the escape from the front side of the solar cells, and the losses in the short, medium and long wavelength regions of measuremed wavelength range. The detailed disctributing and ranking are summarized in Fig. 8.10(d). The main current losses are related to the losses in the short and long wavelength regions, the light escape at the front side of the solar cells, and the shadowing loss at the front side of the solar cells. Total current density loss is 8.4 mA/cm^2 which is 18.3 % from the $J_{AM1.5G}$. In the total current density loss, the highest current loss J_{long} of 25.8 % is from the parasitic absorption in TCO/metal electrode in the
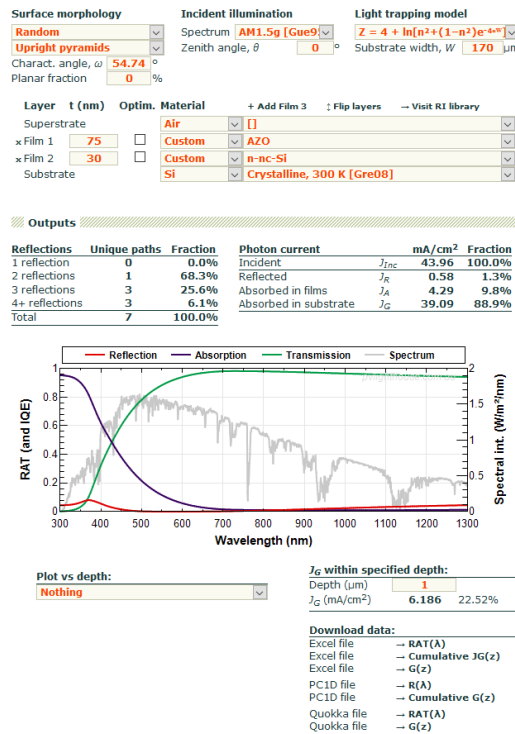
Fig. 8.9. Simulation for the front surface reflection of the non-metaiilzation area in the solar cell with the "OPAL2" module from PV lighthouse.
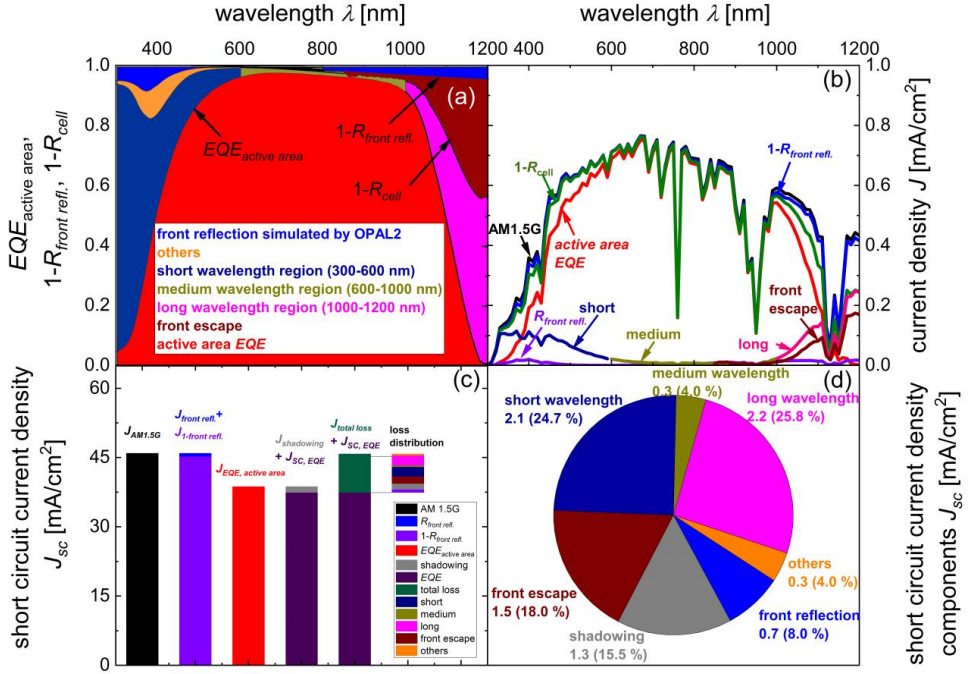
Fig. 8.10. Short circuit current density loss analysis: (a) the spectra of active area *EQE* response, 1-$R_{front\ refl.}$, and 1-R_{cell} for the solar cells with related components leading to current density loss; (b) the current density curves as a function of wavelength for each current density loss contribution component; (c) the distribution of short circuit current densities and current density loss contribution components; and (d) the detailed distribution and ranking for the current density loss contribution components. The numbers in graph 8.10(d) is in the unit of mA/cm^2.

long wavelength region. The J_{long} can be reduced with the AZO optimization in the directions of optical properties to reduce parasitic absorption or advanced rear reflector design. The current loss J_{short} in short wavelength region of 24.7 % is related to parasitic absorption and the insufficient collection of the high energy photons. The can be reduced by reducing the window layer thickness or use high bandgap materials. The light escape from the front side of the cell $J_{front\ escape}$ contributed to 18.0 % of the total loss, which is needed to be considered together with the J_{long} since there is a trade off between the light to be absorbed and to be reflected. The current density loss from shadowing is 15.5 % which needs to be optimized with metallization process. As for the current loss of 8.0 % from the front surface reflection, the fornt layer stack containing both of the Si layer and AZO film should be taking into consideration. There is approximate 4.0 % current density loss in the medium wavemength region due to the insufficient collection and recombination. The other

4.0 % current density loss results from the uncertainty in the accuracy of the parameters or other reasons.

8.6 Short summary

This chapter introduces the theoretical limits for the SHJ solar cells fabricated in this work and presents the loss analysis for the cell parameters followed by suggestions for further improvement. Loss analysis of the open circuit voltage shows a difference between 19 mm ×19 mm size cell and M2 cell. Compared to the V_{oc} theoretical limit, the V_{oc} values achieved from I-V characterization are approximately 30 mV and 20 mV lower for the SHJ solar cells with the sizes of 19 mm ×19 mm and M2, respectively. This difference is to large extent attributed to the surface or SRH recombination. For the 19 mm ×19 mm size cells fabricated in the 78 mm ×78 mm size wafer, there is a voltage difference between the iV_{oc} and the V_{oc}, however, the same voltage difference for M2 cell is obviously smaller. This smaller difference is supposingly related to the lower perimeter recombination loss and better carrier selective contact. The fill factor loss analysis shows that the main losses originates from series resistance and the J_{02} related recombination. The fill factor loss from the series resistance is attributed to the high resistance of front metal contacts. The fill factor loss from the J_{02} recombination is supposingly related to recombination in junction regions.

The series resistance loss analysis shows that the main loss originates from the fingers and the contact resistance at the interface between the p-type Si layer and AZO film. For the high contact resistance at the interface of p-type Si layer and AZO film, both of the Si layer and the AZO film need to be optimzed.

The short circuit current density loss analysis shows that the main contributors are from the current losses in the short and long wavelength regions J_{short}, J_{long},the front escape loss $J_{front\ escape}$ of the non-metalized area of solar cells, and the front metal shadowing loss $J_{shadowing}$. Further optimization of AZO in thickness and absorption properties properties are required to maximize J_{sc} in SHJ cells with AZO.

Chapter 9 Summary and outlook

9.1 Summary

Doped nc-Si layers and AZO

Based on the conventional SHJ solar cells with ITO and doped a-Si layers, the SHJ solar cells with Al-doped zinc oxide and n-/p- type nanocrystalline Si layers have been developed in this work. The layers of doped nc-Si were deposited on glass substrates without or with intrinsic a-Si layer underneath for optimization. The samples on glass were characterized for the deposition rate, crystalline volume fraction, conductivity, and absorption coefficient. Effects of RF discharge power and gas flow ratios of r_{SiH4} and r_{PH3} have been studied during the development of n-type nc-Si. The n-type nc-Si layers deposited with r_{SiH4} of 0.01 show higher crystalline volume fraction I_c and conductivity σ compared to the Si layer deposited with r_{SiH4} of 0.02. Higher I_c and σ are acquired for the n-type nc-Si deposited at 200 W compared to other powers with r_{SiH4} of 0.01. Variation of r_{PH3} in the range of 0.5-2 has slight influence on the properties of n-type nc-Si layer. Effect of thickness on the properties of n-type nc-Si is studied. The thickness of n-type nc-Si was varied in the range of 24-90 nm. Optimum thickness on glass was found at 35 nm with conductivity of 10^{-1} S/cm. The thickness is equivalent to approximately 20 nm on textured wafer surface of a solar cell. Thus, the parameters set of 200°C substrate temperature, 200 W power, 0.01 for r_{SiH4} and r_{PH3}, 2.5 mbar pressure, and 20-nm thickness was taken as optimal for the n-type nc-Si layer implemented in SHJ solar cells.

P-type nc-Si layers were developed after the development of n-type nc-Si layer at the same power of 200 W and substrate temperature of 200°C. TMB or B_2H_6 has been used as doping gas precursors for Si layer deposition. The gas flow rate ratio r_{TMB} and deposition pressures have been varied for the p-type nc-Si layer development. The p-type nc-Si layer shows a conductivity of 1×10^{-2} S/cm at the thickness of approximately 20 nm on textured surface with the deposition parameter set of 200°C substrate temperature, 200 W power, 0.01 for r_{SiH4}, 0.5 for r_{TMB}, 2.5 mbar pressure, and 20-nm thickness. This layer is the most optimal for the SHJ solar cell fabrication in current study. The p-type nc-Si layer deposited with B_2H_6 instead of TMB as a doping gas precursor did not show proper electrical properties in a preliminary investigation.

Development of AZO films for SHJ solar cells have been performed initially on glass substrates with variation of pressures, power densities, substrate temperatures, doping concentrations, and gas precursor in magnetron sputtering process. Optical and electrical properties of AZO films were characterized with transmittance and reflectance measurements and Hall measurements. The results of AZO pressures series indicate that lower sputtering pressure facilitates higher carrier mobility and lower resistivity of AZO film. Sputtering pressure of 0.1 Pa is used for the AZO development due to the highest mobility acquired in AZO pressure series. There was no distinct effect of the power density varied between 1.3-2.7 W/cm^2 on optical and electrical properties of AZO. However, somewhat higher mobility was obtained with the power density of 2.0 W/cm^2 which was fixed for the following AZO development.

Influence of substrate temperature during AZO sputtering has been studied to identify optimal preparation conditions of AZO for SHJ solar cells. Increase of heater temperature during AZO sputtering and post-deposition annealing have only slight influence on the optical properties as well as on the electrical properties. Effect of Al doping concentration has been studied with additional AZO series sputtered with 2 wt.% AZO target. AZO films sputtered with 2 wt.% target show approximately twice higher of the free carrier concentration, but twice lower carrier mobility and therefore similar resistivity to AZO sputtered with 1 wt.% target. However, AZO films sputtered with 2 wt.% target show higher optical absorptance in long wavelength region compared to 1 wt.% AZO films. To reduce the parasitic absorption for AZO films sputtered with 2 wt.% target, 0.5% O_2 was introduced to the sputtering gas precursor. The absorptance has been successfully reduced in the wavelength region above 1000 nm, however, the reduction comes at the cost of reduction in carrier mobility and therefore increase in resistivity. The absorptance in 2 wt.% AZO with oxygen appeared to be very similar to the absorptance of AZO films sputtered with 1 wt.% target. Both heater temperature and post-deposition annealing have slight influence either on the transmittance and absorptance, or the resistivity, mobility and carrier concentration of the AZO films sputtered with the 2 wt.% target. It has been found that RT sputtered AZO with 1 wt.% target is the optimal material for SHJ solar cells among studied options due to its high mobility, low resistivity, and low absorptance.

SHJ solar cell results

In this section, the contacts of AZO layers with doped nanocrystalline or amorphous Si layers were tested in the rear emitter SHJ solar cells on n-type textured Czochralski Si wafers. The sputtering parameters for the AZO applied in SHJ solar cells have been varied in terms of target doping concentrations, gas precursors, and substrate temperatures (RT, 150ºC, and 200ºC). J-V, *IQE* and 1-reflection, and contact resistance measurements have been used to characterize cell performance.

Cells with p-type a-Si layers show proper J-V characteristics, and Cells with n-type nc-Si layer have higher *J$_{sc}$* compared to the cells with n-type a-Si layer. Cells with p-type nc-Si layers reveal

strong s-shaped J-V curves due to the improper contact at the interface between p-type nc-Si and AZO film.

Lower J_{sc} values were observed for the cells with AZO sputtered with 2 wt.% target compared to the cells with AZO sputtered with 1 wt.% target, which is due to the higher carrier density in AZO film resulting in higher parasitic absorption. AZO sputtering temperature has slight influence on J_{sc} variation confirmed by QE response as well. Compared to the cell with AZO sputtered with 1 wt.% target, the cell with AZO sputtered with 2 wt.% target shows a lower QE response in the long wavelength region due to the higher free carrier absorption in AZO. The cell with the AZO sputtered with 2 wt.% target and O_2 in precursor gas shows slightly higher QE response in the short wavelength region. The active area $J_{EQE, active area}$ values calculated from the EQE response are 38.7 mA/cm^2 for the cell with 1 wt.% AZO, 37.9 mA/cm^2 for the cell with 2 wt.% AZO, 38.8 mA/cm^2 for the cell with 2 wt.% AZO and oxygen in the precursor, respectively. From the QE point of view AZO layers sputtered with 1 wt.% target at room temperature appeared to be most suitable for high efficiency solar cells.

AZO sputtering temperature as well as AZO target doping concentration have no obvious influence on V_{oc} in studied SHJ cells. However, the V_{oc} values show decrease trend with the increase of AZO sputtering temperatures. Increase in AZO sputtering temperature, doping concentration, and oxygen content all have negative influence on FF. Cell efficiency decreases with the increased AZO sputtering temperature. The highest efficiency of 21.2 % for the 19 mm × 19 mm cell is achieved for the cell with 1 wt.% RT sputtered AZO (V_{oc} = 720 mV, J_{sc} = 39.1 mA/cm^2 and FF = 75.4 %).

Contact resistances between AZO and silver (AZO/Ag) and between AZO and Si layer have been measured with TLM method in cells with RT sputtered AZO. The contact resistance between AZO and p-type a-Si is approximately twice lower than contact resistance between ITO and p-type a-Si. For the AZO contact to the p-type nc-Si layer, non-ohmic I-V curve is observed from the TLM measurement, indicating improper contact between AZO and p-type nc-Si layer. The n-type Si layer shows proper ohmic contact with AZO layers prepared with different sputtering parameters. The contact resistances between n-type Si layers and 1 wt.% AZO was averagely 27 mΩ/cm^2 which is lower than the value of averagely 66 mΩ/cm^2 observed for the 2 wt.% AZO. Therefore, better performance has been observed for the 1wt.% AZO in the studied SHJ solar cells.

Influence of AZO sputtering on passivation

Quality of surface defect passivation is typically characterized by effective carrier lifetime measured by QSSPC technique. In this section, effective carrier lifetime curves, effective carrier lifetime values τ_{eff}, implied open circuit voltage iV_{oc}, and implied fill factor iFF have been summarized after each procedure during SHJ solar cell fabrication process.

Influence of AZO sputtering on effective carrier lifetime of symmetrical structures with intrinsic a-Si/n-type nc-Si (i/n stack) or intrinsic a-Si/p-type a-Si (i/p stack) on both sides of wafer has been explored. Influence of pressures and substrate temperatures during AZO sputtering on carrier

lifetime in i/n stack and i/p stack has been investigated, in which n-type nc-Si layer was deposited with r_{SiH4} (a ratio between the flow rates of silane and hydrogen) of 0.01. Effect of room temperature sputtered AZO on effective carrier lifetime in i/n symmetrical stack was studied as well with n-type Si layers deposited with different r_{SiH4} and thickness. Furthermore, influence of RT sputtered AZO on the effective carrier lifetime of cell precursor was studied.

The effective carrier lifetime in i/n and i/p symmetrical stacks was measured after Si layer stack deposition, AZO sputtering, annealing, and AZO removal. Normally high initial effective carrier lifetime after Si layer deposition is significantly reduced after AZO sputtering and mostly recovers after annealing. The detrimental effect of AZO sputtering process on Si layers is eliminated completely by annealing. Simultaneously the presence of AZO film results in the reduction of effective carrier lifetime in low excess carrier density region for i/p stack which is likely related to the work function mismatch between AZO and Si layer. Variation of sputtering pressures has no influence on the lifetime curve variation over the treatment procedure for both i/n and i/p stacks. Increase of sputtering substrate temperature of AZO leads to obvious improvement of the effective lifetime after AZO sputtering for both i/n and i/p symmetrical samples which is related to the in-situ annealing. However, this difference is eliminated by post-deposition annealing. N-type Si layers prepared with higher r_{SiH4} appears to be less sensitive to the damage associated with AZO sputtering.

Lifetime monitoring for cell precursors shown similar lifetime evolution upon treatment procedure to the symmetrical stacks studied earlier. Similarly, the lifetime in the low excess carrier density after annealing is not recovered completed due to i/p stack. Furthermore, incomplete lifetime recovery has no influence on the iV_{oc} and iFF, thus the solar cell operation.

Contacts at the interfaces between AZO and p-type Si layers

Heavily distorted s-shaped light J-V curves were observed for SHJ solar cells with p-type nc-Si layer. The J-V characteristics comparison for cells with introducing an extra p-type a-Si prior to or after the deposition of p-type nc-Si indicates that the contact barrier locates at the interface between p-type nc-Si and AZO. Temperature dependent J-V measurements reveal pronounced thermal activation property indicating the presence of a carrier collection barrier. The I-V characteristics of the barrier was reconstructed via the analysis of voltage offsets between dark I-V and I_{sc}-V_{oc}, or light I-V and I_{sc}-V_{oc} curves. The non-linear relationship between the voltage offsets and current level confirms the presence of a transport barrier at the interface between p-type nc-Si and AZO. Properties of p-type nc-Si layer and AZO have been varied to improve the contact barrier. Increasing the doping in p-type nc-Si layer or inserting a seed layer prior to p-type nc-Si layer reduce the contact barrier. Increasing the substrate temperature during sputtering or AZO doping concentration have slight influence on the s-shaped light J-V curve. Thus, the critical point is lying within the p-type nc-Si layer development. A μc-Si:H thin-film cell was prepared as well with p-type μc-Si deposited on AZO to verify if preparation sequence would make an effect

on the contact properties. The µc-Si:H thin-film cell shows proper J-V characteristic which indicates that the preparation order could also affect the contact between AZO and p-type Si layer.

Loss analysis

Deatiled loss analysis for parameters V_{oc}, FF, R_s, and J_{sc} of the best performance cell has been performaed with respect to the state-of-the-art theroretical limits.

Measurements of iV_{oc} or V_{oc} were performed between solar cell fabarictaion steps. Compared to the theoretical limit of V_{oc}, the measured V_{oc} are approximately 30 mV and 20 mV lower for the SHJ solar cells with the sizes of 19 mm ×19 mm and M2, respectively. This difference to large extent is attributed to the surface and SRH recombination. Room temperature AZO sputtering reduces iV_{oc}, while it can be recovered with the subsequent annealing. There is a approximately 15 mV difference between iV_{oc} measured after annealing and real V_{oc} measured with the sun simulator in a 19 mm ×19 mm size cell. This V_{oc} loss is attributed to perimeter recombination loss and the imperfect carrier selectivity of the contacts. This loss is much smaller, approximately 5 mV, in the case of full area M2 cells which is related to the contact selectivity issues.

The fill factor loss analysis is carried out in two ways. One method is based on the two-diode model, and another one is based on the comparison of measured parameters like iFF, pFF, and FF with theoretical limit. The main FF losses are from the R_s and the recombination in the junction region. The FF loss from the R_s is mainly attributed to metallization. The FF loss related to the recombination is attributed to the non-optimal junction formation. Compared to the theoretical limit of FF of 88.6 %, there is total loss of 13.1 % as for the solar cells. The FF loss of 4.9 % is from the R_s, and the FF loss of 3.1 % is from the imperfect carrier selectivity of the contacts.

The R_s was calculated as a sum of the bulk resistances of the layers and the contact resistances between the layers in solar cells. The calculation shows that 73.4 % of the loss comes from the series resitance of metal fingers . The contact resistance at the interface between the p-type Si layer and AZO film and the i/p stack reistance are the second and thrid high loss components with 13.3 % and 4.3% of total R_s. The resistance of front fingers, i/p stack and the contact resistacne between AZO and p-type Si layer are therefore most crucial for further R_s reduction.

Losses of J_{sc} were estimated using EQE response, reflection spectrum of the non-metallization area of solar cell, and simulated front surface reflection with "OPAL2' module. Main J_{sc} losses are from the parasitic absorption in the short and long wavelength regions, light escape from front side of the cell area without metallization, and front metal shadowing.

9.2 Outlook

This work delivered promising results and encourages further investigation of the SHJ solar cells with Al-doped zinc oxide (AZO), particularly with AZO sputtered at room temperature. Based on the solar cells developed in this work, the following recommendations for the further development on both material level and device level are given:

Material level

Optical and electrical properties of doped nc-Si layers require optimization as for suitable conductivity, absorption/reflection properties, and proper contact with AZO. Proper nucleation is critical for the growth of nc-Si, therefore, a suitable seed layer or treatment on the a-Si layer is needed for the very thin doped nc-Si layers. The contact at the interfaces between AZO and doped Si layer needs further investigation. Particularly the contact between p-type nc-Si and AZO requires improvement to overcome the contact barrier at the interface. Increasing the doping concentration in p-type nc-Si and increasing the workfunction of AZO film are options to optimize the contact property. Simultaneously options for improveing the properties of doped nc-Si layers need to be further explored.

As for AZO film, three aspects need improvement: parasitic absorption in the short and long wavelength regions of solar spectum, contact proeprty for the AZO film to Si layer, and degradation reduction of the effective carrier lifetime related to AZO sputtering with e.g. by means of "softer" sputtering process for a thin buffer layer applied to the surface of Si layer.

Device level

Based on the loss analysis on the parameters of SHJ solar cells with AZO, following optimization routes are identified. Further improvement of open circuit voltage requires optimization of passivation and carrier selective contacts which can be achieved with technical improvements for cell preparation and use of novel materials. Optimization for fill factor needs improvement in metallization, reduction of series resistance, and improved junction quality. Multi-printing can be used to reduce series resistance without increasing shadowing. Further optimization of Si and TCO layers has to be conducted to reduce series resistance in the contact layer stack. Improvement of short circuit current density is a matter of further optimization of metallization and optical performance of the cell stack. Multi-printing for metal contacts can reduce shadowing loss. Fine tuning of the front layer thicknesses can reduce parasitic absorption and reflection losses. Further reduction of parasitic absorption may be facilited by using novel carrier selective contacts.

References

[1]   BP statistical review of world energy, 68th edition, Jun. 2019. https://www.bp.com/content/dam/bp/business-sites/en/global/corporate/pdfs/energy-economics/statistical-review/bp-stats-review-2019-full-report.pdf.

[2]   BP energy outlook, 2019 edition. https://www.bp.com/content/dam/bp/business-sites/en/global/corporate/pdfs/energy-economics/energy-outlook/bp-energy-outlook-2019.pdf.

[3]   M. A. Green, "Photovoltaic principles," *Physica E*, vol. 14, no. 1-2, pp.11-17, 2002.

[4]   Best research-cell efficiency chart, https://www.nrel.gov/pv/cell-efficiency.html.

[5]   A. Goetzberger, J. Luther, and G. Willeke, "Solar cells: past, present, future," *Solar Energy Materials and Solar Cells*, vol. 74, no. 1-4, pp. 1-11, 2002.

[6]   M. A. Green, "The path to 25% silicon solar cell efficiency: History of silicon cell evolution," *Progress in Photovoltaics: Research and Applications,* vol. 17, no. 3, pp. 183-189, 2009.

[7]   R. S. Ohl, "Light-sensitive electric device," patent no. US2402662, Jun. 1946.

[8]   R. S. Ohl, "Light-sensitive electric device including silicon," patent no. US2443542, Jun. 1948.

[9]   M. A. Green, "Third generation photovoltaics: solar cells for 2020 and beyond," *Physica E*, vol. 14, no. 1-2, pp. 65-70, 2002.

[10]   G. Conibeer, "Third-generation photovoltaics," *Materials Today,* vol. 10, no. 11, pp. 42-50, 2007.

[11]   S. K. Chunduri and M. Schmela, "Heterojunction solar technology. The next big thing in solar cell/module manufacturing?," Taiyang News Report, 2019. http://taiyangnews.info/reports/heterojunction-solar-technology-2019-report/.

[12]   A. W. Blakers, A. Wang, A. M. Milne, J. Zhao, and M. A. Green, "22.8% efficient silicon solar cell," *Applied Physics Letters,* vol. 55, no. 13, pp. 1363-1365, 1989.

[13]   E. Schneiderloechner, R. Preu, R. Luedemann, and S. W. Glunz, "Laser-fired rear contacts for crystalline silicon solar cells," *Progress in Photovoltaics: Research and Applications,* vol. 10, no. 1, pp. 29-34, 2002.

[14]   M. Taguchi, A. Yano, S. Tohoda, K. Matsuyama, Y. Nakamura, T. Nishiwaki, K. Fujita, and E. Maruyama, "24.7% record efficiency HIT solar cell on thin silicon wafer," *IEEE Journal of Photovoltaics,* vol. 4, no. 1, pp. 96-99, 2014.

[15]   K. Masuko, M. Shigematsu, T. Hashiguchi, D. Fujishima, M. Kai, N. Yoshimura, T. Yamaguchi, Y. Ichihashi, T. Mishima, N. Matsubara, T. Yamanishi, T. Takahama, M. Taguchi, E. Maruyama, and S. Okamoto, "Achievement of more than 25% conversion

References

efficiency with crystalline silicon heterojunction solar cell," *IEEE Journal of Photovoltaics,* vol. 4, no. 6, pp. 1433-1435, 2014.

[16] S. De Wolf, A. Descoeudres, Z. C. Holman, and C. Ballif, "High-efficiency silicon heterojunction solar cells: A review," *Green,* vol. 2, no. 1, pp. 7-24, 2012.

[17] K. Yoshikawa, H. Kawasaki, W. Yoshida, T. Irie, K. Konishi, K. Nakano, T. Uto, D. Adachi, M. Kanematsu, H. Uzu, and K. Yamamoto, "Silicon heterojunction solar cell with interdigitated back contacts for a photoconversion efficiency over 26%," *Nature Energy,* vol. 2, Art. no. 17032, 2017.

[18] J. Werner, B. Niesen, and C. Ballif, "Perovskite/silicon tandem solar cells: Marriage of convenience or true love story? - An overview," *Advanced Materials Interfaces,* vol. 5, Art. no.1700731, 2018.

[19] F. Sahli, J. Werner, B. A. Kamino, M. Braeuninger, R. Monnard, B. Paviet-Salomon, L. Barraud, L. Ding, J. J. Diaz Leon, D. Sacchetto, G. Cattaneo, M. Despeisse, M. Boccard, S. Nicolay, Q. Jeangros, B. Niesen, and C. Ballif, "Fully textured monolithic perovskite/silicon tandem solar cells with 25.2% power conversion efficiency," *Nature Materials,* vol. 17, pp. 820-826, 2018.

[20] A. Richter, M. Hermle, and S. W. Glunz. "Reassessment of the limiting efficiency for crystalline silicon solar cells," *IEEE Journal of Photovoltaics,* vol. 3, no. 4, pp. 1184-1191, 2013.

[21] P. Kowalczewski and L. C. Andreani, "Towards the efficiency limits of silicon solar cells: How thin is too thin?," *Solar Energy Materials and Solar Cells,* vol. 143, pp. 260-268, 2015.

[22] Panasonic HIT® solar cell achieves world's highest energy conversion efficiency of 25.6% at research level, Apr. 2014. https://eu-solar.panasonic.net/en/2402.htm.

[23] K. Nakamura, "Current status and technology trend of crystalline Si solar cell," in *24th International Workshop on Active-Matrix Flatpanel Displays and Devices (AM-FPD)*, Kyoto, Japan, 2017.

[24] M. A. Green, "The passivated emitter and rear cell (PERC): From conception to mass production," *Solar Energy Materials and Solar Cells,* vol. 143, pp. 190-197, 2015.

[25] M. Fischer, "ITRPV 10th edition 2019- report release and key findings," in *PV CellTech Conference*, Penang, Malaysia, 2019. https://itrpv.vdma.org/.

[26] T. Dullweber and J. Schmidt, "Industrial silicon solar cells applying the passivated emitter and rear cell (PERC) concept-A review," *IEEE Journal of Photovoltaics,* vol. 6, no. 5, pp. 1366-1381, 2016.

[27] S. K. Chunduri and M. Schmela, "PERC solar cel technology. PERC+: How to improve high efficiency crystalline solar cells," TaiyangNews Report, 2018. http://taiyangnews.info/reports/perc-solar-cell-technology-report-2018/.

[28] J. Zhao, A. Wang, and M. A. Green "24.5% Efficiency silicon PERT cells on MCZ substrates and 24.7% efficiency PERL cells on FZ substrates", *Progress in Photovoltaics: Research and Applications,* vol. 7, no. 6, pp. 471-474, 1999.

[29] T. G. Allen, J. Bullock, X. Yang, A. Javey, and S. De Wolf, "Passivating contacts for crystalline silicon solar cells," *Nature Energy*, vol. 4, pp. 914-928, 2019.

[30] J. Melskens, B. W. H. van de Loo, B. Macco, L. E. Black, S. Smit, and W. M. M. Kessels, "Passivating contacts for crystalline silicon solar cells: From concepts and materials to prospects," *IEEE Journal of Photovoltaics,* vol. 8, no. 2, pp. 373-388, 2018.

[31] A. Richter, J. Benick, F. Feldmann, A. Fell, M. Hermle, and S. W. Glunz, "n-Type Si solar cells with passivating electron contact: Identifying sources for efficiency limitations by wafer thickness and resistivity variation," *Solar Energy Materials and Solar Cells,* vol. 173, pp. 96-105, 2017.

[32] H. Steinkemper, M. Hermle, and S. W. Glunz, "Comprehensive simulation study of industrially relevant silicon solar cell architectures for an optimal material parameter choice," *Progress in Photovoltaics: Research and Applications,* vol. 24, no. 10, pp. 1319-1331, 2016.

[33] E. Yablonovitch, T. Gmitter, R. M. Swanson, and Y. H. Kwark, "A 720 mV open circuit voltage SiO_x:c-Si:SiO_x double heterostructure solar cell," *Applied Physics Letters,* vol. 47, no. 11, pp. 1211-1213, 1985.

[34] K. Yamamoto, D. Adachi, H. Uzu, M. Ichikawa, T. Terashita, T. Meguro, N. Nakanishi, M. Yoshimi, and J. L. Hernández, "High-efficiency heterojunction crystalline Si solar cell and optical splitting structure fabricated by applying thin-film Si technology," *Japanese Journal of Applied Physics,* vol. 54, no. 8S1, pp. 08KD15, 2015.

[35] D. Adachi, J. L. Hernández, and K. Yamamoto, "Impact of carrier recombination on fill factor for large area heterojunction crystalline silicon solar cell with 25.1% efficiency," *Applied Physics Letters,* vol. 107, no. 23, pp. 233506, 2015.

[36] J. Zhao, M. Koenig, Y. Yao, Y. C. Wang, R. Zhou, T. Xie, and H. Deng, "24% Silicon heterojunction solar cells on Meyer Burger's on mass production tools and how wafer material impacts cell parameters," in *IEEE 7th World Conference on Photovoltaic Energy Conversion (WCPEC)*, Waikoloa Village, HI, USA, 2018.

[37] F. Sahli, B. A. Kamino, J. Werner, M. Braeuninger, B. Paviet-Salomon, L. Barraud, R. Monnard, J. P. Seif, A. Tomasi, Q. Jeangros, A. Hessler-Wyser, S. De Wolf, M. Despeisse, S. Nicolay, B. Niesen, and C. Ballif, "Improved optics in monolithic perovskite/silicon tandem solar cells with a nanocrystalline silicon recombination junction," *Advanced Energy Materials,* vol. 8, no. 6, pp. 1701609, 2018.

[38] K. A. Bush, A. F. Palmstrom, Z. J. Yu, M. Boccard, R. Cheacharoen, J. P. Mailoa, D. P. McMeekin, R. L. Z. Hoye, C. D. Bailie, T. Leijtens, I. M. Peters, M. C. Minichetti, N. Rolston, R. Prasanna, S. Sofia, D. Harwood, W. Ma, F. Moghadam, H. J. Snaith, T. Buonassisi, Z. C. Holman, S. F. Bent, and M. D. McGehee, "23.6%-efficient monolithic perovskite/silicon tandem solar cells with improved stability," *Nature Energy,* vol. 2, Art. no. 17009, 2017.

[39] A. Huebner, A. G. Aberle, and R. Hezel, "Novel cost-effective bifacial silicon solar cells with 19.4% front and 18.1% rear efficiency," *Applied Physics Letters,* vol. 70, no. 8, pp. 1008-1010, 1997.

References

[40]   R. Guerrero-Lemus, R. Vega, T. Kim, A. Kimm, and L. E. Shephard, "Bifacial solar photovoltaics - A technology review," *Renewable and Sustainable Energy Reviews,* vol. 60, pp. 1533-1549, 2016.

[41]   S. K. Chunduri and M. Schmela, "Bifacial solar module technology. Getting ready for much higher yields with bifacial modules," TaiyangNews Report, 2018. http://taiyangnews.info/reports/bifacial-solar-technology-report-2018/.

[42]   Z. C. Holman, A. Descoeudres, L. Barraud, F. Z. Fernandez, J. P. Seif, S. De Wolf, and C. Ballif, "Current losses at the front of silicon heterojunction solar cells," *IEEE Journal of Photovoltaics,* vol. 2, no. 1, pp. 7-15, 2012.

[43]   N. Jensen, R. M. Hausner, R. B. Bergmann, J. H. Werner, and U. Rau, "Optimization and characterization of amorphous/crystalline silicon heterojunction solar cells," *Progress in Photovoltaics: Research and Applications,* vol. 10, no. 1, pp. 1-13, 2002.

[44]   A. Descoeudres, Z. C. Holman, L. Barraud, S. Morel, S. De Wolf, and C. Ballif, ">21% efficient silicon heterojunction solar cells on n- and p-type wafers compared," *IEEE Journal of Photovoltaics,* vol. 3, no. 1, pp. 83-89, 2013.

[45]   H. Savin, P. Repo, G. von Gastrow, P. Ortega, E. Calle, M. Garín, and R. Alcubilla, "Black silicon solar cells with interdigitated back-contacts achieve 22.1% efficiency," *Nature Nanotechnology,* vol. 10, pp. 624-628, 2015.

[46]   K. Yoshikawa, W. Yoshida, T. Irie, H. Kawasaki, K. Konishi, H. Ishibashi, T. Asatani, D. Adachi, M. Kanematsu, H. Uzu, and K. Yamamoto, "Exceeding conversion efficiency of 26% by heterojunction interdigitated back contact solar cell with thin film Si technology," *Solar Energy Materials and Solar Cells,* vol. 173, pp. 37-42, 2017.

[47]   E. Franklin, K. Fong, K. McIntosh, A. Fell, A. Blakers, T. Kho, D. Walter, D. Wang, N. Zin, M. Stocks, E.-C. Wang, N. Grant, Y. Wan, Y. Yang, X. Zhang, Z. Feng, and P. J. Verlinden, "Design, fabrication and characterisation of a 24.4% efficient interdigitated back contact solar cell," *Progress in Photovoltaics: Research and Applications,* vol. 24, no. 4, pp. 411-427, 2016.

[48]   M. Bivour, S. Schroeer, M. Hermle, and S. W. Glunz, "Silicon heterojunction rear emitter solar cells: Less restrictions on the optoelectrical properties of front side TCOs," *Solar Energy Materials and Solar Cells,* vol. 122, pp. 120-129, 2014.

[49]   M. Taguchi, K. Kawamoto, S. Tsuge, T. Baba, H. Sakata, M. Morizane, K. Uchihashi, N. Nakamura, S. Kiyama, and O, Oota, "HIT^{TM} cells-high efficiency crystalline Si cells with novel structure," *Progress in Photovoltaics: Research and Applications,* vol. 8, no. 5, pp. 503-513, 2000.

[50]   W. E. Spear and P. G. Le Comber, "Subtitutional doping of amorphous silicon," *Solid State Communications*, vol. 17, pp. 1193-1196, 1975.

[51]   M. Balestrieri, D. Pysch, J. P. Becker, M. Hermle, W. Warta, and S. W. Glunz, "Characterization and optimization of indium tin oxide films for heterojunction solar cells," *Solar Energy Materials and Solar Cells,* vol. 95, no. 8, pp. 2390-2399, 2011.

[52]   S. Li, Z. Tang, J. Xue, J. Gao, Z. Shi, and X. Li, "Comparative study on front emitter and rear emitter n-type silicon heterojunction solar cells: The role of folded electrical fields," *Vacuum,* vol. 149, pp. 313-318, 2018.

[53]   D. Meza, A. Cruz, A. B. Morales-Vilches, L. Korte, and B. Stannowski, "Aluminum-doped zinc oxide as front electrode for rear emitter silicon heterojunction solar cells with high efficiency," *Applied Sciences,* vol. 9, no. 5, pp. 862, 2019.

[54]   L. Mazzarella, A. B. Morales-Vilches, M. Hendrichs, S. Kirner, L. Korte, R. Schlatmann, and B. Stannowski, "Nanocrystalline n-type silicon oxide front contacts for silicon heterojunction solar cells: Photocurrent enhancement on planar and textured substrates," *IEEE Journal of Photovoltaics,* vol. 8, no. 1, pp. 70-78, 2018.

[55]   D. Zhang, D. Deligiannis, G. Papakonstantinou, R. A. C. M. M. van Swaaij, and M. Zeman, "Optical enhancement of silicon heterojunction solar cells with hydrogenated amorphous silicon carbide emitter," *IEEE Journal of Photovoltaics,* vol. 4, no. 6, pp. 1326-1330, 2014.

[56]   K. Ellmer and R. Mientus, "Carrier transport in polycrystalline transparent conductive oxides: A comparative study of zinc oxide and indium oxide," *Thin Solid Films,* vol. 516, no. 14, pp. 4620-4627, 2008.

[57]   T. J. Coutts, D. L.Young, and X. Li, "Characterization of transparent conducting oxides," in *MRS Bulletin*, vol. 25, no. 8, pp. 58-65, 2000.

[58]   A. Solieman and M. A. Aegerter, "Modeling of optical and electrical properties of In_2O_3:Sn coatings made by various techniques," *Thin Solid Films*, vol. 502, no. 1-2, pp. 205-211, 2006.

[59]   A. Kanevce and W. K. Metzger, "The role of amorphous silicon and tunneling in heterojunction with intrinsic thin layer (HIT) solar cells," *Journal of Applied Physics,* vol. 105, no. 9, pp. 094507, 2009.

[60]   M. F. A. M. van Hest, M. S. Dabney, J. D. Perkins, D. S. Ginley, and M. P. Taylor, "Titanium-doped indium oxide: A high-mobility transparent conductor," *Applied Physics Letters,* vol. 87, no. 3, pp. 032111, 2005.

[61]   T. Koida and M. Kondo, "Improved near-infrared transparency in sputtered In_2O_3-based transparent conductive oxide thin films by Zr-doping," *Journal of Applied Physics,* vol. 101, no. 6, pp. 063705, 2007.

[62]   Y. Meng, X. Yang, H. Chen, J. Shen, Y. Jiang, Z. Zhang, and Z. Hua, "A new transparent conductive thin film In_2O_3: Mo," *Thin Solid Films*, vol. 394, pp. 219-223, 2001.

[63]   F. Meng, J. Shi, Z. Liu, Y. Cui, Z. Lu, and Z. Feng, "High mobility transparent conductive W-doped In_2O_3 thin films prepared at low substrate temperature and its application to solar cells," *Solar Energy Materials and Solar Cells,* vol. 122, pp. 70-74, 2014.

[64]   P. F. Newhouse, C. -H. Park, D. A. Keszler, J. Tate, and P. S. Nyholm, "High electron mobility W-doped In_2O_3 thin films by pulsed laser deposition," *Applied Physics Letters,* vol. 87, no. 11, pp. 112108, 2005.

[65]   M. Morales-Masis, S. M. De Nicolas, J. Holovsky, S. De Wolf, and C. Ballif, "Low-temperature high-mobility amorphous IZO for silicon heterojunction solar cells," *IEEE Journal of Photovoltaics,* vol. 5, no. 5, pp. 1340-1347, 2015.

References

[66] T. Koida, H. Fujiwara, and M. Kondo, "Hydrogen-doped In_2O_3 as high-mobility transparent conductive oxide," *Japanese Journal of Applied Physics*, vol. 46, no. 28, pp. L685–L687, 2007.

[67] J. A. Libera, J. N. Hryn, and J. W. Elam, "Indium oxide atomic layer deposition facilitated by the synergy between oxygen and water," *Chemistry of Materials,* vol. 23, no. 8, pp. 2150-2158, 2011.

[68] T. Minami, "Present status of transparent conducting oxide thin-film development for Indium-Tin-Oxide (ITO) substitutes," *Thin Solid Films,* vol. 516, no. 17, pp. 5822-5828, 2008.

[69] M. Frenzel, C. Mikolajczak, M. A. Reuter, and J. Gutzmer, "Quantifying the relative availability of high-tech by-product metals – The cases of gallium, germanium and indium," *Resources Policy,* vol. 52, pp. 327-335, 2017.

[70] V. M. Fthenakis, S. C. Morris, P. D. Moskowitz, and D. L. Morgan, "Toxicity of cadmium telluride, copper indium diselenide, and copper gallium diselenide," *Progress in Photovoltaics: Research and Applications,* vol. 7, no. 6, pp. 489-497, 1999.

[71] M. A. Green, "Estimates of te and in prices from direct mining of known ores," *Progress in Photovoltaics: Research and Applications,* vol. 17, no. 5, pp. 347-359, 2009.

[72] M. Bivour, H. Steinkemper, J. Jeurink, S. Schroeer, and M. Hermle, "Rear emitter silicon heterojunction solar cells: Fewer restrictions on the optoelectrical properties of front side TCOs," *Energy Procedia,* vol. 55, pp. 229-234, 2014.

[73] O. Madani Ghahfarokhi, K. Chakanga, S. Geissendoerfer, O. Sergeev, K. von Maydell, and C. Agert, "DC-sputtered ZnO:Al as transparent conductive oxide for silicon heterojunction solar cells with µc-Si:H emitter," *Progress in Photovoltaics: Research and Applications,* vol. 23, no. 10, pp. 1340-1352, 2015.

[74] L. Korte, E. Conrad, H. Angermann, R. Stangl, and M. Schmidt, "Advances in a-Si:H/c-Si heterojunction solar cell fabrication and characterization," *Solar Energy Materials and Solar Cells,* vol. 93, no. 6-7, pp. 905-910, 2009.

[75] W. Kern, "The evolution of silicon wafer cleaning technology," *Journal of Electrochemical Society*, vol. 137, no. 6, 1990.

[76] F. L. McCrackin, E. Passaglia, R. R. Stromberg, and H. L. Steinberg, "Measurement of the thickness and refractive index of very thin films and the optical properties of surfaces by ellipsometry," *Journal of Research of the National Bureau of Standards-A. Physics and Chemistry,* vol. 67A, no. 4, pp. 363-377, 1963.

[77] Brochure of M-2000 ellipsometer from J. A Woollam, https://www.jawoollam.com/download/pdfs/m-2000-brochure.pdf.

[78] D. A. Long, "Raman spectroscopy" in "The characterization of chemical purity: Organic compounds", pp. 149-161, edited by L. A. K. Staveley, London, Butterworths, 1971.

[79] F. Koehler, S. Schicho, B. Wolfrum, A. Gordijn, S. E. Pust, and R. Carius, "Gradient etching of silicon-based thin films for depth-resolved measurements: The example of Raman crystallinity," *Thin Solid Films,* vol. 520, no. 7, pp. 2605-2608, 2012.

118

[80]   W. B. Jackson, N. M. Amer, A. C. Boccara, and D. Fournier, "Photothermal deflection spectroscopy and detection," *Applied Optics*, vol. 20, no. 8, pp. 1333-1344, 1981.

[81]   WCT-120 Photoconductance Lifetime Tester and Suns-V_{oc} user manual from Sinton instruments, v3.0.

[82]   A. Sinton, A. Cuevas, and M. Stuckings, "Quasi-steady-state photoconductance, a new method for solar cell material and device characterization," in *IEEE 25th Photovoltaics Specialists Conference (PVSC)*, pp. 457-460, Washington, DC. USA, 1996.

[83]   H. H. Berger, "Models for contacts to planar device," *Solid-State Electronics*, vol. 15, no. 2, pp. 145-158, 1972.

[84]   O. Astakhov, R. Carius, F. Finger, Y. Petrusenko, V. Borysenko, and D. Barankov, "Relationship between defect density and charge carrier transport in amorphous and microcrystalline silicon," *Physical Review B*, vol. 79, no. 10, pp. 104205, 2009.

[85]   S. Olibet, C. Monachon, A. Hessler-Wyser, E. Vallat-Sauvain, S. De Wolf, L. Fesquet, J. Damon-Lacoste, and C. Ballif, "Textured silicon heterojunction solar cells with over 700 mV open-circuit voltage studied by transmission electron microscopy," in *23rd European Photovoltaic Solar Energy Conference (EU PVSEC)*, Valencia, Spain, 2008.

[86]   Z. A. Wang, J. B. Chu, H. B. Zhu, Z. Sun, Y. W. Chen, and S. M. Huang, "Growth of ZnO:Al films by RF sputtering at room temperature for solar cell applications," *Solid-State Electronics*, vol. 53, no. 11, pp. 1149-1153, 2009.

[87]   L. Ding, S. Nicolay, J. Steinhauser, U. Kroll, and C. Ballif, "Relaxing the conductivity/transparency trade-off in MOCVD ZnO thin films by hydrogen plasma," *Advanced Functional Materials*, vol. 23, no. 41, pp. 5177-5182, 2013.

[88]   B. Macco, Y. Wu, D. Vanhemel, and W. M. M. Kessels, "High mobility In_2O_3:H transparent conductive oxides prepared by atomic layer deposition and solid phase crystallization," *Physica Status Solidi (RRL) - Rapid Research Letters*, vol. 8, no. 12, pp. 987-990, 2014.

[89]   P. J. M. Isherwood, M. Gona, J. W. Bowers, N. Neves, P. Newbatt, and J. M. Walls, "Comparison of DC and RF sputtered aluminium-doped zinc oxide for photovoltaic applications", in *IEEE 42nd Photovoltaic Specialist Conference (PVSC)*, New Orleans, USA, 2015.

[90]   S. Rahmane, M. A. Djouadi, M. S. Aida, N. Barreau, B. Abdallah, and N. Hadj Zoubir, "Power and pressure effects upon magnetron sputtered aluminum doped ZnO films properties," *Thin Solid Films*, vol. 519, no. 1, pp. 5-10, 2010.

[91]   A. Matsuda, "Microcrystalline silicon.: Growth and device application," *Journal of Non-Crystalline Solids*, vol. 338-340, pp. 1-12, 2004.

[92]   O. Vetterl, F. Finger, R. Carius, P. Hapke, L. Houben, O. Kluth, A. Lambertz, A. Mueck, B. Rech, and H. Wagner, "Intrinsic microcrystalline silicon: A new material for photovoltaics," *Solar Energy Materials and Solar Cells*, vol. 62, pp. 97-108, 2000.

[93]   A. Lambertz, F. Finger, R. E. I. Schropp, U. Rau, and V. Smirnov, "Preparation and measurement of highly efficient a-Si:H single junction solar cells and the advantages of

μc-SiOₓ:H n-layers," *Progress in Photovoltaics: Research and Applications,* vol. 23, no. 8, pp. 939-948, 2015.

[94]   P. Koswatta, M. Boccard, and Z. Holman, "Carrier-selective contacts in silicon solar cells," in *IEEE 42nd Photovoltaic Specialist Conference (PVSC)*, New Orleans, LA, USA, 2015.

[95]   M. Bivour, M. Reusch, F. Feldmann, M. Hermle, and S. Glunz , "Requirements for carrier selective silicon heterojunctions," in *24th Workshop on Crystalline Silicon Solar Cells and Modules: Materials and Processes*, Breckenridge, Colorado, USA, 2014.

[96]   J. F. Chang and M. H. Hon, "The effect of deposition temperature on the properties of Al-doped zinc oxide thin films," *Thin Solid Films*, vol. 386, pp. 79-86, 2001.

[97]   R. A. Sinton and A. Cuevas, "Contactless determination of current-voltage characteristics and minority-carrier lifetimes in semiconductors from quasi-steady-state photoconductance data," *Applied Physics Letters,* vol. 69, no. 17, pp. 2510-2512, 1996.

[98]   D. Chen, L. Zhao, H. Diao, W. Zhang, G. Wang, and W. Wang, "Low-temperature sintering properties of the screen-printed silver paste for a-Si:H/c-Si heterojunction solar cells," *Journal of Materials Science: Materials in Electronics,* vol. 25, no. 6, pp. 2657-2664, 2014.

[99]   V. Smirnov, S. Reynolds, F. Finger, R. Carius, and C. Main, "Metastable effects in silicon thin films: Atmospheric adsorption and light-induced degradation," *Journal of Non-Crystalline Solids,* vol. 352, no. 9-20, pp. 1075-1078, 2006.

[100]   F. Finger, R. Carius, T. Dylla, S. Klein, S. Okur, and M. Guenes, "Stability of microcrystalline silicon for thin film solar cell applications," *IEE Proceedings - Circuits, Devices and Systems,* vol. 150, no. 4, pp. 300-308, 2003.

[101]   L. Xiao, O. Astakhov, F. Finger, and M. Stutzmann, "Determination of the defect density in thin film amorphous and microcrystalline silicon from ESR measurements: The influence of the sample preparation procedure," *Journal of Non-Crystalline Solids,* vol. 358, no. 17, pp. 2078-2081, 2012.

[102]   R. Rößler, C. Leendertz, L. Korte, N. Mingirulli, and B. Rech, "Impact of the transparent conductive oxide work function on injection-dependent a-Si:H/c-Si band bending and solar cell parameters," *Journal of Applied Physics,* vol. 113, no. 14, pp. 144513, 2013.

[103]   B. Demaurex, S. De Wolf, A. Descoeudres, Z. C. Holman, and C. Ballif, "Damage at hydrogenated amorphous/crystalline silicon interfaces by indium tin oxide overlayer sputtering," *Applied Physics Letters,* vol. 101, no. 17, pp. 171604, 2012.

[104]   A. Illiberi, P. Kudlacek, A. H. M. Smets, M. Creatore, and M. C. M. van de Sanden, "Effect of ion bombardment on the a-Si:H based surface passivation of c-Si surfaces," *Applied Physics Letters*, vol. 98, no. 24, pp. 242115, 2011.

[105]   F. Lebreton, S. N. Abolmasov, F. Silva, and P. Roca i Cabarrocas, "In situ photoluminescence study of plasma-induced damage at the a-Si:H/c-Si interface," *Applied Physics Letters,* vol. 108, no. 5, pp. 051603, 2016.

[106]   A. Morales-Vilches, C. Voz, M. Colina, G. López, I. Martín, P. Ortega, A. Orpella, and R. Alcubilla, "Recovery of indium-tin-oxide/silicon heterojunction solar cells by thermal annealing," *Energy Procedia,* vol. 44, pp. 3-9, 2014.

[107] S. De Wolf, S. Olibet, and C. Ballif, "Stretched-exponential a-Si:H/c-Si interface recombination decay," *Applied Physics Letters,* vol. 93, no. 3, pp. 032101, 2008.

[108] H. Li, W. Duan, A. Lambertz, J. Huepkes, K. Ding, F. Finger, U. Rau, and O. Astakhov, "Application of room temperature sputtered Al-doped zinc oxide in silicon heterojunction solar cells," in *IEEE 7th World Conference on Photovoltaic Energy Conversion* (*WCPEC*), Waikoloa Village, HI, USA, pp. 2151-2154, 2018.

[109] S. Bowden and A. Rohatgi, "Rapid and accurate determination of series resistance and fill factor losses in industrial silicon solar cells," in *17th European Photovoltaic Solar Energy Conference and Exhibition*, Munich, Germany, 2001.

[110] D. Pysch, A. Mette, and S. W. Glunz, "A review and comparison of different methods to determine the series resistance of solar cells," *Solar Energy Materials and Solar Cells,* vol. 91, no. 18, pp. 1698-1706, 2007.

[111] M. Boccard, R. Monnard, L. Antognini, and C. Ballif, "Silicon oxide treatment to promote crystallinity of p-type microcrystalline layers for silicon heterojunction solar cells," *AIP Conference Proceedings 1999*, pp. 040003, 2018.

[112] J. Mueller, O. Kluth, S. Wieder, H. Siekmann, G. Schoepe, W. Reetz, O. Vetterl, D. Lundszien, A. Lambertz, F. Finger, B. Rech, and H. Wagner, "Development of highly efficient thin flm silicon solar cells on texture-etched zinc oxide-coated glass substrates," *Solar Energy Materials and Solar Cells,* vol. 66, pp. 275-281, 2001.

[113] B. Rech, O. Kluth, T. Repmann, T. Roschek, J. Springer, J. Mueller, F. Finger, H. Stiebig, and H. Wagner, "New materials and deposition techniques for highly efficient silicon thin film solar cells," *Solar Energy Materials and Solar Cells,* vol. 74, pp. 439-447, 2002.

[114] W. Shockley and H. J. Queisser, "Detailed balance limit of efficiency of p-n junction solar cells," *Journal of Applied Physics,* vol. 32, no. 3, pp. 510-519, 1961.

[115] T. Tiedje, E. Yablonovitch, G. D. Cody, and B.G. Brooks, "Limiting efficiency of silicon solar cells," *IEEE Transactions on Electron Devices*, vol. ED-31, no. 5, pp. 711-716, 1984.

[116] M. A. Green, "Limits on the open-circuit voltage and efficiency of silicon solar cells imposed by intrinsic Auger processes" *IEEE Transactions on Electron Devices*, vol. ED-31, no. 5, pp. 671-678, 1984.

[117] M. J. Kerr, A. Cuevas, and P. Campbell, "Limiting efficiency of crystalline silicon solar cells due to Coulomb-enhanced Auger recombination," *Progress in Photovoltaics: Research and Applications,* vol. 11, no. 2, pp. 97-104, 2003.

[118] A. Hangleiter and R. Haecker, "Enhancement of band-to-band Auger recombination by electron-hole correlations," *Physical Review Letters,* vol. 65, no. 2, pp. 215-218, 1990.

[119] T. Trupke, M. A. Green, P. Wuerfel, P. P. Altermatt, A. Wang, J. Zhao, and R. Corkish, "Temperature dependence of the radiative recombination coefficient of intrinsic crystalline silicon," *Journal of Applied Physics,* vol. 94, no. 8, pp. 4930-4937, 2003.

[120] P. P. Altermatt, F. Geelhaar, T. Trupke, X. Dai, A. Neisser, and E. Daub, "Injection dependence of spontaneous radiative recombination in crystalline silicon: Experimental verification and theoretical analysis," *Applied Physics Letters,* vol. 88, no. 26, pp. 261901, 2006.

References

[121] A. Richter, S. W. Glunz, F. Werner, J. Schmidt, and A. Cuevas, "Improved quantitative description of Auger recombination in crystalline silicon," *Physical Review B,* vol. 86, no. 16, pp. 165202, 2012.

[122] M. A. Green, "Lambertian light trapping in textured solar cells and light-emitting diodes: analytical solutions," *Progress in Photovoltaics: Research and Applications,* vol. 10, no. 4, pp. 235-241, 2002.

[123] F. Haase, S. Schaefer, C. Klamt, F. Kiefer, J. Kruegener, R. Brendel, and R. Peibst, "Perimeter recombination in 25%-efficient IBC solar cells with passivating POLO contacts for both polarities," *IEEE Journal of Photovoltaics,* vol. 8, no. 1, pp. 23-29, 2018.

[124] A. Khanna, T. Mueller, R. A. Stangl, B. Hoex, P. K. Basu, and A. G. Aberle, "A fill factor loss analysis method for silicon wafer solar cells," *IEEE Journal of Photovoltaics,* vol. 3, no. 4, pp. 1170-1177, 2013.

[125] M. Leilaeioun and Z. Holman, "A new expression for intrinsic fill factor of silicon solar cells," in *IEEE 42nd Photovoltaic Specialist Conference (PVSC)*, New Orleans, LA, USA, 2015.

[126] W. Shockley and W. T. Read, Jr. "Statistics of the recombinations of holes and electrons," *Physical Review,* vol. 87, no. 5, pp. 835-842, 1952.

[127] K. R. McIntosh, "Lumps, Humps and Bumps: Three detrimental effects in the current-voltage curve of silicon solar cells", *PhD thesis*, 2001.

[128] O. Breitenstein, J. P. Rakotoniaina, M. H. Al Rifai, and M. Werner, "Shunt types in crystalline silicon solar cells," *Progress in Photovoltaics: Research and Applications,* vol. 12, no. 7, pp. 529-538, 2004.

[129] K. Qiu, Q. Xie, D. Qiu, L. Cai, W. Wu, W. Lin, Z. Yao, B. Ai, Z. Liang, and H. Shen, "Power-loss analysis of a dopant-free ZnS/p-Si heterojunction solar cell with WO_3 as hole-selective contact," *Solar Energy,* vol. 165, pp. 35-42, 2018.

[130] K. R. McIntosh and S. C. Baker-Finch, "OPAL 2: Rapid optical simulation of silicon solar cells," in *38th IEEE Photovoltaic Specialists Conference*, Austin, TX, USA, 2012.

Abbreviations and symbols

A	absorptance
α	absorption coefficient
η	energy conversion efficiency
d_{AZO}	AZO layer thickness
σ	electrical conductivity
σ_{dark}	dark conductivity
E	energy
EQE	external quantum efficiency
f	frequency
f_{metal}	metal fraction
ϕ	gas flow rate
Φ_{abs}	absorbed photon flux
Φ_{inc}	incident photon flux
ϕ_{H2}	H_2 flow rate
ϕ_{B2H6}	B_2H_6 flow rate
ϕ_{PH3}	PH_3 flow rate
ϕ_{SiH4}	SiH_4 flow rate
ϕ_{TMB}	TMB flow rate
FF	fill factor
FF_0	fill factor without considering R_s and R_{sh}
FF_{J01}	fill factor without considering R_s, R_{sh} and J_{02}
ΔFF_{J02}	fill factor loss from J_{02} related recombination

Abbreviations and symbols

$\mathbf{\mathit{\Delta FF_{Rs}}}$	fill factor loss from R_s
$\mathbf{\mathit{\Delta FF_{Rsh}}}$	fill factor loss from R_{sh}
$\mathbf{\mathit{\Delta n}}$	excess carrier density
$\mathbf{\Delta V}$	voltage offset
$\mathbf{\Delta V_d}$	voltage offset between dark I-V and I_{sc}-V_{oc}
$\mathbf{\Delta V_l}$	voltage offset between light I-V and I_{sc}-V_{oc}
$\mathbf{\mathit{I}}$	current
$\mathbf{\mathit{I_c}}$	crystalline volume fraction
$\mathbf{\mathit{I_{dark}}}$	dark current
$\mathbf{iFF}$	implied fill factor
$\mathbf{\mathit{I_{mpp}}}$	current at maximum power point
$\mathbf{\mathit{I_{ph}}}$	photo current
$\mathbf{IQE}$	internal quantum efficiency
$\mathbf{\mathit{I_{sc}}}$	short circuit current
$\mathbf{iV_{oc}}$	implied open circuit voltage
$\mathbf{\mathit{J}}$	current density
$\mathbf{\mathit{J_0}}$	saturation current density
$\mathbf{\mathit{J_{01}}}$	saturation current density for the first diode in the two-diode model
$\mathbf{\mathit{J_{02}}}$	saturation current density for the second diode in the two-diode model
$\mathbf{\mathit{J_{loss,J01}}}$	current loss related to J_{01}
$\mathbf{\mathit{J_{loss,J02}}}$	current loss related to J_{02}
$\mathbf{\mathit{J_{mpp}}}$	current density at maximum power point
$\mathbf{\mathit{J_{sc}}}$	short circuit current density
$\mathbf{\mathit{J_{AM1.5G}}}$	J generated from the AM1.5G spectrum
$\mathbf{\mathit{J_{sc,\,EQE}}}$	J generated from the EQE response

124

$J_{EQE,\ active\ area}$	J generated from the active area EQE response
$J_{1-front\ refl.}$	J generated without the front reflection simulated by "OPAL2"
$J_{front\ refl.}$	J loss from the front reflection simulated by "OPAL2"
J_{short}	J loss in the short wavelength region
J_{medium}	J loss in the medium wavelength region
J_{long}	J loss in the long wavelength region
$J_{shadowing}$	J loss from the front shadowing
$J_{front\ escape}$	J loss due to the light escape from the front side of the solar cell
$J_{rear\ escape}$	J loss due to the light escape from the rear side of the cell without mentalization
$J_{total\ loss}$	Total loss of J
λ	wavelength
L	spacing
L_T	transfer length
μ	mobility
n_1	ideality factor for the first diode in the two-diode model
n_2	ideality factor for the second diode in the two-diode model
n	carrier concentration
n_{if}	diode ideality factor
P	deposition power
P_{in}	input power
P_{max}	power at maximum power point
pFF	pseudo fill factor
QE	quantum efficiency
R	reflectance

Abbreviations and symbols

R_c	contact resistance
R_{cell}	reflectance of the non-metallization area of the solar cell
r_d	deposition rate
r_{B2H6}	the ratio between the gas flow rates of B_2H_6 and SiH_4
r_{PH3}	the ratio between the gas flow rates of PH_3 and SiH_4
r_{SiH4}	the ratio between the gas flow rates of SiH_4 and H_2
r_{TMB}	the ratio between the gas flow rates of TMB and SiH_4
$R_{front\ refl.}$	front surface reflection of solar cell simulated by "OPAL2" or R_{OPAL}
R_s	series resistance
R_s^{AZO}	AZO resistance
$R_s^{front\ finger}$	front finger resistance
$R_s^{front\ (i/n)}$	front i/n stack resistance
R_s^{wafer}	wafer resistance
$R_s^{rear\ (i/p)}$	rear i/p stack resistance
$R_s^{rear\ Ag}$	rear Ag resistance
$R_s^{AZO/Ag}$	contact resistance at the interface between AZO and Ag
$R_s^{AZO/front\ (i/n)}$	contact resistance at the interface between AZO and front i/n stack
$R_s^{front\ (i/n)/\ wafer}$	contact resistance at the interface between front i/n stack and AZO
$R_s^{AZO/(i/n)/wafer}$	total resistance of $R_s^{AZO/front\ (i/n)}$ and $R_s^{front\ (i/n)/\ wafer}$
$R_s^{wafer/rear\ (i/p)}$	contact resistance at the interface between wafer and rear i/p stack
$R_s^{rear\ (i/p)/\ AZO}$	contact resistance at the interface between rear i/p stack and AZO
$R_s^{wafer/(i/p)/AZO}$	total resistance of $R_s^{wafer/rear\ (i/p)}$ and $R_s^{rear\ (i/p)/\ AZO}$
R_{sh}	shunt resistance
R_{sheet}	sheet resistance
R_t	total resistance

ρ	resistivity
ρ_c	specific contact resistance
S	surface recombination velocity
T	transmittance
T_{cell}	transmittance of the non-metallization area of the solar cell
T_{sub}	substrate temperature
$T_{temp.}$	temperature
τ	lifetime
τ_{Auger}	Auger lifetime
τ_{bulk}	bulk lifetime
τ_{eff}	effective carrier lifetime
τ_{rad}	radiative lifetime
τ_{SRH}	Shockley-Read-Hall lifetime
V	voltage
V_{mpp}	voltage at maximum power point
V_{oc}	open circuit voltage
W	wafer thickness
x	stoichiometry number
Ag	silver
a-IZO	amorphous indium zinc oxide
Al	aluminum
a-	amorphous
a-Si	amorphous silicon
a-SiC	amorphous silicon carbide

Abbreviations and symbols

Al₂O₃	aluminum oxide
Al BSF	Al-back surface field
ALD	atomic layer deposition
AM	air mass
AZO	Al-doped zinc oxide
B(CH₃)₃	trimethyl borane or TMB
B₂H₆	diborane
BSF	back surface field
c	speed of the light
c-Si	crystalline silicon
CCl₄	carbon tetrachloride
Cu	copper
CVD	chemical vapor deposition
Cz	Czochralski
DC	direct current
eV	electron volt
FCA	free carrier absorption
FSF	front surface field
h	Plank's constant
:H	hydrogenated
H	hydrogen
H₂	molecular hydrogen
H₂O₂	hydrogen peroxide
HCl	hydrogen Chloride
HF	hydrogen fluoride

HIT	heterojunction with intrinsic thin layer
HJ	heterojunction
HJT	heterojunction technology
HJ-IBC	heterojunction interdigitated back contact
i-	intrinsic
I-V	current-voltage
I_{sc}-V_{oc}	short circuit current-open circuit voltage
i/n	intrinsic a-Si/n-type nc-Si
i/p	intrinsic a-Si/p-type a-Si
IBC	interdigitated back contact
In_2O_3	indium oxide
IO:H	hydrogen-doped indium oxide
ITO	indium tin oxide
J-V	current density-voltage
J_{sc}-V_{oc}	short circuit current density-open circuit voltage
k	Boltzmann constant
LCOE	levelized cost of energy
LM	loading module
μc-	microcrystalline
μc-Si:H	hydrogenated microcrystalline silicon
M2	156.75 mm × 156.75 mm
Mo	molybdenum
MPP	maximum power point
n-	n-type doped
nc-	nanocrystalline

nc-Si	nanocrystalline silicon
nc-Si:H	hydrogenated nanocrystalline silicon
nc-SiO$_x$	nanocrystalline silicon oxide
NH$_4$OH	ammonia solution
Ω	ohm
O$_2$	oxygen
p-	p-type doped
PC	process chamber
PDS	photothermal deflection spectroscopy
PECVD	plasma enhanced chemical vapor deposition
PERC	passivated emitter and rear cell
PERD	passivated emitter and rear directly-contacted
PERF	passivated emitter, rear floating-junction
PERL	passivated emitter, rear locally diffused
PERT	passivated emitter, rear totally-diffused
PH$_3$	phosphine
PM	process module
PV	photovoltaics
q	electron charge
QSSPC	quasi steady-state photo conductance
RCA	standard cleaning process developed at Radio Corporation of America
RF	radio frequency
RT	room temperature
SC	standard cleaning
sccm	standard cubic centimeter

SHJ	silicon heterojunction
Si	silicon
SiH$_4$	silane
SRH	Shockley-Read-Hall
TCO	transparent conductive oxide
Ti	titanium
TLM	transfer length method
TMB	trimethyl borane
TOPCon	tunnel oxide passivated contact
UV-Vis-NIR	ultraviolet – visible – near-infrared
W	tungsten
wt.%	weight percentage
ZnO	zinc oxide
Zr	zirconium

Curriculum Vitae

Personal details

Name:	Huimin Li
Date of birth:	January 27th, 1989
Place of birth:	Hebei, China
Nationality:	Chinese

Education

1995 – 2001	Primary school in Hebei, China.
2001 – 2004	Nanyang middle school in Hebei, China.
2004 – 2008	Rongcheng high school in Hebei, China.
2008 – 2012	Bachelor of Science in Optical Information Science and Technology at Hebei University. Bachelor thesis at Institute of Physics Science and Technology.
2012 – 2015	Master of Science in Engineering in Optical Engineering at Hebei University. Master thesis at Institute of Physics Science and Technology. Title: Photoelectric Properties Analysis of nc-SiO$_x$:H Thin Films Prepared by VHF-PECVD.
2015 – now	PhD student in the field of silicon heterojunction solar cells at Institute of Energy and Climate Research IEK-5 Photovoltaics in Forschungszentrum Jülich.

List of Publications

H. Li, O. Astakhov, D. Weigand, J. Hüpkes, A. Lambertz, K. Ding, "Single-chamber silicon deposition process for industrial silicon heterojunction solar cells," *poster* 2AV.3.11*, in 32nd European Photovoltaic Solar Energy Conference and Exhibition (EU PVSEC)*, Munich, Germany, 2016.

H. Li, W. Duan, A. Lambertz, J. Hüpkes, K. Ding, F. Finger, U. Rau, and O. Astakhov, "Application of room temperature sputtered Al-doped zinc oxide in silicon heterojunction solar cells," in *IEEE 7th World Conference on Photovoltaic Energy Conversion (WCPEC)(A Joint Conference of 45th IEEE PVSC, 28th PVSEC & 34th EU PVSEC),* pp. 2151-2154, Waikoloa Village, HI, USA, 2018.

H. Li, W. Duan, A. Lambertz, J. Hüpkes, K. Ding, U. Rau, and O. Astakhov, "Influence of room Temperature sputtered Al-doped zinc oxide on passivation quality in silicon heterojunction solar cells," *IEEE Journal of Photovoltaics*, vol. 9, pp. 1485-1491, 2019.

H. Li, W. Duan, A. Lambertz, K. Ding, U. Rau, and O. Astakhov, "Investigation on the contact between doped nanocrystalline silicon and Al-doped zinc oxide in silicon heterojunction solar cells," (submitted).

Acknowledgements

I would like to thank all the people who help to make this PhD work possible. I would like to specify my great thanks to the following people for their contributions during my PhD time:

- Prof. Dr. Uwe Rau for being my doctor father and providing me the opportunity to work as a PhD student at IEK-5 photovoltaic, for his supervision and instruction on the PhD work, and for his support and encouragement on me.

- Prof. Dr. Joachim Knoch for being a reviewer of my PhD thesis and a member of the defense committee, for his suggestions on this work and kind support during my PhD time.

- Dr. Oleksandr Astakhov for being a great supervisor who supports me at any time, for being together to get into the SHJ solar cell field, for reading my presentations, reports, manuscripts and PhD thesis and giving feedback quickly, and for the proper attitude towards science and conducting research, and for his encouragement and the optimistic attitude towards life.

- Dr. Kaining Ding for being the contact person during my PhD application, for being an excellent group leader who provides me excellent research platform and keeps me on the right track, for his support with solving problems and continuous encouragement.

- Dr. Tsvetelina Merdzhanova for her kind support with the project development, for the help with paper work, for the support on defense presentation preparation, and for her continuous encouragement on me.

- Dr. Weiyuan Duan for many fruitful and meaningful discussion on the SHJ solar cell development, for giving excellent suggestions on the manuscript preparation, for the help to widen my overview on SHJ solar cell development in laboratory and in industry, and for the continuous encouragement on me.

- Dr. Andreas Lambertz for his supporting on the SHJ solar cell preparation and characterization, for his support from baseline development, for his kind instructions on research direction and detailed comments on experimental results, and for his professionalism to work.

Band / Volume 502
Auswirkungen der Energiewende auf das deutsche Gastransportsystem
B. Gillessen (2020), XVII, 186
ISBN: 978-3-95806-487-4

Band / Volume 503
Lagrangian Simulation of Stratospheric Water Vapour: Impact of Large-Scale Circulation and Small-Scale Transport Processes
L. Poshyvailo (2020), 124 pp
ISBN: 978-3-95806-488-1

Band / Volume 504
Water Management in Automotive Polymer-Electrolyte-Membrane Fuel Cell Stacks
S. Asanin (2020), XVIII, 172 pp
ISBN: 978-3-95806-491-1

Band / Volume 505
Towards a new real-time irrigation scheduling method: observation, modelling and their integration by data assimilation
D. Li (2020), viii, 94 pp
ISBN: 978-3-95806-492-8

Band / Volume 506
Modellgestützte Analyse kosteneffizienter CO_2-Reduktionsstrategien
P. M. Lopion (2020), XIV, 269 pp
ISBN: 978-3-95806-493-5

Band / Volume 507
Integration of Renewable Energy Sources into the Future European Power System Using a Verified Dispatch Model with High Spatiotemporal Resolution
C. Syranidou (2020), VIII, 242 pp
ISBN: 978-3-95806-494-2

Band / Volume 508
Solar driven water electrolysis based on silicon solar cells and earth-abundant catalysts
K. Welter (2020), iv, 165 pp
ISBN: 978-3-95806-495-9

Band / Volume 509
Electric Field Assisted Sintering of Gadolinium-doped Ceria
T. P. Mishra (2020), x, 195 pp
ISBN: 978-3-95806-496-6

Schriften des Forschungszentrums Jülich
Reihe Energie & Umwelt / Energy & Environment

Band / Volume 510
Effect of electric field on the sintering of ceria
C. Cao (2020), xix, 143 pp
ISBN: 978-3-95806-497-3

Band / Volume 511
Techno-ökonomische Bewertung von Verfahren zur Herstellung von Kraftstoffen aus H$_2$ und CO$_2$
S. Schemme (2020), 360 pp
ISBN: 978-3-95806-499-7

Band / Volume 512
Enhanced crosshole GPR full-waveform inversion to improve aquifer characterization
Z. Zhou (2020), VIII, 136 pp
ISBN: 978-3-95806-500-0

Band / Volume 513
Time-Resolved Photoluminescence on Perovskite Absorber Materials for Photovoltaic Applications
F. Staub (2020), viii, 198 pp
ISBN: 978-3-95806-503-1

Band / Volume 514
Crystallisation of Oxidic Gasifier Slags
J. P. Schupsky (2020), III, 127, XXII pp
ISBN: 978-3-95806-506-2

Band / Volume 515
Modeling and validation of chemical vapor deposition for tungsten fiber reinforced tungsten
L. Raumann (2020), X, 98, XXXVIII pp
ISBN: 978-3-95806-507-9

Band / Volume 516
Zinc Oxide / Nanocrystalline Silicon Contacts for Silicon Heterojunction Solar Cells
H. Li (2020), VIII, 135 pp
ISBN: 978-3-95806-508-6

Weitere *Schriften des Verlags im Forschungszentrum Jülich* unter
http://wwwzb1.fz-juelich.de/verlagextern1/index.asp

JÜLICH
Forschungszentrum